IRREVERSIBLE TRANSPORT PHENOMENA IN POLYCRYSTALLINE $Bi_{1.7}Pb_{0.3}Sr_2Ca_2Cu_3O_x$ SUPERCONDUCTORS

by

HAKAN YETİŞ

THESIS SUBMITTED TO
THE GRADUATE SCHOOL OF NATURAL AND APPLIED SCIENCES
OF
THE ABANT İZZET BAYSAL UNIVERSITY
IN PARTIAL FULFILLMENT OF THE REQUIREMENTS FOR THE DEGREE OF
DOCTOR OF PHILOSOPHY
IN
THE DEPARTMENT OF PHYSICS

JUNE 2009

Approval of the Graduate School of Natural and Applied Sciences

Prof. Dr. Nihat ÇELEBİ

Director

I certify that this thesis satisfies all the requirements as a thesis for the degree of Doctor of Philosophy.

Prof. Dr. Kıvılcım KILIÇ

Head of Physics Department

This is to certify that we have read this thesis and that in our opinion it is fully adequate, in scope and quality, as a thesis for the degree of Doctor of Philosophy.

Prof. Dr. Atilla KILIÇ

Supervisor

Examining Commitee Members

1. Prof. Dr. Mehmet CANKURTARAN ....
2. Prof. Dr. Atilla KILIÇ ....
3. Prof. Dr. Kıvılcım KILIÇ ....
4. Assoc. Prof. Dr. Oktay ÇETİN ....
5. Assist. Prof. Dr. Aliekber AKTAĞ ....

ABSTRACT

IRREVERSIBLE TRANSPORT PHENOMENA IN POLYCRYSTALLINE $Bi_{1.7}Pb_{0.3}Sr_2Ca_2Cu_3O_x$ SUPERCONDUCTORS

Yetiş, Hakan

Ph.D., Department of Phyics

Supervisor: Prof. Dr. Atilla KILIÇ

June 2009, 151 pages

The aim of this study is to investigate the magnetic flux dynamics in a polycrystalline sample of superconducting $Bi_{1.7}Pb_{0.3}Sr_2Ca_2Cu_3O_x$ (BSCCO) with a macroscopic cylindrical hole (CH) drilled through the sample. Current-voltage (I – V curves), transport relaxation (V – t curves), and magnetovoltage (V – H curves) measurements were carried out as functions of transport current (I), temperature (T), and external magnetic field (H) on the BSCCO sample before drilling the CH. Then, similar measurements were carried out on the same BSCCO sample after drilling the CH. The results can be summarized as follows:

(i) The hysteresis effects in the I – V curves of the sample without CH disappear for all dI/dt values at $H \neq 0$, and the I – V curves exhibit approximately linear behavior. However, the hysteresis effects in the I – V curves of sample with CH are still observed for the same magnetic field, temperature and dI/dt values. The results suggest that the CH behaves as a macroscopic flux pinning center for

the flux lines, which reduces the measured voltage dissipation by preventing the flux motion.

(ii) In order to investigate the penetration of the driving current into the samples, a maximum current (I_{max}) was applied to the samples and decreased to zero with a certain value of dI/dt. Then, the current was increased from zero to I_{max} with the same value of dI/dt. The voltage humps which indicate the existence of an obstruction due to the surface effects and also by the presence of CH were observed at low values of I_{max}.

(iii) The $V - t$ measurements of the sample with CH showed some discontinuities which were attributed to the leaving of flux lines via the CH and surface effects. In addition, we observed a new type of non-linear dynamic response to bidirectional square wave (BSW) current applied to the sample reflects itself as regular sinusoidal-like voltage oscillations.

(iv) The $V - H$ curves measured for the sample with CH depend on the field ramping rate (dH/dt) and exhibit prominent counter clockwise hysteresis effects which are unusual when compared to those for the sample without CH.

Keywords: Type-II Superconductors, $I - V$ Curves, Magnetovoltage, Transport Relaxation Curves, Time Effects, Surface Effects, Vortex Dynamics.

ÖZET

POLİKRİSTAL $Bi_{1,7}Pb_{0,3}Sr_2Ca_2Cu_3O_x$ ÜSTÜNİLETKENLERDE TERSİNMEZ TAŞIMA OLAYLARI

Yetiş, Hakan

Doktora, Fizik Bölümü

Tez Danışmanı: Prof. Dr. Atilla KILIÇ

Haziran 2009, 151 sayfa

Bu çalışmanın amacı makroskopik silindirik bir delik (SD) açılmış polikristal $Bi_{1,7}Pb_{0,3}Sr_2Ca_2Cu_3O_x$ (BSCCO) üstüniletken örnek içinde oluşan manyetik akı hareketlerini araştırmaktır. Akım-gerilim (I – V eğrileri), taşıma durulma (V – t eğrileri), ve manyetovoltaj (V – H eğrileri) ölçümleri taşıma akımının (I), sıcaklığın (T) ve dış manyetik alanın (H) fonksiyonu olarak BSCCO örnek üzerinde, delik delinmeden önce, yapıldı. Sonra, silindirik deliğin örneğin taşıma özellikleri üzerindeki etkilerini araştırmak için, aynı BSCCO örnek üzerinde SD açıldıktan sonra benzer ölçümler tekrar yapıldı. Sonuçlar aşağıdaki gibi özetlenebilir:

(i) Deliksiz örneğe, bir dış manyetik alan uygulandığında, I – V eğrilerindeki histeresis etkileri tüm dI/dt değerleri için yok olur ve yaklaşık olarak doğrusal bir davranış sergiler. Buna karşın, aynı manyetik alan, sıcaklık ve dI/dt değerlerinde, delikli örneğin I – V eğrilerinde histeresis etkileri hala gözlenmektedir. Bu deneysel bulgular, silindirik deliğin akı çizgileri için bir

makroskopik akı tutma merkezi gibi davrandığını ve akı hareketini engelleyerek ölçülen voltaj harcanımını düşürdüğünü göstermektedir.

(ii) Sürücü akımın üstüniletken örneğin dış yüzeyinden içeriye doğru girişini araştırmak için, örneğe bir maksimum akım I_{max} uygulandı ve bu akım belirli bir akım tarama dI/dt hızıyla sıfıra düşürüldü. Sonra akım sıfırdan I_{max} değerine aynı dI/dt hızıyla artırıldı. Düşük I_{max} değerlerinde oluşan voltaj tepeleri, taşıma akımının örnek içine girişinin yüzey etkileri ve silindirik delik tarafından engellendiğini göstermektedir.

(iii) Delikli örneğin $V – t$ ölçümlerinde, akı çizgilerinin silindirik deliği terk etmesine ve yüzey etkilerine atfedilen bazı kesikliklerin meydana geldiği gözlendi. Ayrıca, $V – t$ eğrileri yardımıyla doğrusal olmayan yeni bir dinamik tepki gözledik. İki-yönlü kare dalga şeklinde bir sürücü akımın örneğe uygulanmasıyla oluşan bu doğrusal olmayan tepkiler, sıcaklığın, manyetik alanın, sürücü akımın genlik ve periyodunun belirli aralıkları içinde, düzenli sinüssel voltaj salınımları olarak ölçüldü.

(iv) Delikli örnekte ölçülen $V – H$ eğrilerinin alan tarama hızına (dH/dt) bağlı olduğunu ve (deliksiz örnekle karşılaştırıldığında) alışılmışın dışında, saat yönünün tersinde dönen belirgin histeresis etkileri gösterdiği gözlendi.

Anahtar Kelimeler: Tip-II Üstüniletkenler, $I – V$ Eğrileri, Manyetovoltaj, Taşıma Durulma Eğrileri, Zaman Etkileri, Yüzey Etkileri, Akı Dinamiği.

ACKNOWLEDGEMENTS

I should convey my heartfelt gratitude to everyone who helped me in the preparation and completion of this thesis.

I owe a great deal to my supervisor, Prof. Dr. Atilla Kılıç, for moral support, guidance and supervision throughout this study. His assistance brought my thesis to completion.

I am grateful to Prof. Dr. Kıvılcım Kılıç along with my advisor for her suggestions and contributions to the thesis.

I would like to thank Prof. Dr. Mehmet Cankurtaran at Hacettepe University for valuable discussions and critical reading of the thesis. I am obliged for his help in the revision of this dissertation.

I would like to direct special thanks to Assoc. Prof. Dr. Hüseyin Sözeri for the BSCCO samples prepared at TÜBİTAK (Gebze).

I would like to thank Assoc. Prof. Dr. Oktay Çetin for his friendship and contribution. I am thankful to research assistants Atılgan Altınkök and Murat Olutaş for their invaluable supports.

I am grateful to my wife Müge Yetiş who has always been with me.

Finally, I am grateful to my family for their support and encouragement all thorough my years in the university.

PREFACE

This thesis is based on my research within the Superconductivity group at the Abant İzzet Baysal University, Bolu, during the period of 2003 – 2009. It consists of seven chapters and an appendix. In chapter one, we give a broad overview of the earlier studies about the vortex dynamics in superconductors. Chapter two presents a brief introduction to vortices and superconductivity. In chapter three, the theoretical models which evaluate the time effects in transport measurements are introduced. In chapter four, the details of sample preparation and experimental set-up are given. In chapter five, the experimental results for current-voltage ($I - V$ curves), transport measurements ($V - t$ curves), slow voltage oscillations and magnetovoltage measurements ($V - H$ curves) are presented. In chapter six, the experimental results are discussed and compared with the theoretical models outlined in chapter three. In chapter seven, the results and findings are summarized.

TABLE OF CONTENTS

LIST OF FIGURES

FIGURES

CHAPTER 1

INTRODUCTION

The effect of transport current on vortex dynamics in type-II superconductors has been widely investigated experimentally [1–8] and theoretically [9, 10] and by realistic computer simulations [11–27]. Several dynamic phase transitions have been reported in those studies. It was found that the structure of flux line lattice (FLL) is highly dependent on both the magnitude of transport current and the strength of pinning defects. For instance, at low applied currents, it was observed that the vortices are almost pinned; as the current is increased, non-uniformly moving disordered vortex lattice is established along the sample depending on the magnitude of the Lorentz force. However, at high enough currents, the driving current enables vortices to form an ordered moving lattice by reducing the pinning barriers [6]. The competition between the pinning and depinning processes is generally considered as the source of many complex dynamics instabilities in type-II superconductors. The most pronounced example of this competition is the sudden enhancement of the critical current just below the upper critical field H_{c2}. This unusual phenomenon is known as the peak effect, and it has been attributed to the softening of the elastic moduli of the vortex lattice and strong pinning [2].

In addition to the peak effect, the vortex system displays many significant phenomena such as voltage noise [28], history dependent response [29], memory effects [6, 30], and metastability [31]. A comprehensive model which defines such instabilities was presented by Paltiel *et al.* [7] in their experimental study on a single-crystalline sample of 2H-$NbSe_2$. The authors showed that the applied current flowing along the edges of the sample causes a contamination by injecting a disordered vortex phase, while the current flowing in the bulk acts as an annealing mechanism. In Ref. [7] it is assumed that the ordered and metastable disordered vortex phases are present simultaneously in bulk of the sample and the driving current serves as an effective temperature in the usual sense as in the statistical mechanics so that it anneals the metastable disordered vortex phase towards the more ordered stable phase by depinning vortices from the pinning sites. This model could also be applied to the investigation of vortex dynamics in high-T_c superconductors [32].

These dynamical complexities of vortices in type-II superconductors were also explained in the frame of order-disorder transition of the vortex system or competing interactions between pinning and depinning of vortices [3–8, 33, 34]. The interplay between these two mechanisms determines the properties of the vortex system and is also highly dependent on the magnitude of the applied current or driving force. Due to the high pinning strength, the motion of flux lines at low currents forms defective flow patterns by causing plastic motion related to the ensemble of neighboring flux lines which move at different velocities; whereas, at high current levels, the flux line motion becomes correlated with nearly constant velocity along the whole sample. Fast and slow transport relaxation measurements and $I-V$ measurements with different current ramping rates performed on single-crystalline sample of 2H-$NbSe_2$ reveal clearly the degree of order of the vortex system and such reorganization of the vortices [6]. The transport relaxation measurements [3–8] showed that the moving vortices reorganize themselves into less ordered or more ordered states depending on the experimental conditions.

Voltage jumps, hysteresis and significant time effects were observed in the I – V curves of polycrystalline, superconducting $Y_1Ba_2Cu_2O_{7-\delta}$ (YBCO) samples [35] as a function of the current sweep rate (dI/dt) for both low and moderate dissipation levels on long time scales. It was found that the evolution of the I – V curves depends strongly on the cycling direction of the applied current and on the value of dI/dt, which leads to formation of significant hysteresis loops in the I – V curves. The width of the hysteresis loops decreases somewhat with reducing dI/dt which can be considered as an evidence of the time effect. The dynamical hysteresis effects were also observed in the I – V curves of single-crystalline type-II superconductors [36]. The instabilities and hysteresis effects in the I – V curves were discussed in terms of Joule heating at the current contacts depending on the magnitude of applied current [35, 37], inelastic quasi-particle scattering depending on the magnetic field strength [38], inhomogeneity in the flux pinning strength for polycrystalline superconductors [35, 39, 40] and dynamical metastability of vortex lattice [6, 29, 41–43].

Previous transport measurements, on the other hand, revealed that the dynamics of vortices in type-II superconductors depends on the type of transport current modulation. Gordeev *et al.* [3, 4] showed that the asymmetrical square wave (ASW) currents cause slow voltage oscillations on long time scale in de-twinned single-crystalline sample of $Y_1Ba_2Cu_3O_{7-\delta}$; whereas, they observed that bi-directional square wave (BSW) current enhances the magnitude of voltage response a few orders of magnitude when compared to direct current which did not cause any oscillation. This unusual behavior was attributed to the reorganization of vortex lattice by the transport current and the interplay between bulk and surface pinning. Kwok *et al.* [28] ascribed the time oscillations in the voltage response to an ac sinusoidal type current just below the melting line (or freezing) of flux line lattice in a single-crystalline sample of $Y_1Ba_2Cu_3O_{7-\delta}$. Such an oscillation was attributed to the elasticity of the vortex solid and the dynamic competition between pinning and depinning forces.

Similarly, Henderson *et al.* [30] demonstrated the importance of the type and frequency of applied current in the motion of vortex array which causes novel types of non-linear response by using fast transport measurements in single crystalline sample of superconductor $2H$-$NbSe_2$. In polycrystalline samples of $Y_1Ba_2Cu_3O_{7-\delta}$, Kiliç *et al.* [44] showed that a non-linear response to the long period BSW current reflects itself as regular sinusoidal-type voltage oscillations in the time evolution of sample voltage (i.e., $V - t$ curves). The experimental results were interpreted in terms of the defective flow of flux lines in a multiply connected network and semi-elastic coupling between the flux lines and pinning centers [44].

In the previous experimental studies, driving the vortex system by a transport current was the most convenient way of observing different dynamical instabilities and dynamic phase transitions. In addition to experimental studies, much effort has been devoted to numerical simulations of the current-driven vortex lattice in the presence of both periodic [23, 45, 46] and randomly distributed point-like pinning sites [47–50]. In the presence of driving force, the dynamic phase diagrams revealed the existence of several intermediate phases between the plastic and elastic regimes as a function of the spatial distribution and strength of the pinning sites [51, 52]. In parallel to numerical simulations, experimental studies were focused on the superconducting systems with well-arranged artificial square or triangular periodic pinning arrays in which the vortices could be trapped at individual pinning sites and also at interstitial regions between pinning sites [53, 54]. Recent developments in artificially engineered pinning structures [55] have brought a new physical insight in which the vortices interact with hole arrays of large radius. Thus, analysis of the systems (such as nucleation of vortices [56], formation of multiquanta vortices [57, 58] and multiple trapping of vortices inside the cavities which serve as strong pinning centers [59]) has attracted a lot of interest. In addition, the flux trapping capacity of hole defects and the effect of columnar defects on the arrangement of vortex lines inside the superconducting sample were also investigated experimentally [60, 61]. Silhanek *et al.* [62] showed that a thin film sample of Pb with artificially created square array of microholes is a good candidate to determine the number of trapped flux lines inside the cavity as a function of temperature and magnetic field strength.

Irreversibility effects in polycrystalline high-T_c superconducting (HTSCs) samples have been observed in magnetization [63–67] and magnetoresistance [61, 68, 69] measurements at low, moderate and high magnetic fields. The hysteresis effects in magnetovoltage measurements ($V - H$ curves) appear generally in the clockwise direction as the external magnetic field is swept up and down [68–70]. Low- and high-magnetic field irreversibilities observed in polycrystalline HTSCs samples have been interpreted in terms of flux trapping developing both intergranular and intragranular regions. In magnetovoltage measurements, it was shown experimentally that the time required to plot the whole cycle of the $V - H$ curve is important, thus, it becomes possible to investigate the relaxation effects in $V - H$ measurements by varying of the sweeping rate of the external magnetic field (dH/dt) [61, 71].

In this thesis, we investigated the time-dependent flux motion in a polycrystalline, superconducting $Bi_{1.7}Pb_{0.3}Sr_2Ca_2Cu_3O_x$ (BSCCO) having a drilled macroscopic cylindrical hole (CH) with a diameter of 0.5 mm. The experiments include $I - V$ measurements [35] as a function of current ramping rate dI/dt, $V - t$ curves and slow voltage oscillations, magnetovoltage ($V - H$ curves) measurements [61] as a function of magnetic field ramping rate dH/dt. In the experiments, first, the transport measurements were performed on the BSCCO sample without CH, then a CH was drilled through this sample and then the measurements were repeated on BSCCO sample with CH. This procedure enables us to compare the experimental results obtained for the BSCCO sample before and after drilling of the CH. The aim of this study is mainly to investigate the flux dynamics, flux trapping/de-trapping, and time effects in polycrystalline superconducting BSCCO sample with CH as functions of temperature T, transport current I, and magnetic field H.

The experimental results obtained for the BSCCO samples with and without CH exhibit several interesting physical behaviors at temperatures just below T_c. It is observed that the I - V curves of the BSCCO sample with CH show significant hysteresis effects, which depend on the magnitudes of dI/dt, the applied maximum current (I_{max}), and the external magnetic field. The hysteresis effects in the I - V curves are considered as a kind of superheated state of coherent motion of flux lines which try to keep their integrity. The analysis of I - V curves showed that CH acts as an attractive macroscopic pinning center for flux lines and inhibits the flux motion. Further, the discontinuities observed in the time evolution of the quenched state of the V - t curves are interpreted in terms of leaving of flux lines through CH. It is shown that dH/dt becomes an important parameter in the evolution of V – H curves, which determines the measured dissipation and the degree of relative irreversible effects. For different values of dH/dt, pronounced counterclockwise hysteresis effects appearing in asymmetric V – H curves are considered as a direct evidence of flux trapping in the CH. It is well known that, near the critical temperature (T_c), high-T_c superconductors are quite sensitive to low external magnetic field and a macroscopic CH drilled through the sample could be very promising to produce highly sensitive magnetic sensors by using these superconductors [72]. The noise problem in superconducting quantum interference devices (SQUIDs) can also be solved by introducing suitable holes of different sizes which trap the vortices. We suggest that our findings in this study will provide a direct contribution to designing of high performance SQUIDs.

CHAPTER 2

SUPERCONDUCTIVITY

Superconductivity was first discovered by Kamerlingh Onnes and Gilles Holst in 1911, while measuring the electrical resistance of mercury at low temperatures [73]. They found that, the dc resistance of mercury dropped abruptly to zero below 4.2 K. Thereafter, many investigations have shown that most of metals and metallic alloys have this property, namely, a transition from normal state to perfect conductivity. In 1957, Bardeen, Cooper and Schrieffer (BCS) reported the first successful microscopic theory of superconductivity [74].

Superconducting materials exhibit two characteristic features:

- Perfect electrical conductivity (the resistivity (ρ) becomes zero below a critical temperature T_c.)
- Perfect diamagnetism (i.e., the Meissner effect; the magnetic induction inside the superconductor is zero, $\vec{B} = 0$.)

2.1 Meissner effect

When a specimen is placed in an external magnetic field (below a critical field of H_c) and is cooled below the critical temperature T_c, the magnetic flux is expelled from the specimen, i.e. the material exhibits perfect diamagnetism. It is well known that a bulk type-I superconductor in a weak magnetic field acts as a "*perfect diamagnet*", with zero magnetic induction in the interior. Diamagnetism can be explained by induction of magnetization in a direction opposite to the external magnetic field:

$$\vec{B} = \vec{H} + 4\pi\vec{M} \ . \tag{2.1}$$

Here, $\vec{B}$ is the magnetic induction (or effective field inside the sample), $\vec{H}$ is external magnetic field (magnetizing field) and $\vec{M}$ is the magnetization induced in material. In type-I superconductors, the flux is repelled out of the sample and $\vec{B}$ becomes zero below T_c. In this case, the magnetic susceptibiliy $\chi = M / H$ of the sample is *-1/4π* (in CGS units). Negative susceptibility is an indication of diamagnetism, and the value *-1/4π* corresponds to the perfect diamagnetism. Above T_c, a transition from the superconducting state to normal state occurs as the magnetic flux penetrates into the sample. However, perfect diamagnetism can not be correlated to perfect conductivity ($\rho = 0$). The Ohm's law can be written as

$$\vec{E} = \rho\vec{J} \ , \tag{2.2}$$

where $\vec{E}$ is the applied electrical field, ρ is the electrical resistivity and $\vec{J}$ is the current density. The Faraday's law of induction states that the induced electromotive force is proportional to the negative of the time rate of change of the magnetic flux $\vec{B}$ through the loop. This is given as [75]

$$\vec{\nabla} \times \vec{E} = -\frac{1}{c}\frac{\partial \vec{B}}{\partial t} . \tag{2.3}$$

If $\rho = 0$, according to Ohm's law, the electrical field inside the sample must be zero ($\vec{E} = 0$). Thus, $\frac{\partial \vec{B}}{\partial t} = 0$ and, $\vec{B} =$ constant within the sample. This clearly proves the existence of two different possible states for a perfect conductor. Thus, its final state below the critical temperature T_c in the presence of the external field H ($< H_c$) depends on the history of the cooling process. However, a superconductor is perfectly diamagnetic for $T < T_c$ and $H < H_c$, and the transition to the superconducting state is perfectly reversible.

2.2 London equations and the two fluid model

The theoretical description of the Meissner effect was put forward by Fritz and Heinz London brothers by modifing the set of Maxwells' equations in 1935 in terms of "two fluid model" [73]. In this model, there are two charge carrier types coexisting in a superconductor below the critical temperature T_c and the total carrier density n_t is given as the sum of superelectron density n_s and normal electron density n_n

$$n_t = n_n + n_s = constant. \tag{2.4}$$

At a fixed temperature below T_c, there is a special ratio between the densities of the two carriers, as a consequence of two fluid model. However, the transport current has a determining effect on the dynamical process of carriers. When a current is passed through a superconducting sample, a dynamic competition between the carriers is produced depending on the magnitude of the applied current. At very low currents, it is supposed that only superelectrons contribute to the conduction and normal electrons do not take place in the conduction phenomena. As a consequence, no dissipation (or voltage developed in the direction of the transport current) is observed, hence, $\rho = 0$. On the other hand, the normal electron conductivity is given as $\sigma = \frac{n_n e^2 \tau}{m}$. Here, n_n is the density of normal electrons, e is the magnitude of the electron charge, τ is the relaxation time, and m is the electron effective mass. If an electrical current is carried by normal electrons in a superconducting sample, it naturally causes dissipation (i.e., a voltage drop is developed in the current direction).

The London equations successfully describe the Meissner effect. The first London equation relates the superconducting current to the applied electric field as follows [73]:

$$\frac{d\vec{J}_s}{dt} = \frac{n_s e^2 \vec{E}}{m} \quad , \quad \text{with} \qquad \vec{J}_s = -n_s e \vec{v}_s \tag{2.5}$$

$$\vec{J}_n = \sigma_n \vec{E} \, , \qquad \text{with} \qquad \vec{J}_n = -n_n e \vec{v}_n \, . \tag{2.6}$$

Here, $\vec{J}_s$ is the supercurrent density, and $\vec{J}_n$ is the normal current density, $\vec{v}_s$ and $\vec{v}_n$ are the mean velocities of the superelectrons and normal electrons inside the material, respectively. The total current density $\vec{J}$ is given by

$$\vec{J} = \vec{J}_s + \vec{J}_n \, . \tag{2.7}$$

The equation of motion of an electron in an electrical field $\vec{E}$ can be written as,

$$m \frac{d\vec{v}}{dt} = -e\vec{E} \, . \tag{2.8}$$

By substituting the supercurrent density equation into Equation (2.8), we obtain

$$\frac{d(-n_s e \vec{v}_s)}{dt} = -\frac{n_s e^2 \vec{E}}{m} \, . \tag{2.9}$$

The supercurrent $\vec{J}_s$ is connected to the magnetic induction $\vec{B}$ and by considering the Maxwell equations [75] after some straightforward algebra, we obtain the London equation

$$\nabla^2 \vec{B} = \frac{4\pi n_s e^2}{mc^2} \vec{B} = \frac{1}{\lambda_L^2} \vec{B}, \tag{2.10}$$

where $\lambda_L = \sqrt{\dfrac{mc^2}{4\pi n_s e^2}}$ (in CGS) is defined as the London penetration depth. This equation is seen to account for the Meissner effect because it does not allow a solution uniform in space, so that a uniform magnetic field cannot exist in a superconductor. That is $B(\mathrm{r}) = B_0$ = constant is not a solution of Equation (2.10) unless the constant field B_0 is identically zero [73]. The London eqution, which is purely classical, deals with electrodynamic properties of superconductors on a macroscopic scale and the solution of the London equation

$$B(r) = B(0)exp(-r/\lambda_L) \tag{2.11}$$

leads to an exponential decay of the external magnetic flux with distance r inside the bulk semi-infinite superconductor. Here, $B(0)$ is the magnetic field, which is parallel to the surface of the superconductor. The penetration of the magnetic flux into the sample is characterized by a parameter λ_L called as "London's Penetration Depth", and screening currents are induced within a distance related to λ_L (for type-I superconductors, $\lambda_L \cong 500$ Å) [73].

2.3 The Ginzburg - Landau theory

Despite the success of London theory in explaining the Meissner effect, it failed to explain some important phenomena, including the surface energy at the interface between the normal and superconducting regions (NS boundary), the critical magnetic field and the critical current of a thin film. The Ginzburg-Landau (GL) theory takes into account the quantum effects. The GL theory [76] is considered as the first phenomenological quantum theory of superconductivity and is based on the Landau theory of second order phase transitions. According to Landau [77], second order phase transitions occur when the state of a substance changes continuously, while its symmetry changes in a discontinuous manner. The second order phase transitions characterized by an order parameter. This implies the existence of an order parameter for a superconductor, which is nonzero at $T < T_c$ and zero at $T > T_c$. The effective wave function $\psi(r)$ of the superelectrons was considered as an order parameter by Ginzburg and Landau [76, 78]. The order parameter ψ for superconductors is defined as

$$\psi = \sqrt{n_s} e^{i\theta}, \tag{2.12}$$

where θ is the phase of the order parameter and $|\psi|^2$ is assumed to be equal to the density of the superelectrons n_s. The GL theory is consistent with the experimental results taken in the vicinity of the transition temperature T_c, and the free energy can be expanded in powers of ψ, which is very small in the vicinity of T_c [78],

$$F_s(r) = F_n(r) + \alpha|\psi|^2 + \frac{\beta}{2}|\psi|^4 + \frac{1}{4m}\left|\left(-i\hbar\vec{\nabla} - \frac{2e\vec{A}}{c}\right)\psi\right|^2 - \int_0^H \vec{M}\cdot d\vec{H}'. \tag{2.13}$$

Here, $\vec{A}$ is the vector potential, $\hbar$ is the Planck constant, α and β are phenomenological constants; $\alpha = \alpha_0(T - T_c)$ and $\beta > 0$ are related with transition and stability. $F_n(r)$ and $F_s(r)$ are the free energy densities of a material in the normal state and superconducting state, respectively. In order to find the minimum value of the free energy, we apply the variational method with respect to $\psi^*(r)$, which is the complex conjugate of $\psi(r)$,

$$\delta F_s(r) = \left[\alpha\psi + \beta|\psi|^2\psi + \frac{1}{4m}\left(-i\hbar\vec{\nabla} - \frac{2e\vec{A}}{c}\right)\psi \cdot \left(-i\hbar\vec{\nabla} - \frac{2e\vec{A}}{c}\right)\right]\delta\psi^* + c.c. \tag{2.14}$$

By means of integration by parts,

$$\int dV(\vec{\nabla}\psi)(\vec{\nabla}\delta\psi^*) = -\int dV(\nabla^2\psi)\delta\psi^* . \tag{2.15}$$

If $\delta\psi^*$ vanishes at the surface of the superconductor, so that

$$0 = \delta\int F_s(r)dV = \int dV\delta\psi^* \left[\alpha\psi + \beta|\psi|^2\psi + \frac{1}{4m}\left(-i\hbar\vec{\nabla} - \frac{2e\vec{A}}{c}\right)^2 \psi \right] + c.c. \tag{2.16}$$

If the expression in the square brackets is zero, so Equation (2.16) is satisfied. From this, we obtain the first equation of the GL theory [78]:

$$\alpha\psi + \beta|\psi|^2\psi + \frac{1}{4m}\left(-i\hbar\vec{\nabla} - \frac{2e\vec{A}}{c}\right)^2 \psi = 0 . \tag{2.17}$$

The GL theory is able to explain the magnetic properties of superconductors. For example, the GL theory introduced a special parameter κ which depends on the ratio of the penetration depth λ to the coherence length ξ which is correlated to superelectron pairs. This parameter is known as the GL parameter and it plays a key role in the determination of the surface energy at the NS boundary. According to the GL theory [78], the surface energy is found to be positive for conventional superconductors with $\kappa < 1/\sqrt{2}$. Abrikosov [79, 80] showed that the surface energy is negative at large GL parameter $\kappa > 1/\sqrt{2}$, and this implied the existence of a new type of superconductors having fairly different magnetic properties. Thereafter, Abrikosov named the pure superconductors as type-I superconductors and these new ones as type-II superconductors, which have an intermediate state above the Meissner state [80]. Later on, it was found that the predictions of GL theory and Abrikosov theory were consistent with experiments. The magnetization curves for type-I and type-II superconductors are given in Fig. 2.1. For a type-II superconductor, for $H < H_{c1}$ (the lower critical field), the material is in the Meissner state. For $H > H_{c1}$, the magnetic field lines penetrate partially into the sample in the form of quantized vortices and an intermediate (mixed) state consisting of normal and superconducting regions is formed. As the external magnetic field becomes equal to or higher than the upper critical field H_{c2}, the bulk superconductivity disappears completely.

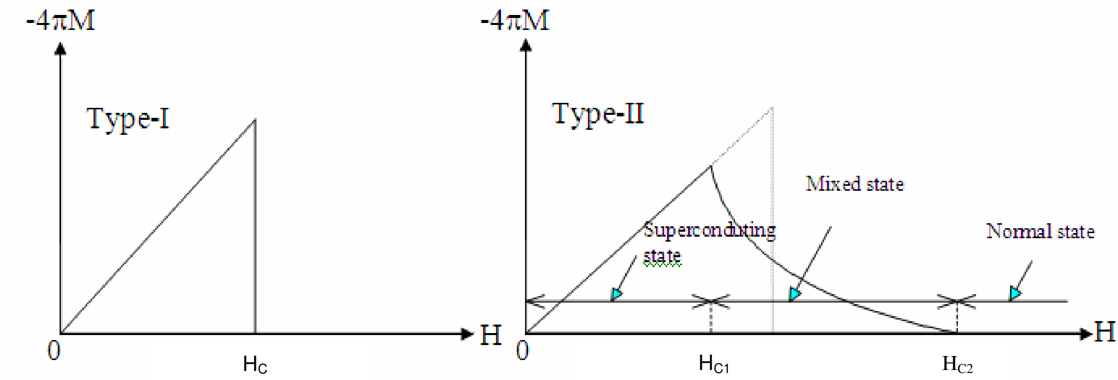

Figure 2.1 The magnetization curves for the type-I and type-II superconductors. Here, the H_c is the thermodynamic critical field where the superconductivity is destroyed above for type-I superconductors. H_{c1} and H_{c2} are lower and upper critical fields for type-II superconductors. Also, there is a mixed state where the superconducting and normal state regions co-exist in the phase diagram for type-II superconductors [80].

When the free energy density (Equation 2.13) is minimized with respect to the vector potential $\vec{A}$, the supercurrent equation (i.e., variation of $\vec{A}$ in a superconductor) or the second GL equation is obtained as [78]

$$\vec{J}_s(r) = -\frac{iq\hbar}{2m}\left(\psi^*\vec{\nabla}\psi - \psi\vec{\nabla}\psi^*\right) - \frac{q^2}{mc}\psi^*\psi\vec{A}. \tag{2.18}$$

Here q is the magnitude of wave vector. The supercurrent density $\vec{J}_s$ and the vector potential $\vec{A}$ in the superconductor can be described [75] as

$$\vec{\nabla}\times\vec{H} = \frac{4\pi}{c}\vec{J}_s(r) \qquad \text{and} \qquad \vec{B} = \vec{\nabla}\times\vec{A}. \tag{2.19}$$

The GL equations possess two scales. The coherence length ξ characterizes the variation of $\psi(r)$ with position and the penetration depth λ characterizes the variation of $B(r)$ with position inside the superconductor. Both ξ and λ are temperature dependent and are given as [78]

$$\xi(T) = \frac{\hbar}{\sqrt{2m^*\alpha(T_c - T)}} \qquad \text{and} \qquad \lambda(T) = \frac{c}{e^*}\sqrt{\frac{m^*\beta}{4\pi\alpha(T_c - T)}}, \tag{2.20}$$

where α and β are phenomenological constants defined in Equation (2.13). The value of m^* (=2m) and e^* (=2e) are twice the normal electron mass and electron charge, respectively. Both ξ and λ diverge at $T = T_c$.

2.4 Magnetic flux quantization

The quantization of magnetic flux in a superconductor was first predicted by F. London [78]. Let us place a superconducting ring in a magnetic field which is weaker than the first critical field ($H < H_{c1}$) at $T > T_c$. Since the superconducting ring is in the normal state, the magnetic flux lines pass through the interior of the ring: These flux lines can be trapped by applying the field cooled (FC) process to the ring: The temperature is decreased below the critical temperature of superconducting ring in an external magnetic field $H < H_{c1}$ and the magnetic field is turned off at a certain temperature below T_c. According to Faraday's law of induction, the instantaneous diminish of the magnetic field inside the ring produces a current to prevent the decrease in field. This induced current is persistent because the electrical resistance of the superconducting ring is zero and this persistent current is known as the superconducting current or a supercurrent. The external magnetic field is now zero and the flux lines generated by the persistent supercurrent are trapped inside the ring. The supercurrent density is given as [80],

$$\vec{J}_s = \frac{1}{c\Lambda}\left(\frac{\phi_0}{2\pi}\vec{\nabla}\theta - \vec{A}\right), \tag{2.21}$$

where $\Lambda = 4\pi\lambda^2/c^2$ and $\phi_0 = 2\pi\hbar c/2e$ is the magnetic flux quantum named as fluxoid.

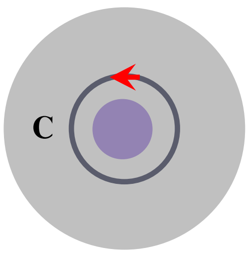

Figure 2.2 A superconductor with a hole. The arrow shows the direction of the supercurrent. The contour *C* encircles the hole.

In Figure 2.2, the contour C is chosen to encircle the hole and the distance between the contour and the internal surface of the hole is everywhere well in excess of the London penetration depth. Thus, the circulating supercurrent at any point of contour is taken zero, $\vec{J}_s = 0$. So that, the line integral is

$$\frac{\phi_0}{2\pi}\oint_C \vec{\nabla}\theta \cdot d\vec{\ell} = \oint_C \vec{A} \cdot d\vec{\ell} . \tag{2.22}$$

From the definition of the magnetic flux through closed loop (contour C),

$$\phi = \int \vec{H} \cdot d\vec{S} = \oint \vec{A} \cdot d\vec{\ell} , \tag{2.23}$$

and, then

$$\phi = \frac{\phi_0}{2\pi}\oint_C \vec{\nabla}\theta \cdot d\vec{\ell} . \tag{2.24}$$

The quantity θ is the phase of the order parameter (or wave function), and the wave function is defined as in Equation (2.12). In this case, it is necessary to decide on the value of phase θ, because, it is known that $\psi(r)$ is a single-valued function, while the phase θ is a multiple-valued function. Therefore, the change in θ after a full circle around the hole containing the magnetic flux must be integral multiple of $2\pi n$, where $n = 0, 1, 2\ldots.$

$$\oint_C \vec{\nabla}\theta \cdot d\vec{\ell} = 2\pi n . \tag{2.25}$$

Finally, one obtains that

$$\phi = n\phi_0 , \tag{2.26}$$

where $\phi_0 = \frac{hc}{2e}$. The phenomenon of magnetic flux quantization is a very important feature of superconductivity. It states that a superconducting coil can only trap magnetic flux equal to integral multiples of ϕ_0. Also, the flux quantum with charge $2e$ suggests that the supercurrent is carried by pairs of electrons.

2.5 Vortices in type-II superconductors

Abrikosov theory [79, 80] is based on the GL theory, and has a great importance on understanding the magnetic properties of type-II superconductors, which have an intermediate state (mixed) at magnetic fields in the range $H_{c1} < H < H_{c2}$. When H is higher than the upper critical field H_{c2}, the superconductivity is destroyed completely. In the intermediate state, the magnetic field penetrates within the superconductor in the form of quantized filaments of magnetic flux such that each flux tube contains one flux quantum (fluxoid). The fluxoid (or Abrikosov vortice) can be approximated by a long thin cylinder with a radius equal to the coherence length ξ and the central axis of the cylinder coincides with the external magnetic

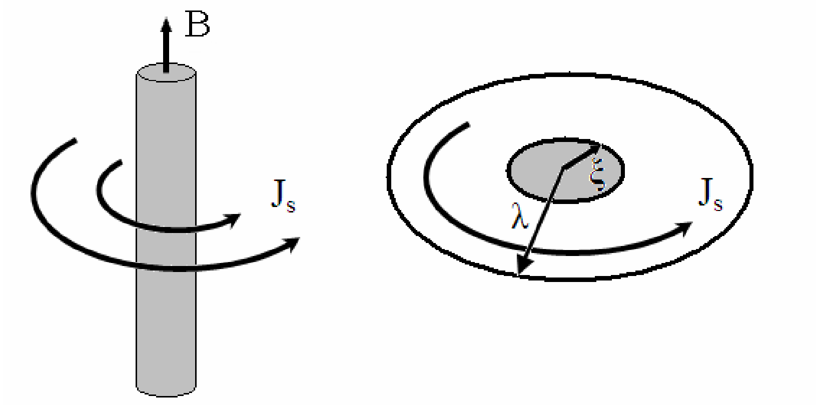

Figure 2.3 A schematic representation of flux tube (or fluxoid). Here λ is the penetration depth, ξ is the coherence length, B is the magnetic induction, J_s is the supercurrent.

field [78] (Fig. 2.3). Thus, each vortex filament has a normal core because the external field value is reached at the center of the normal core. This field induces a supercurrent (J_s) which is circulating around the normal core within a distance of the penetration depth λ. So that, the magnitude of the magnetic field decays as a function of distance away from the center of the vortex over a distance λ.

The magnetic field of a single isolated vortex can be obtained by solving the following equation [80]

$$\vec{H} + \lambda^2 \vec{\nabla} \times \left(\vec{\nabla} \times \vec{H} \right) = \hat{z} \phi_0 \delta(r), \tag{2.27}$$

where $\delta(r)$ is the delta function, and $\hat{z}$ is the unit vector along the axis of the vortex. The solution of this equation gives

$$H = \frac{\phi_0}{2\pi\lambda^2} K_0\left(\frac{r}{\lambda}\right), \tag{2.28}$$

where $K_0\,(r/\lambda)$ is zeroth order modified Bessel function of second kind [78].

As Figure 2.4 illustrates the density of Cooper pairs $|\psi|^2$ goes to zero and also the order parameter ψ is zero inside the vortex core [81]. The variation of magnetic induction B reaches its maximum value at the center of the vortex. The supercurrent J_s is circulating within a length scale given by λ.

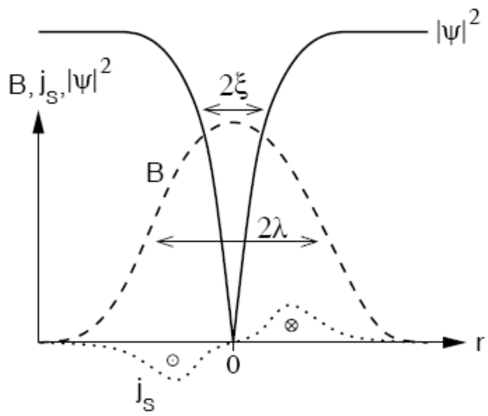

Figure 2.4 The spatial variation of the density of Cooper pairs $|\psi|^2$, the magnetic induction B, and the supercurrent J_s around the vortex center [81].

Up to now, we introduced the properties of an isolated single vortex. In fact, there are many vortices in the mixed state of a type-II superconductor. The increase in the number of these vortices leads to strong repulsive interactions between them. The interaction energy between two vortices separated by a distance r is given by [81]

$$U(r) = E_0 K_0\left(\frac{r}{\lambda}\right), \tag{2.29}$$

where $E_0 = \dfrac{\phi_0^2}{8\pi^2\lambda^2}$ is the energy scale. In the mixed state of a type-II superconductor, the vortices always tend to form a regular triangular lattice in the absence of disorder to minimize their energy [78, 80]. Without external forces, the form of the triangular lattice is kept to maximize the average lattice spacing which is defined as the characteristic parameter of flux line lattice.

2.6 Flux flow and flux pinning

The regular triangular vortex arrays (flux line lattice) start to move when an electrical current $\vec{J}$ is applied to a type-II superconductor. The external force exerted on each vortex is given by

$$\vec{F}_L = \frac{\phi_0}{c}\vec{J}, \tag{2.30}$$

where $\vec{F}_L$ is the Lorentz force and $\vec{J}$ is the transport current density [78]. In the absence of structural disorder, the vortices move in the sample under the influence of the Lorentz force. The motion of vortices produces an electric field due to the magnetic induction changing with time (see Equation (2.3)). This leads to a voltage dissipation equal to EJ, according to the Ohm's Law and manifests itself as a linear voltage increase in current-voltage ($I - V$) measurements.

In practice, for applied current below the critical current (I_c) where a maximum current that a superconductor can carry, the motion of vortices is always prevented by imperfections inside the superconductor, such as grain boundaries, twin planes. Most of these imperfections behave as pinning centers, and the flux pinning phenomenon plays a crucial role in the determination of the current carrying capacity of type-II superconductors. In a superconducting material, in which the imperfections (pining centers) are naturally present, as the transport current is increased above I_c, a measurable voltage dissipation occurs across the sample. In the experimental $I - V$ curves of superconductors, the critical current I_c is determined from the criteria at which the sample voltage or the induced electric field reaches 1 μV/cm. When the Lorentz force overcomes the pinning force F_p, the motion of flux lines is characterized by a flux flow regime [82]. Here, F_p is defined as a force, acting on a pinned flux line from a pinning center. On the other hand, if $F_p > F_L$, high enough transport current can flow in the superconductor without destroying the superconductivity.

It is well known that the free energy of the normal state exceeds the superconducting free energy by an amount of $H_c^2/8\pi$ per unit volume [78, 80]. When a vortex passes through a point defect with a size greater than ξ, it loses its core energy of $\frac{H_c^2}{8\pi}\pi\xi^2$ per unit length. This results in attraction of vortex to the defect center. In conventional type-II superconductors, not all defects (point defects such as vacancies or individual second-phase atoms) serve as an effective pinning center due to their small size as compared to the radius of vortex core. However, this case is not valid for the high-T_c superconductors because of their very small coherence length [9]. The point defects can be effective in inhibiting the vortex motion in high-T_c superconductors.

2.7 Flux creep

At finite temperatures ($T < T_c$), the pinned vortices are activated thermally and hence the vortices start hopping from one pinning site to another. This phenomenon is known as thermally activated flux creep and occurs at a measurable scale. The flux creep has a negative influence on the value of the critical current density in high-T_c superconductors.

Anderson [83] introduced a theory which connects the activation free energy of pinning regime to the hopping rate. According to this theory, the hopping rate of flux bundles is given as

$$\nu = \nu_o \exp\left[-U(J)/k_B T\right]. \tag{2.31}$$

where ν is the rate of flux hopping, ν_o is the attempt frequency, and k_B is the Boltzmann constant. $U(J)$ is considered as a pinning energy in transport measurements, because there is almost a static behavior of the flux lines; while, in magnetization measurements, $U(J)$ is taken as an activation energy since the flux lines are already in motion [63]. Also, the flux creep phenomenon manifests itself as a nonlinear increase in the sample voltage as a function of the driving current.

CHAPTER 3

TRANSPORT RELAXATION MODELS FOR $V - t$ CURVES OF HIGH-T_c SUPERCONDUCTORS

3.1 Superconducting glass model

The superconducting glass model [84] has been used to explain the magnetic relaxation of granular high-T_c superconductors. This model has some similarities to the thermally activated flux creep model. However, there are some difficulties in the interpretation of the magnetic properties of high-T_c superconductors by means of the thermally activated flux creep model. For example, memory effects observed in HTSCs could not be explained within the flux creep theory [6, 29]. The flux creep regime can not either explain the transition from the normal state to the superconducting state at small applied currents [84–88]. It was shown that the latter can be explained assuming pinning energies with different values distributed randomly through the sample [84]. The difference in the energy barriers between the neighboring states is small, while the difference between the more distant barriers is higher. Such barrier energy distribution leads to the concept of the superconducting glass model. The vortices can overcome easily the neighboring low barriers, however, fall in a deeper barrier due to the thermal activation. This model also provides useful information about the decay of the sample voltage of both zero-field cooling and field cooling of the sample below T_c [84].

The superconducting glass model is based on the relaxation of remanent magnetic moment in spin glasses [89], and has been used to explain the time decay of the magnetic susceptibility of La-based HTSCs by Müller *et al.* [85]. Since then, the magnetic behavior of HTSCs has been investigated by other researchers [90–93]. In the model used for spin glasses, it has been shown that the remanent magnetic moment of the sample cooled in an applied magnetic field decays exponentially with time after the applied magnetic field is turned off. Müller *et al.* [85] demonstrated that the magnetic susceptibility data in high-T_c La_2BaCuO_{4-y} superconductor measured at different magnetic fields show all features expected for a superconducting glassy state: The time decay of the magnetic susceptibility was exponential as in the case of the spin glasses. The superconducting glass model has also been used [84] to explain the anomalous time decay of the electrical resistivity in polycrystalline YBCO sample. In the latter, the sample voltage over the whole time interval is described well by

$$V(t) - V_0 = A_k \exp(-t/t_0), \tag{3.1}$$

where A_k is a constant, and t_0 is a characteristic time which depends on the applied magnetic field and temperature.

3.2 Modified flux-flow and resistive weak-links models

In order to characterize the relaxation effects in transport measurements of high-T_c superconductors, the modified flux-flow and resistive weak-link models have been proposed [94]. When the Lorentz force F_L overcomes the pinning force F_p , the motion of the flux lines changes into a viscous flow character from flux creep motion, and the flux line velocity can be written as [82, 95, 96]

$$v_L = 1/\eta(F_L-F_p). \tag{3.2}$$

Here η is the viscous drag coefficient of the medium. At transport currents greater than the critical current (I_c) of the sample, the voltage V developed across the sample in the direction of the transport current can be written as [94]

$$V = \frac{L}{S}\rho_f\left[I - I_c(H)\right]. \tag{3.3}$$

Here ρ_f is the flux flow resistivity, L is the distance between the voltage contacts, S is the area of the cross section perpendicular to the current, and I_c is the critical current which depends on the applied magnetic field and temperature.

In the resistive weak link model, it is assumed that the effective resistivity of the weak link system can be represented by [94]

$$\rho = \rho_w\left[I - I_c(H)\right]^{p-1} . \tag{3.4}$$

Here ρ_w is the resistivity of the weak-links, and p is the exponent which depends on the applied magnetic field and temperature. Using the magnetic field dependence of I_c (i.e., $I_c(H) \propto 1/H$) and assuming that the decay of magnetization (M) with time is logarithmic, both models predict a logarithmic time dependence of the sample voltage $V(t)$ [94]:

$$V(t) = V(0)\left[1 - \frac{k_B T}{U_0}\ln(t/t_0)\right] \tag{3.5}$$

Here, U_0 is the activation energy and $t_0 \sim 1/f_0$ is the characteristic time. There is a close similarity between the expression of V(t), derived for the transport relaxation (Equation (3.5)), and the expression of magnetization M(t) for the magnetic relaxation as derived [97, 98] from the classical Anderson-Kim theory:

$$M(t) = M(0)\left[1 - \frac{k_B T}{U_0}\ln(t/t_0)\right] \tag{3.6}$$

where $M(0)$ is the value of magnetization at $t = 0$.

3.3 Two-kinds of flux creep model

Recently, Ma *et al.* [99] developed a new model, known as two-kinds of flux-creep model, which describes the relaxation effects in transport measurements in high-T_c superconductors. This model treats the case when both transport current and external magnetic field are simultaneously applied to the sample. The model is essentially based on the flux creep theory, and considers two kinds of fluxes: one of them is the flux which decreases with time (i.e., the relaxation flux), while the other is the conventional flux which does not vary with time. In the creep of the relaxation flux under the Lorentz force, the transport current density J_t develops an electrical field E_i and hence a magnetization current density J_i; while the conventional flux produces an electrical field E_c. The total induced electrical field is then $E = E_i + E_c$. Further theoretical treatment by considering the logarithmic $U – J$ relationship [100] gives a compact formula for time dependence of the electrical resistivity $R_{ff}(t)$ in high-T_c superconductors. In the usual slab geometry, the conventional flux creep under the influence of magnetization current density J_i governs the decrease of J_i, according to the rate equation:

$$\frac{dJ_i}{dt} = A_s \exp(-U_i / k_B T) \tag{3.7}$$

where A_s is a constant, $U_i = U(J_i / J_{c0})$, is the effective pinning energy of the conventional flux that creeps under the Lorentz force of J_i, and J_{c0} is the critical current density. The logarithmic $U – J$ relation is expressed as [100]

$$U(J_i) = U_0 \ln(J_{c0} / J_i)\,. \tag{3.8}$$

Further theoretical treatment [99] by taking the logarithmic $U – J$ relation gives a useful formula for the time dependence of electrical resistivity:

$$R_{ff}(t) = R_0 + R_{ti}(0)[1 + t / t_0]^s \tag{3.9}$$

Here, $R_0 = E_c/J_t$, $R_{ti}(0)$ is the resistivity produced by the creep of the relaxation flux at $t = 0$. The exponent s is a function of U_0/k_BT, and t_0 is a characteristic time. Direct comparison [99] shows that there is a reasonable agreement between the experimental results obtained for the thin film samples of $Gd_{0.8}Y_{0.2}Ba_2Cu_3O_7$

epitaxially grown on (100) YSZ substrate and Equation (3.9). The equation of the relaxation resistivity (Equation (3.9)) in two-kind of flux-creep model suggests that the sample voltage changes with time as

$$V(t) \sim V(0)(1+t/t_0)^s. \tag{3.10}$$

CHAPTER 4

SAMPLE PREPARATION AND EXPERIMENTAL SET-UP

4.1 Preparation of bulk superconducting $Bi_{1.7}Pb_{0.3}Sr_2Ca_2Cu_3O_x$ (BSCCO) samples

Polycrystalline $Bi_{1.7}Pb_{0.3}Sr_2Ca_2Cu_3O_x$ (BSCCO) samples were prepared from high purity powders of Bi_2O_3, $CaCO_3$, $SrCO_3$, PbO and CuO (Aldrich Co.) by the conventional solid state reaction method [101]. Appropriate amounts of powders were mixed and grinded in alcohol using agata mortar for 1 hour. The mixed powder was put in liquid ammonium nitrate at 180 °C in order to obtain a homogenous mixture, and the solution was kept at this temperature for 24 hours. Then, the ammonium nitrate in the solution was evaporated at 600 °C for 1 hour which was followed by annealing at 500 °C for 5 hours in a microprocessor controlled tube furnace (Carbolite CTF 12/100/90). The mixed powder was pressed into disk shape of 16 mm in diameter under pressure of 300 MPa (Lightpath Optical (UK) LTD). The pellets were sintered at 850 °C for 75 hours. The pellets were re-grounded in alcohol for 1 hour and re-pelleted under the same pressure. The final heat treatment was carried out by sintering the pellets at 840 °C for 96 hours. Thus, the Bi-2223 phase is obtained [61].

One of the BSCCO pellets was cut carefully to obtain a rectangular sample of length l = 6.35 mm, width w = 3.4 mm, and thickness d = 1.3 mm. Then, four conducting pads were placed onto the sample by using silver paint and annealed for 3 hours at 150 °C under oxygen atmosphere to reduce the possible Joule heating effect which may occur at current leads. Pure copper wires were attached to the pads using silver paint. The contact resistance as measured using the three point method was in the order of 10^{-2} Ω below T_c and 10^{-1} Ω at room temperature. After all transport measurements were carried out on this BSCCO sample, a macroscopic cylindrical hole (CH) of 0.5 mm diameter was drilled through the same BSCCO sample as shown in Fig. 4.1. All transport measurements were again carried out on the same BSCCO sample after drilling CH.

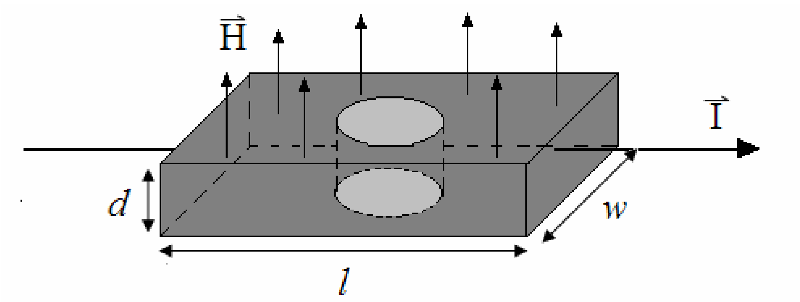

Figure 4.1 The BSCCO sample after a cylindrical hole (CH) was drilled. Here, $\vec{H}$ is the applied magnetic field and $\vec{I}$ is the transport current. The sample has dimensions of length l = 6.35 mm, width w = 3.4 mm, and thickness d = 1.3 mm.

4.2 Experimental set-up

The transport measurements were carried out using a standard four-point method in a closed-cycle refrigerator (Oxford Instruments, CCC1104). The block diagram of the experimental set-up is shown in Fig. 4.2. In the experiments, a nanovoltmeter (Keithley 2182A, with a resolution 1 nV) and a current source (Keithley 6221) were used to measure the sample voltage and to apply the driving current, respectively. The temperature was recorded by a calibrated 27 Ohm Rhodium-Iron thermocouple (Oxford Instruments, Calibration number 31202), and a temperature stability better than 10 mK was maintained during the measurements (Oxford Instruments, ITC – 503 temperature controller). The critical temperature of the BSCCO sample obtained from resistance vs temperature measurements at zero magnetic field was $T_c \cong 105$ K and was confirmed by ac susceptibility measurements (made at TÜBİTAK, Gebze, İZMİT) by using a SQUID magnetometer (QUANTUM DESIGN, MPMS XL) with 1 Oe amplitude ac magnetic field.

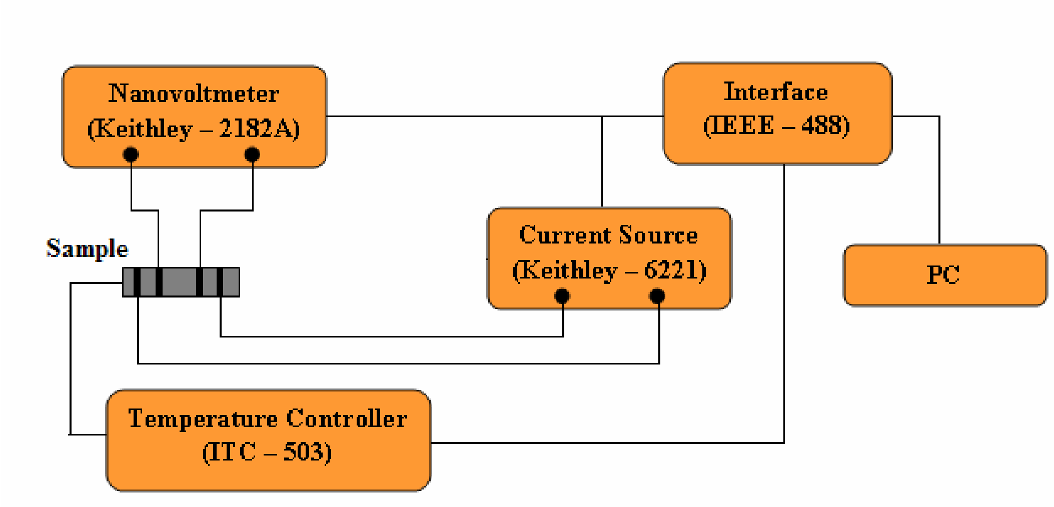

Figure 4.2 The block diagram of the measurement set-up. All measurements were carried out under computer control via IEEE - 488 interface.

The magnetic field was generated by an electromagnet (Oxford Instruments, N100). In the $V - H$ measurements, the external magnetic field ($\vec{H}$) was oriented perpendicular to the transport current ($\vec{H} \perp \vec{I}$) (see Fig. 4.1).

In all measurements, the nanovoltmeter was triggered for a maximum of $6^{1/2}$ digits, and its buffer was read directly within the integration time of 100 ms, in order not to cause any artificial effects. The measured sample voltage was the average value of 5 readings for each data point.

To determine the critical current density (J_c) of the BSCCO samples, the current-voltage (I – V) characteristics were measured at temperatures just below the critical temperature ($T_c \cong 105$ K). The critical current density of the samples, whose data are presented in this study, was ~ 0.35 A/cm^2, at T = 102 K and current sweep rate dI/dt = 1.25 mA/s, as determined by using the 1 μV/cm criterion.

In this study, the current sweep rate (dI/dt) is obtained by dividing the maximum current range (0 – I_{max}) with the number of the data points (i. e., N = 10, 20, 40, and 80). Thus, the current sweep rate and the measurement time for each I – V curve are determined. In the measurements carried out on both BSCCO samples with CH and without CH, we used two different procedures: the standard procedure and the reverse procedure. In the standard procedure: the current is first increased from zero to a maximum value I_{max} with a given value of dI/dt (current-increase (CI) branch), then, the current was decreased from I_{max} to zero with the same value of dI/dt (current-decrease (CD) branch). In the reverse procedure: the I – V curves were measured first by applying I_{max} to the sample and then decreasing the current from I_{max} to zero (current-decrease (RCD) branch), then, the current is increased from zero to I_{max} with the same value of dI/dt (current-increase (RCI) branch).

The time evolution of the sample voltage (V – t curve) was measured at zero applied magnetic field by applying dc or bidirectional square wave (BSW) (with long period (P_I) and different amplitudes) current to the sample. The current source (Keithley 6221) and the nanovoltmeter (Keithley 2182A) are capable to produce BSW currents and to read extremely low voltages with high precision. Slow transport relaxation measurements (V – t curves) were carried out using dc currents by recording the variation of the sample voltage with time. In these measurements, an initial dc current I_1 was applied for about 60 s and, then, a quenched state is created by interrupting the current or reducing it to a given finite value I_2 for the rest of the relaxation process.

The magnetovoltage measurements (V – H curves) were carried out as functions of temperature, transport current (I), and sweep rate (dH/dt) of the external magnetic field (H) for the configuration $\vec{H} \perp \vec{I}$. In order to determine the time effects in the V – H curves, the value of dH/dt was of crucial importance.

CHAPTER 5

EXPERIMENTAL RESULTS

We performed detailed transport and magnetovoltage measurements on polycrystalline $Bi_{1.7}Pb_{0.3}Sr_2Ca_2Cu_3O_x$ (BSCCO) sample before and after drilling a cylindrical hole (CH) of 0.5 mm diameter through the sample. Hereafter, the two BSCCO samples studied will be referred as the *sample without CH* and the *sample with CH*, respectively. The effects of CH on transport measurements are assessed by a comparing the experimental results of the sample with CH with those of the sample without CH.

5.1 Resistivity measurements on the BSCCO samples

5.1.1 Resistivity versus temperature measurements

The resistivity versus temperature ($\rho - T$) curves of the BSCCO samples with and without CH for an applied current I = 2 mA and zero magnetic field are presented in Figure 5.1. The $\rho - T$ curves show metallic behaviour in the normal state: the resistivities of both samples decrease with decreasing temperature until the superconducting transition occurs at $T_c \cong 105$ K. The normal state resisitivity of the sample without CH is higher than that of the sample with CH. This could be due to the decrease of the sample volume since some amount of the BSCCO material is removed by drilling the CH. However, the normal to superconducting phase transition occurs approximately at the same temperature for both samples. The value of the critical temperature T_c value was taken as the temperature at which the derivative of the resistivity with respect to temperature ($d\rho/dT$) versus T graph showed a peak (see the inset in Fig. 5.1). At zero applied magnetic field, the critical temperature T_c of the samples with and without CH was approximately 105 K. The transition from the normal to the superconducting phase at about 105 K indicates that the desired Bi-2223 phase is produced successfully.

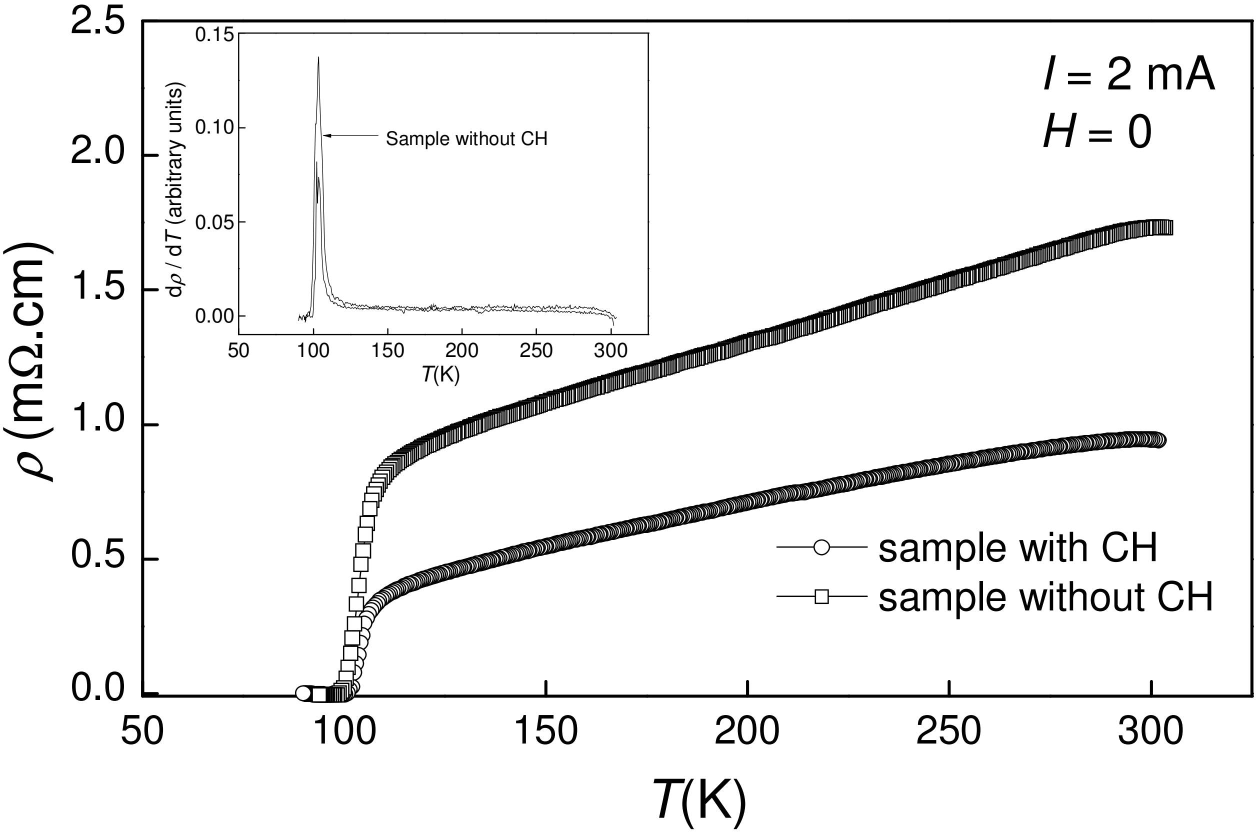

Figure 5.1 Resistivity versus temperature curves of the BSCCO samples with and without CH at zero applied magnetic field ($H = 0$). The inset shows the derivative of resistivity with respect to temperature, $d\rho/dT$.

5.1.2 Resistivity measurements as a function of transport current

The resistivity measurements on the sample without CH were carried out as a function of the transport current in a range from 5 to 40 mA at zero applied magnetic field. A set of Arrhenius plots of the resistivity vs temperature curves is presented in Figure 5.2.

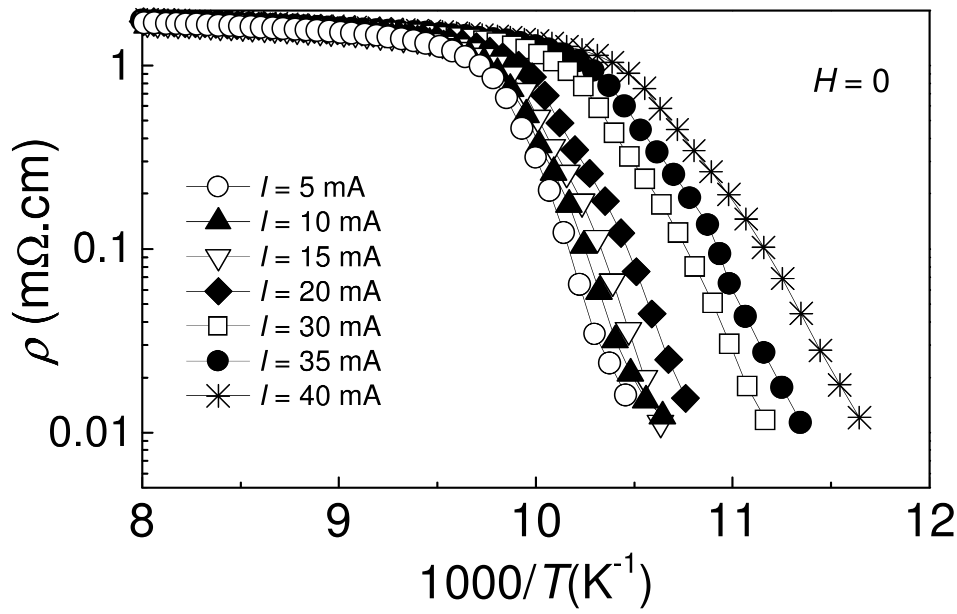

Figure 5.2 Arrhenius plots of the ρ(T) data for BSCCO sample without CH obtained at various transport currents I = 5, 10, 15, 20, 30, 35, 40 mA and zero magnetic field (H = 0).

Arrhenius plot of ρ(T) curves provides a useful method to determine the flux pinning energy U_0 as a function of transport current or external magnetic field. Assuming that the temperature dependence of electrical resistivity can be described [102] by thermally activated processes are in effect,

$$\rho \approx \rho_0 \exp\left(-\frac{U_0}{k_B T}\right), \tag{5.1}$$

where ρ_0 is the electrical resistivity at T = 0 K and U_0 is the effective flux pinning energy which depends on temperature, magnetic field and transport current. The value of U_0 can be extracted from the slope of the linear part of the Arrhenius plot at low temperatures. Figure 5.3 shows the U_0 values as determined from the data given in Fig. 5.2 (ln (ρ) *vs.* 1000/*T* plots).

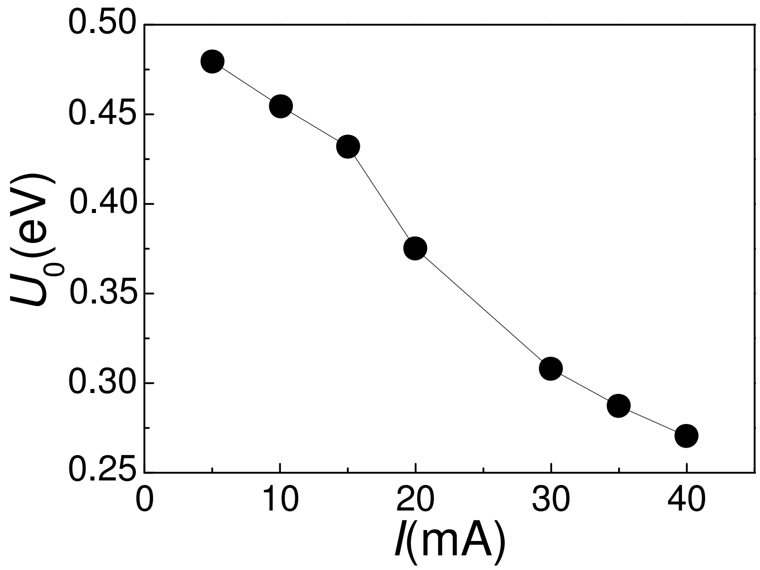

Figure 5.3 The variation of the effective flux pinning energy U_0 as a function of the transport current for BSCCO sample without CH. The values of U_0 are obtained from the Arrhenius plots given in Fig. 5.2. The solid line is a guide to the eye.

The effective flux pinning energy decreases with increasing the transport current as would be expected. This experimental finding suggests that there is a close corelation between the pinning potential and the transport current and that the height of the pinning potential is lowered at sufficiently high transport currents.

5.2 Hysteresis effects in the *I* – *V* curves of the sample with CH for different current sweep rates

Figure 5.4(a) shows a set of hysteretic, non-linear *I* – *V* curves for the BSCCO sample with CH measured for different sweep rates (d*I*/d*t*) in a range from 0.156 to 1.25 mA/s at T = 102 K and zero magnetic field (H = 0). Each *I* – *V* curves consists of two branches: *(i)* The current-increase (CI) branch on which the current is increased from zero to a maximum value I_{max} and *(ii)* the current-decrease (CD) branch on which the current is decreased from I_{max} to zero.

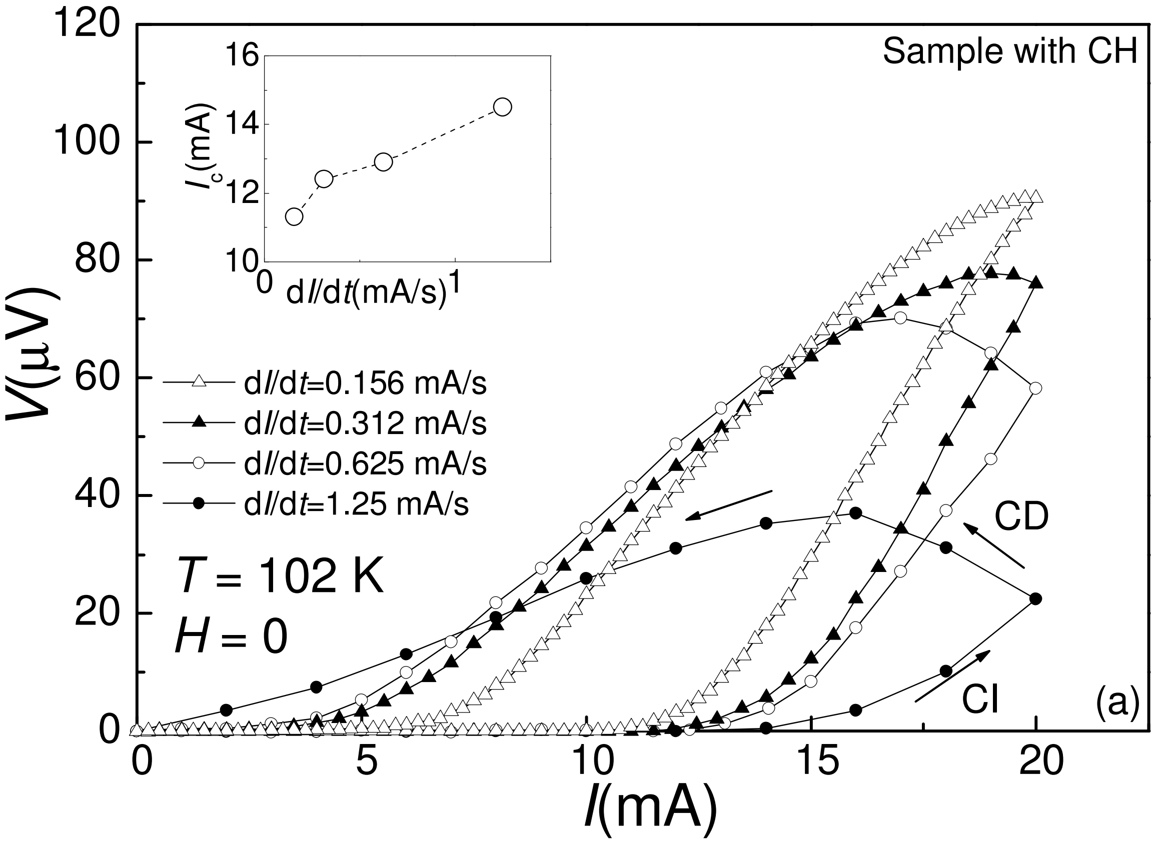

Figure 5.4(a) A set of hysteretic I – V curves for the BSCCO sample with CH measured at different values of dI/dt = 0.156, 0.312, 0.625, and 1.25 mA/s at T = 102 K and H = 0. The inset shows the variation of the critical current I_c with dI/dt. The arrows show the direction of sweeping of the applied current.

There are marked differences between the CI and CD branches of the I – V curves. The voltage dissipation observed in the CI branch is lower than that in the CD branch, and lineshapes of the two branches are different. For both branches, the measured voltage dissipation depends on the current ramping rate, which is possibly related to the relaxation effects intervening during the experiment. In addition, the critical current (I_c) corresponding to the CI branch increases with increasing of dI/dt (see the inset in Fig. 5.4(a)) indicating larger current sweep rates result in an enhancement in I_c. By contrast, the CD branch remains in the normal (resistive) state and the voltage values, which are above the 1 μV criteria, shift to low currents with increasing dI/dt. Thus, the difference in measured voltage dissipation between the CI and CD branches leads to the strong hysteresis effects in I – V curves.

In order to study the effect of external magnetic field (H) on the I – V curves, the measurements in Fig. 5.4(a) were repeated under the same experimental conditions by applying magnetic field oriented perpendicular to the transport current I ($\vec{H} \perp \vec{I}$). Figure 5.4(b) presents the I – V curves measured at H = 8 mT for current sweep rates ranging from 0.156 to 1.25 mA/s. The I – V curves exhibit similar features as those in Fig. 5.4(a). However, due to the external magnetic field, there are some differences to be noted. First, the measured voltage dissipation increases with H, and when the dissipation rate is enhanced considerably at high currents when compared to the case with H = 0. Second, the non-linearity of the I – V curves still persists although the I – V curves remain essentially in the normal state over whole current range considered.

It should be noted that the I – V curves measured at H = 0 (Figs. 5.4(a)) and at H = 8 mT (Fig. 5.4(b)) have some common features. For instance, the I – V curves in Figs. 5.4(a) and 5.4(b) show that the voltage corresponding to the CD branch first tends to increase as the current is started to decrease from I_{max} (= 20 mA) and passes through a broad maximum which becomes more prominent for low sweep rates. Then, the voltage decreases non-linearly with further decrease in the current.

Another common feature of these $I - V$ curves in Figs. 5.4(a) and 5.4(b) is the strong hysteresis effect upon cycling the transport current. In order to provide a quantitative measure of the hysteresis effect, the area (A) enclosed between the CI and CD branches was calculated for each $I - V$ curve measured at $H = 0$ and $H = 8$

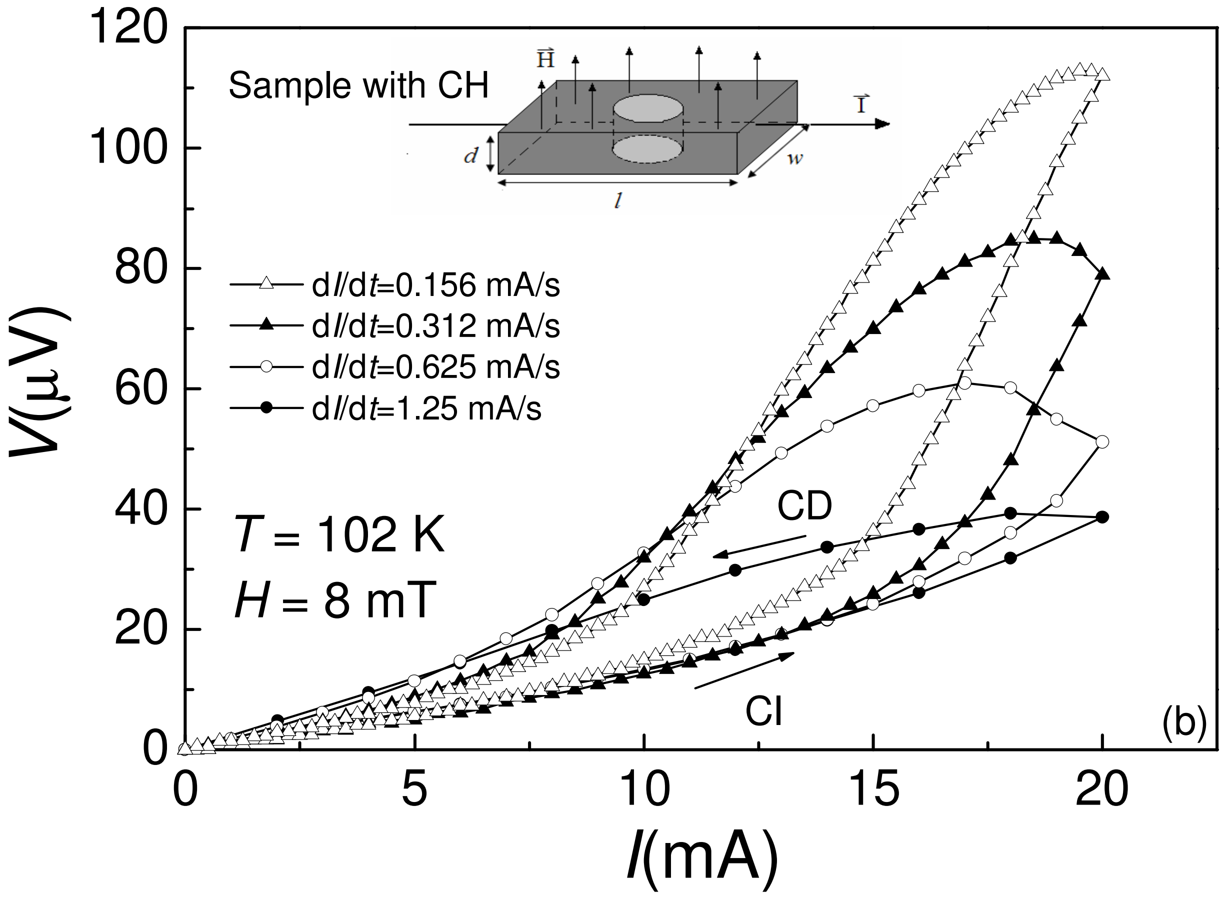

Figure 5.4(b) $I - V$ curves of the BSCCO sample with CH measured at the same experimental conditions in Fig. 5.4(a), but under $H = 8$ mT. The arrows show the direction of sweeping of the applied current.

mT as a function of dI/dt and then normalized to the area at the zero-field I – V curve measured at dI/dt = 1.25 mA/s. The Figure 5.5(a) shows the normalized area as a function of dI/dt. The width of hysteresis loop $\Delta V = (V_{CI} - V_{CD})$ was determined from the I – V curves given in Figs. 5.4(a) and 5.4(b) at a fixed current I = 15 mA and plotted as a function of dI/dt as shown in Figure 5.5(b). Here V_{CI} and V_{CD} are the voltage values corresponding to the CI and CD branches, respectively.

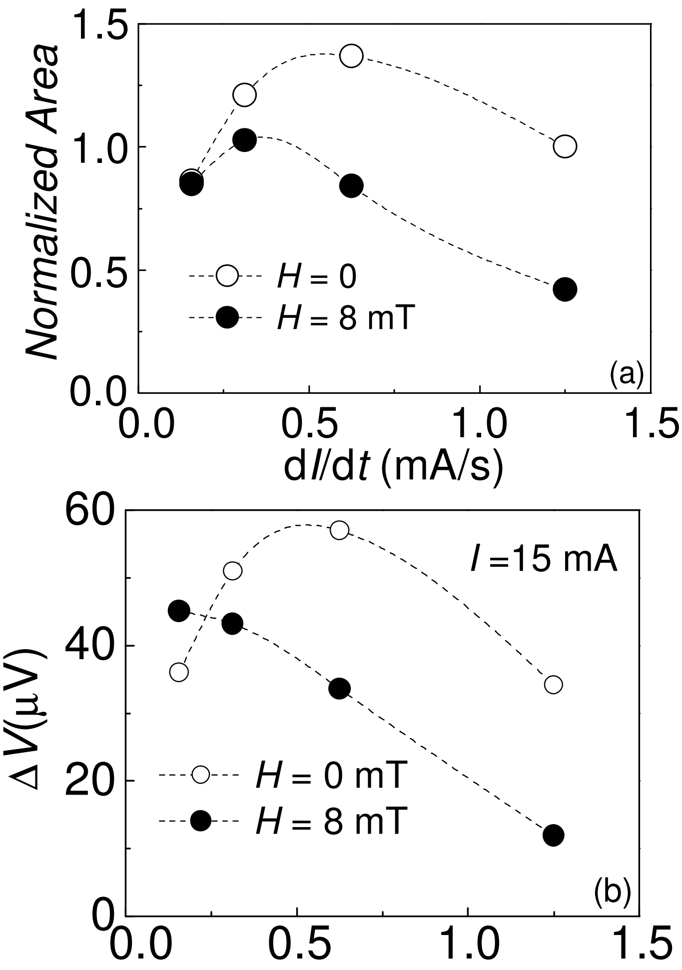

Figure 5.5 (a) The normalized area of the I – V curves (in Figs. 5.4(a) and 5.4(b)) as a function of dI/dt. **(b)** The width ΔV of the hysteresis loop at a fixed current of 15 mA extracted from the I – V curves (in Figs. 5.4(a) and 5.4(b)) as a function of dI/dt.

The hysteresis effect (i.e., the normalized area between the CI and CD branches) first increases, passes through a maximum and, then, decreases with increasing dI/dt. The application of external magnetic field of 8 mT leads to a decrease in the hysteresis effects as compared to that at zero magnetic field. We note that the width of the hysteresis loop also varies depending on the magnitudes of the applied current and dI/dt (Fig. 5.5(b)). Under H = 8 mT, the hysteresis effects (ΔV) decrease with increasing of dI/dt; whereas, at H = 0, ΔV increases first slightly with dI/dt at low values of dI/dt, and then a decrease in ΔV is observed.

5.2.1 The effect of the maximum current (I_{max}) on the I – V curves

Figure 5.6 shows a set of I – V curves of the BSCCO sample with CH measured for different sweep rates (dI/dt) from 0.312 to 1.25 mA/s at 102 K and zero field (H = 0). The experimental conditions are the same as those for the I – V curves presented in Fig. 5.4(a), except the maximum current I_{max} is now raised from 20 to 30 mA. We note that, in addition to some similarities between the I – V curves in Fig. 5.4(a) and those in Fig. 5.6, there are marked differences. Increasing I_{max} from 20 to 30 mA causes an enhancement in the measured voltage dissipation, and the hysteresis effects (i.e., the width of I – V loops) become more prominent. We also note that the difference between the voltage dissipations at I_{max} decreased somewhat as a function of dI/dt.

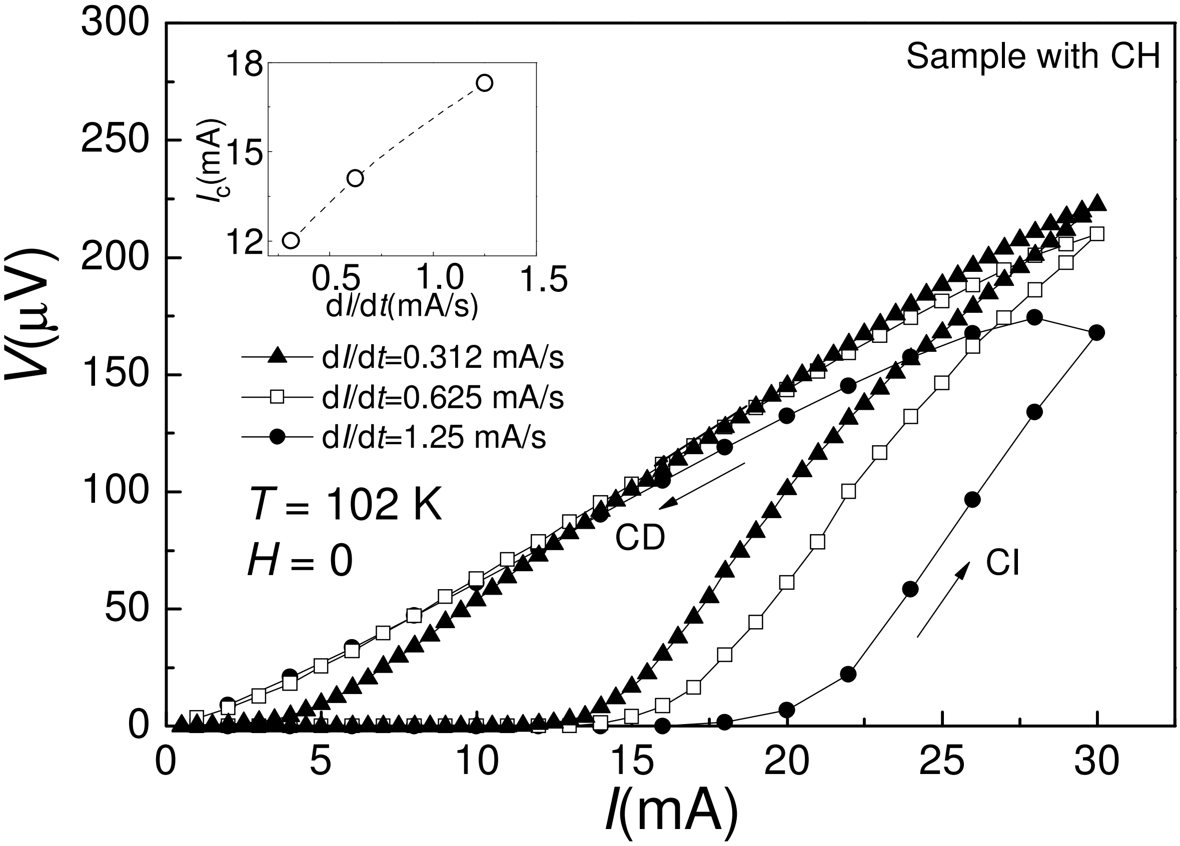

Figure 5.6 A set of $I - V$ curves of the BSCCO sample with CH measured for different values of dI/dt = 0.312, 0.625, 1.25 mA/s at T = 102 K and H = 0 for a maximum current I_{max} = 30 mA. The inset shows the variation of I_c with dI/dt. The arrows show the direction of sweeping of the applied current.

The inset in Fig. 5.6 shows the dI/dt dependence of the critical current (I_c) determined for the CI branch. I_c increases with increasing dI/dt, a behaviour similar to that found from the $I - V$ curves at I_{max} = 20 mA (see inset in Fig. 5.4(a)). The I_c values extracted from the $I - V$ curves in Figs. 5.4(a) and 5.6 are approximately equal in spite of the different values of I_{max}.

Figure 5.7 shows the $I - V$ curves of the BSCCO sample with CH measured for different values of dI/dt at T = 102 K and H = 4 mT. The strong hysteresis effects and the non-linearity in the $I - V$ curves still persist in the presence of an external magnetic field of 4 mT.

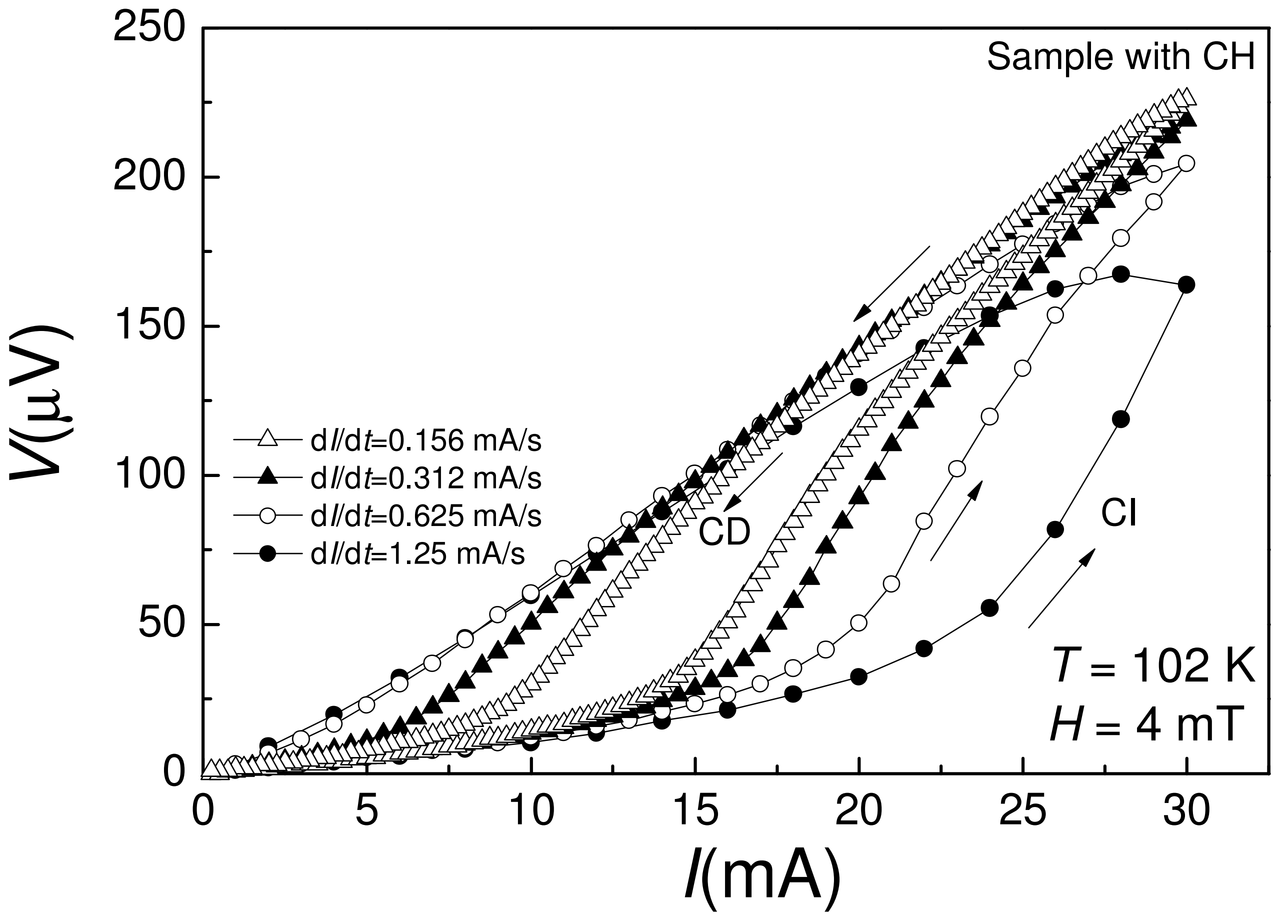

Figure 5.7 I – V curves of the BSCCO sample with CH measured for different values of dI/dt (= 0.156, 0.312, 0.625, and 1.25 mA/s) at T = 102 K and H = 4 mT for the maximum current I_{max} = 30 mA.

5.3 Hysteresis effects in the I – V curves of the sample without CH for different current sweep rates

In the following, we present the results of transport measurements carried out on the BSCCO sample without CH. Figures 5.8(a) to 5.8(c) show the I – V curves measured at T = 102 K and H = 0 for different sweep rates from dI/dt = 0.312 to 1.25 mA/s.

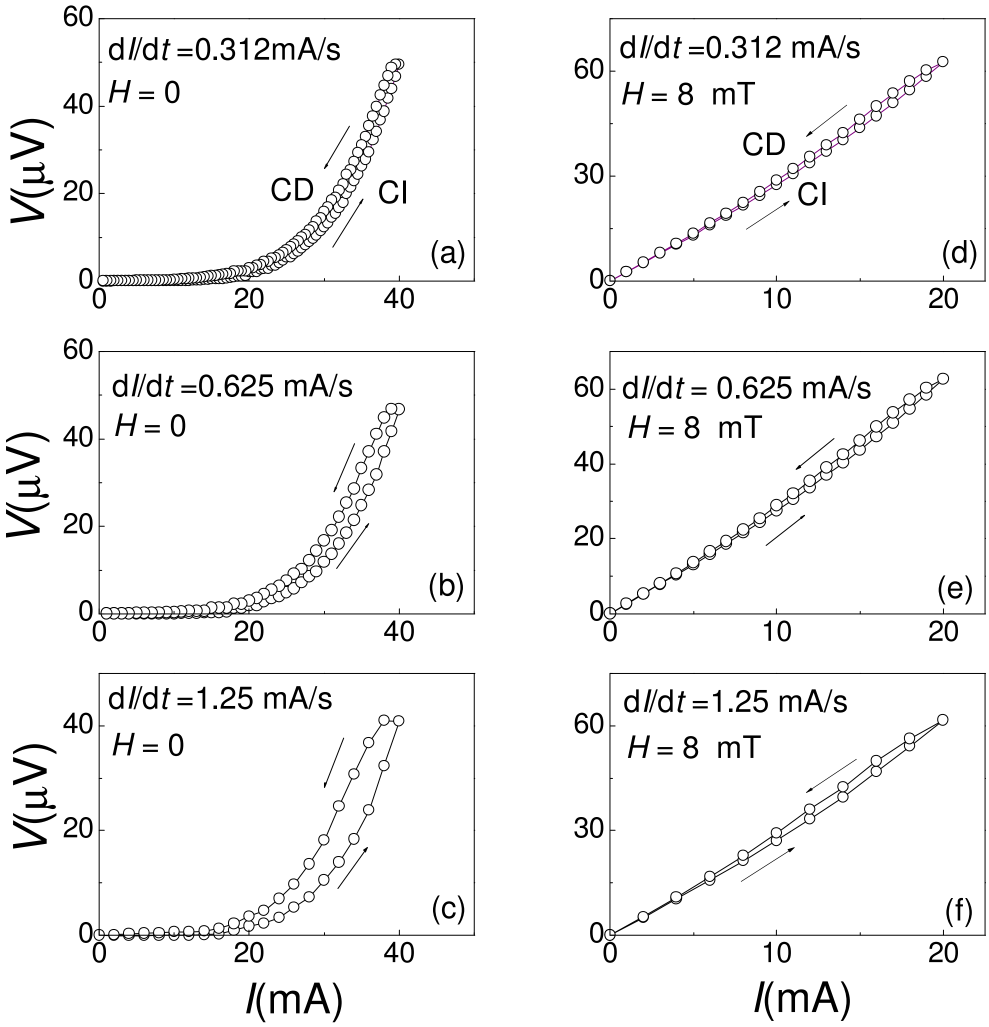

Figure 5.8 The I – V curves of the BSCCO sample without CH measured at T = 102 K and H = 0, for various current sweep rates (dI/dt) from 0.312 to 1.25 mA/s with I_{max} = 40 mA **(a)** to **(c)**; and H = 8 mT for I_{max} = 20 mA **(d)** to **(f)**. The arrows show the direction of sweeping of the applied current.

We observe the usual nonlinear behaviour of the I – V curves, which depends on the value of dI/dt. As dI/dt is decreased from 1.25 to 0.312 mA/s at H = 0, the width of the hysteresis loops decreases. Regardless of the current sweep rate, the CI branch is less dissipative than the CD branch. A comparison of the experimental data presented in Figs. 5.8(a) and 5.8(c) with those in Figs. 5.4(a) and 5.4(b), respectively shows that there are several pronounced differences between the $I - V$ curves of samples with CH and without CH, which can be due to the CH drilled through the sample. First, the presence of CH makes the transport measurements more dI/dt dependent; second, it enhances the hysteresis effects in $I - V$ curves and increases the dissipation in CD branch. The differences between the $I - V$ curves of the sample with CH and that without CH become more significant in the presence of an external magnetic field. When $H = 8$ mT is applied to the sample without CH, the hysteresis effects in $I - V$ curves almost disappear becoming practically independent of dI/dt upon increasing and decreasing of the driving current (Figs. 5.8(d) to 5.8(f)). In particular, in range below about 10 mA, the data on CI and CD branches fall approximately on the same curve. Indeed the applied magnetic field causes a pronounced change in the line shape of the $I - V$ curves of the sample without CH, whereas, the line shape of the $I - V$ curves of sample with CH represented (Fig. 5.4(b)) keeps its non-linear behavior with pronounced hysteresis effects.

Figures 5.9(a) to 5.9(c) show the $I - V$ curves of the BSCCO sample without CH measured for different dI/dt values, and at $T = 102$ K, $H = 0$, $I_{\max} = 30$ mA. To better compare the $I - V$ curves of the samples with and without CH, the same full current scale ($I_{\max} = 30$ mA) (see Fig. 5.6) is used to obtain the $I - V$ curves of BSCCO sample without CH. A comparison of the $I - V$ curves presented in Figs. 5.9(a) to 5.9(c) with those in Fig. 5.6 also shows that the presence of CH in the BSCCO sample enhances the hysteresis effects in the $I - V$ curves and rises the measured dissipation in both CD and CI branches.

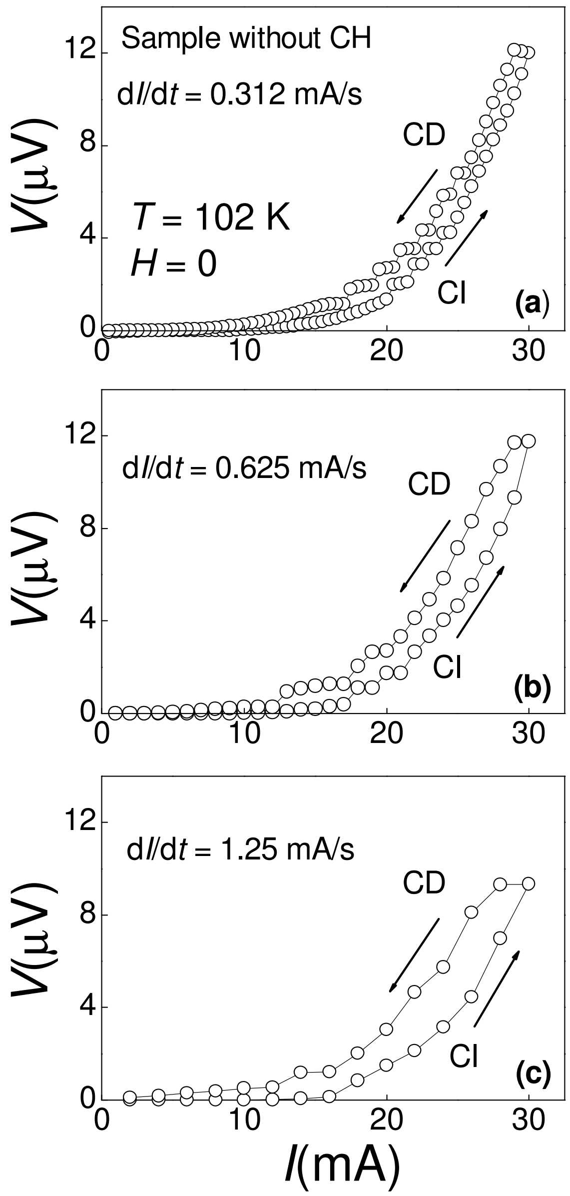

Figure 5.9 The I – V curves of the BSCCO sample without CH for different values of dI/dt = 0.312 **(a)**, 0.625 **(b)**, 1.25 mA/s **(c)** at T = 102 K and H = 0. The maximum current I_{max} = 30 mA.

5.4 The *I* – *V* curves of the sample with CH measured in the reverse procedure

The experimental I – V data presented above were accumulated by using the standard procedure. However, a reverse cycling procedure [35] in which the current is first decreased from I_{max} to 0 (the reverse current decrease (RCD)), and then, the current is increased from 0 to I_{max} (the reverse current increase (RCI)) can be applied as well. Figures 5.10(a) to 5.10(d) show the results of experiments performed using the reverse cycling procedure for sample with CH. The other experimental conditions were the same as those in Figs. 5.4(a) and 5.4(b). The measurements were carried out at T = 102 K, under two different field values of H = 0 and H = 8 mT. The open symbols correspond to the data taken at H = 0, while, the solid symbols to the data obtained at H = 8 mT. I_{c1} and I_{c2} marked on the I – V curves represent the critical currents associated with the RCD and RCI branches, respectively, where the measured voltage is higher than 1 μV. The effect of the reverse procedure on the I – V curves is significant in the sense that the shape of the I – V curves changed markedly as compared to those obtained by using of standard procedure (see Figs. 5.4(a) and 5.4(b)).

The I – V curve measured at H = 0 (open circles in Figs. 5.10(b) to (d)) shows that, initially, the measured voltage on the RCD curve is zero, then, the dissipation increases as the transport current decreases. The voltage tends to pass through a maximum and decreases at lower current. This behaviour becomes more evident as the current sweep rate is decreased from 1.25 to 0.156 mA/s. It is evident in Fig. 5.10(a) that, due to the high dI/dt; the measured voltage on the RCD is zero for currents between 0 and 20 mA. Furthermore, the behavior of the RCI curve is quite different from the RCD curve (Fig. 5.10(a)). On the RCI curve, there is no detectable dissipation up to 14 mA. Then, dissipation increases non-linearly and takes a value of ~15 μV at I_{max} = 20 mA. For the current sweep rate of 1.25 mA/s, the hysteresis between the RCD and RCI branches is less marked. However, as

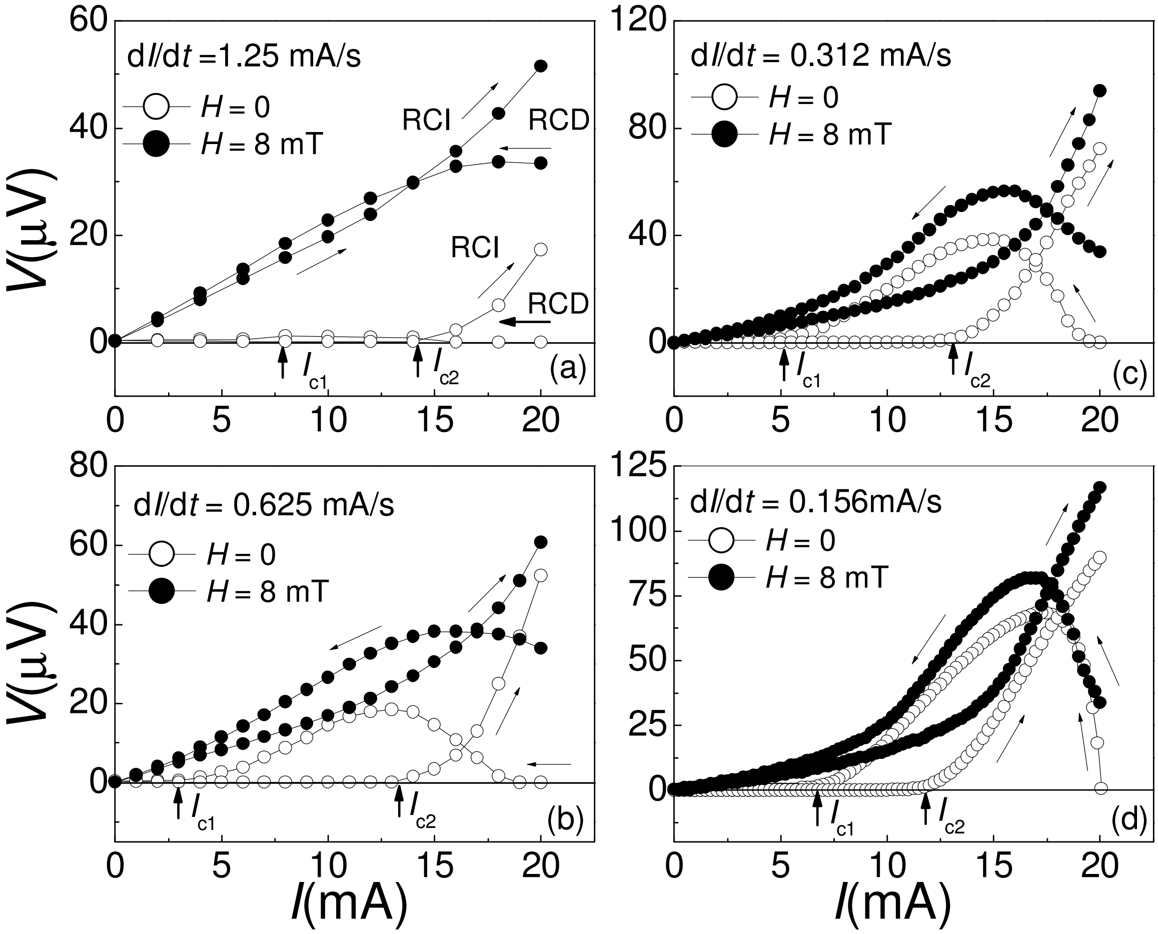

Figure 5.10 The $I - V$ curves of the BSCCO sample with CH measured at $T = 102$ K and $H = 0$ and 8 mT by the reverse procedure for various current sweep rates (dI/dt) from 1.25 to 0.156 mA/s. The arrows show the direction of sweeping of the applied current.

the current sweep rate is decreased, the zero-field $I - V$ curves changes markedly, so that both the dissipation and hysteresis effects are enhanced considerably. A detectable voltage is observed below ~18 mA on the RCD branch of $I - V$ curve for dI/dt = 0.625 mA/s (Fig. 5.10(b)). As the current decreases, the sample voltage first begins to increase, then passes through a maximum (about 15 μV) at ~13 mA; finally, the measured voltage dissipation becomes zero at ~2 mA. However, the first detectable voltage is observed at ~13 mA on the RCI branch of $I - V$

curve in Fig. 5.10(b). In addition, at I_{max} = 20 mA, the measured voltage on the RCI branch takes a value of ~53 μV. This voltage dissipation is higher (by factor of about 3) than that of obtained from the data at dI/dt = 1.25 mA/s. Similar features are also observed for the $I - V$ curves measured at dI/dt = 0.312 and 0.156 mA/s (Figs. 5.10(c) and 5.10(d)). As the current sweep rate decreases, the location of the maximum voltage on the RCD branch shifts to higher currents.

The $I - V$ curves in Figs. 5.10(a) to 5.10(d) demonstrate clearly that the reverse procedure led to a response which has a maximum voltage (V_{max}) in the RCD branch of $I - V$ curves which depend on the value of dI/dt at the beginning of the process. Figure 5.11(a) shows the variation of V_{max} with dI/dt as deduced from the $I - V$ curves measured at H = 0 of the sample with CH (Fig. 5.10). As dI/dt is decreased, the V_{max} value increases markedly. Also, V_{max} values shift to higher current values (see Fig. 5.10). The critical currents I_{c1} and I_{c2} associated with RCD and RCI branches, respectively, as obtained from the $I - V$ data in Figs. 5.10(a) – 5.10(d) by using the 1 μV criterion are plotted as a function of dI/dt in Fig. 5.11(b). In addition, it is observed from Figs. 5.10(b) – 5.10(d) that the I_{c1} values corresponding to the RCD branch shift to low currents as dI/dt is increased, except the one for dI/dt = 1.25 mA/s. However, the RCI branches of $I - V$ curves in Figs. 5.10(a) – 5.10(d) reveal that I_{c2} values (or I_c values associated with RCI branches in Fig. 5.11(b)) tend to increase with increasing dI/dt.

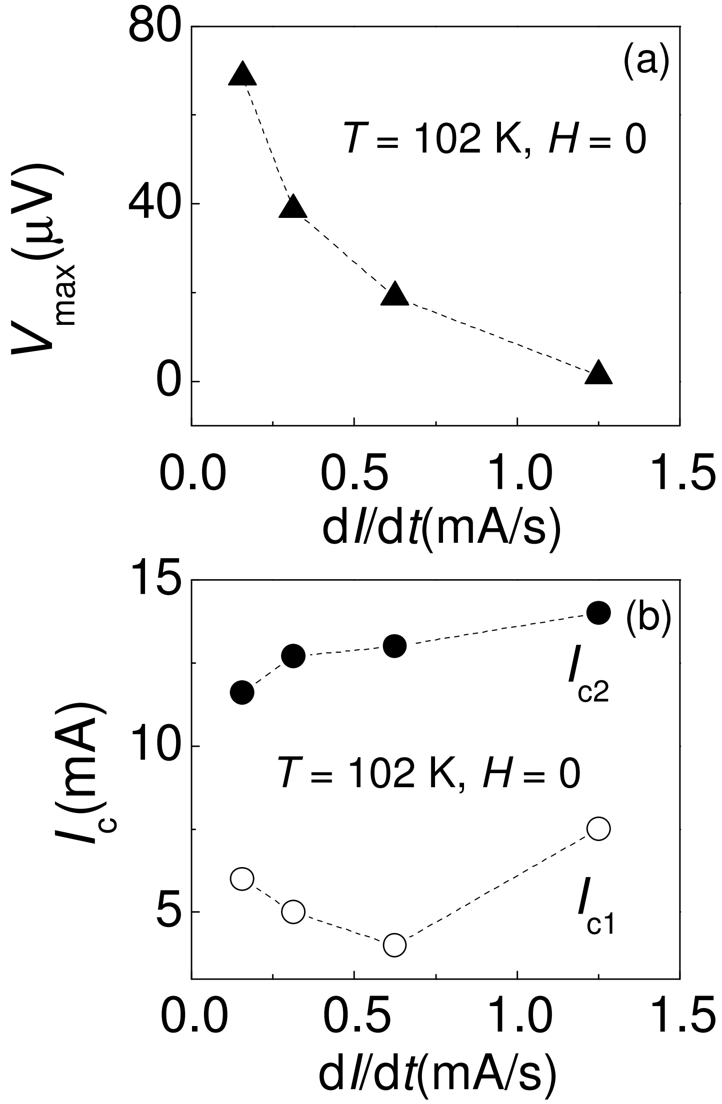

Figure 5.11 (a) The variation of V_{max} as a function of dI/dt as determined from the I – V curves measured at zero magnetic field and T = 102 K. **(b)** The variations of I_{c1} and I_{c2} as a function of dI/dt at zero magnetic field and T = 102 K.

Application of an external magnetic field causes a pronounced change in the I – V curves as compared to those measured at zero magnetic field (Fig. 5.10). When H = 8 mT is applied to the sample, at I_{max} = 20 mA, a voltage dissipation on the RCD curve starts from a certain voltage value (about 34 μV) which is approximately the same for all current sweep rates. Decreasing dI/dt results in an increase in the measured dissipation, which becomes more significant at high currents, and also in an enhancement in the hysteresis effects. However, the RCD and RCI branches corresponding to the $I - V$ curve measured at H = 8 mT for dI/dt = 1.25 mA/s fall approximately on the same curve below 15 mA with negligibly small hysteresis. In order to provide a quantitative measure of the hysteresis effects in the $I - V$ curves measured at H = 0 mT, the width of hysteresis ($\Delta V = V_{RCD} - V_{RCI}$) for two different fixed current values of I = 10 mA and I = 15 mA are obtained from the $I - V$ curves in Fig. 5.10. Figure 5.12 shows the variation of ΔV values with dI/dt. The hysteresis width increases with decreasing of dI/dt.

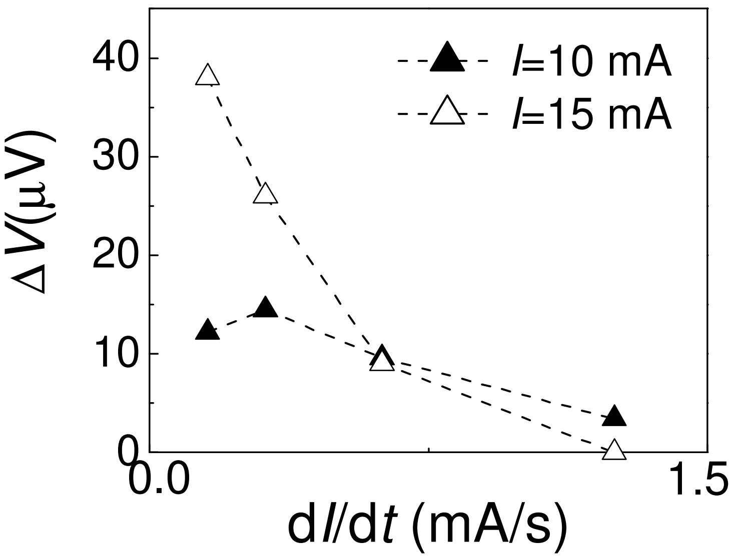

Figure 5.12 The width of hysteresis ΔV for two current values of 10 and 15 mA obtained from the $I - V$ curves given in Figs. 5.10(a) – 5.10(d) at H = 0 as a function of dI/dt.

As mentioned above, in the presence of an external magnetic field, the sample with CH remains in a resistive (normal) state, regardless of the value of dI/dt (see Figs. 5.4(b), 5.7 and 5.10). We also note that, as dI/dt is decreased, a distinct regime appears which manifest itself as a sharp change in slope of the RCI branch above about 15 mA (see Figs. 5.10(c) and 5.10(d)). Initially, a slow increase in dissipation is observed with increasing the current, and, then, a pronounced increase in the rate of dissipation evolves at high currents.

5.5 The effect of maximum current (I_{max}) on the I – V curves measured in the reverse procedure

In order to study the effects of maximum current (I_{max}) on the I – V curve, I – V measurements were made by increasing I_{max} from 20 to 30 mA. The results of the measurements for the sample with CH carried out at T = 102 K and I_{max} = 30 mA under H = 0 (open symbols) and H = 4 mT (solid symbols) are presented in Figs. 5.13(a) and 5.13(b). The I – V curves given in Figs. 5.13(c) and 5.13(d) correspond to the sample without CH. Thus, it becomes possible to evaluate the effect of the CH on transport measurements. The I_c values marked on the I – V curves represent the critical currents associated with the RCI branches.

The voltage dissipation on the RCD branch of I – V curves measured at H = 0 for the sample with CH starts from zero; whereas, for the sample without CH, a dissipation of about 4 μV appears at I_{max} = 30 mA. In addition, the hysteresis in Figs. 5.13(a) and 5.13(b) is more pronounced as compared to that in Figs. 5.13(c) and 5.13(d). It is evident from Fig. 5.13 that the line shape of the I – V curves obtained in the reverse procedure is similar to that observed for the maximum current I_{max} = 20 mA (Fig. 5.10) but quite different from those of the I – V curves measured with the standard procedure (Figs. 5.4,. 5.6 - 5.9).

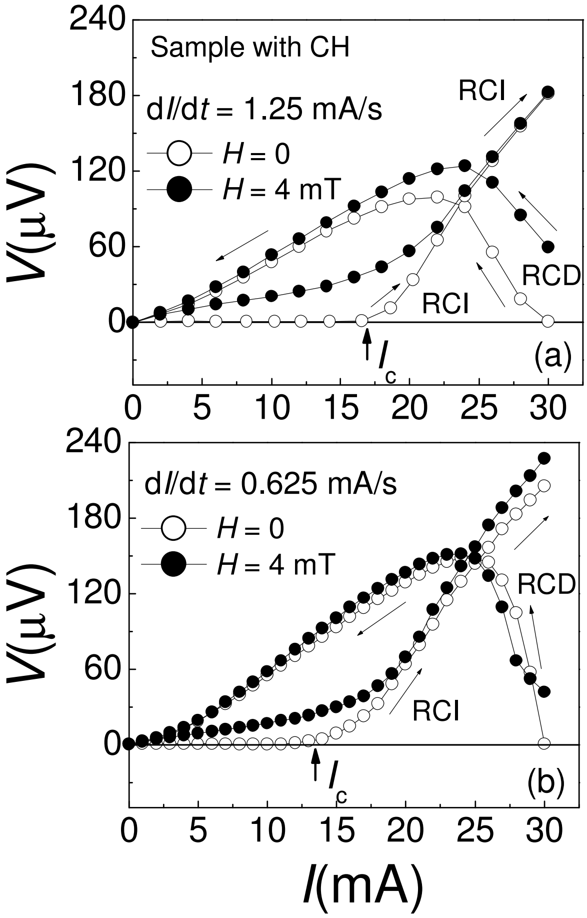

Figure 5.13 The I – V curves of the BSCCO sample with CH measured in the reverse procedure at T = 102 K, H = 0 and H = 4 mT for **(a)** dI/dt = 1.25 and **(b)** dI/dt = 0.625 mA/s. The I – V curves of the sample without CH measured in the reverse procedure at T = 102 K and H = 0 for **(c)** dI/dt = 1.25 and **(d)** dI/dt = 0.625 mA/s. The maximum current I_{max} = 30 mA. The arrows show the direction of sweeping of the applied current.

To further investigate the effects of I_{max} on the I – V curves, I – V measurements were carried out for the samples with and without CH taking I_{max} = 40 mA. Figures 5.14(a) to 5.14(f) show the I – V curves of the samples with and without CH measured at 102 K for zero field (H = 0) for dI/dt = 1.25, 0.625, and 0.312 mA/s. When I_{max} = 40 mA is applied to the sample, a voltage of about 203 μV, which is independent of the value of dI/dt, develops for all I – V curves of the sample with CH (Figs. 5.14(a) to 5.14(c)). The hysteresis effects tend to increase

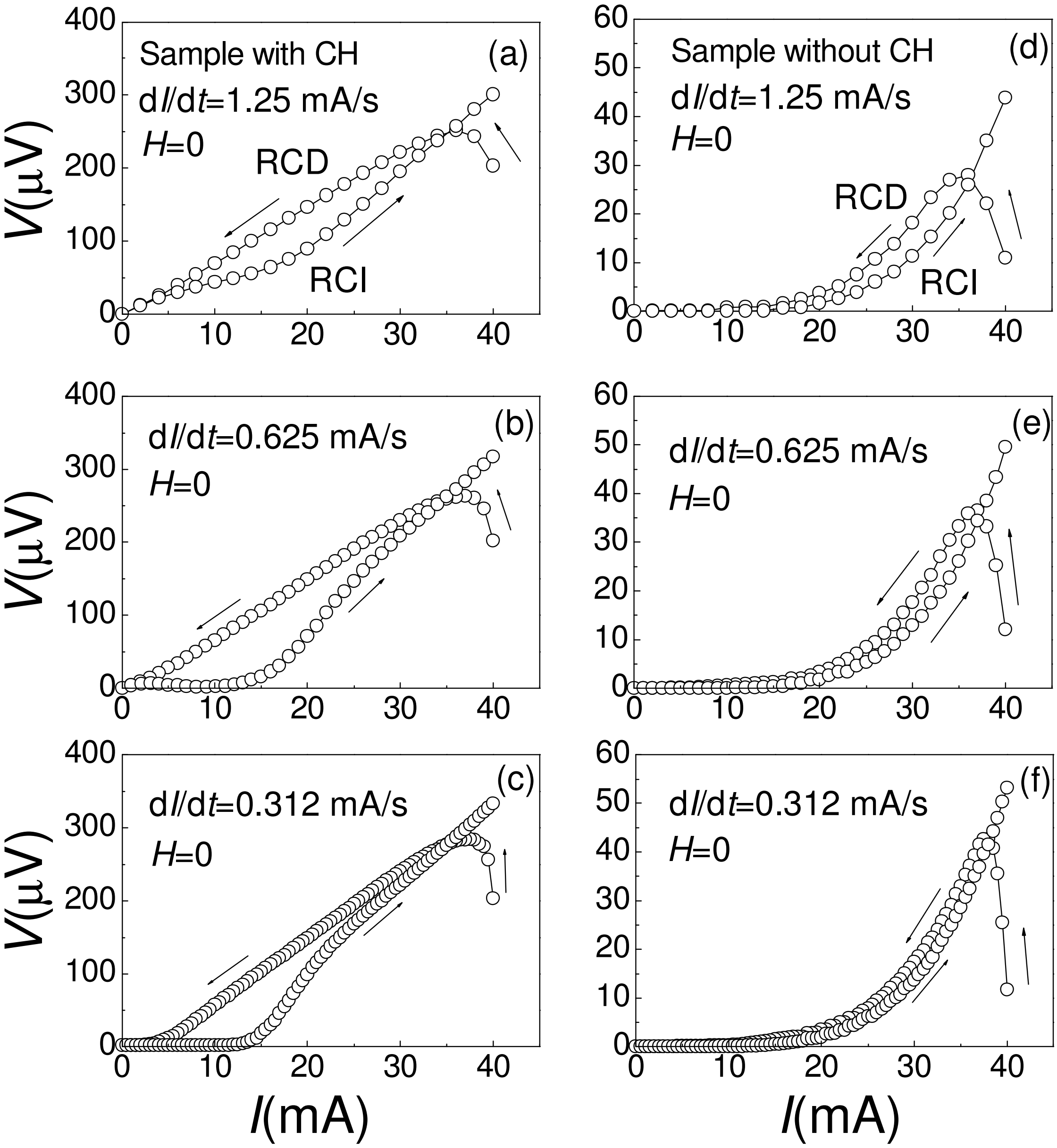

Figure 5.14 The I – V curves of the BSCCO sample with CH measured in the reverse procedure at **(a)** dI/dt = 1.25, **(b)** dI/dt = 0.625 and, **(c)** dI/dt = 0.312 mA/s. The I – V curves of the sample without CH measured in the reverse procedure at **(d)** dI/dt = 1.25 **(e)** dI/dt = 0.625 and **(f)** dI/dt = 0.312 mA/s. All measurements were made at T = 102 K and H = 0. The maximum current I_{max} = 40 mA. The arrows show the direction of sweeping of the applied current.

with decreasing dI/dt. The measured dissipation corresponding to the RCD branch increases gradually and passes through a maximum which shifts to higher currents with decreasing dI/dt. In addition, the RCD branch reveals that sample with CH remains mostly in a resistive state on the whole current range of the experiment. This finding implies the presence of a more correlated motion of the vortices.

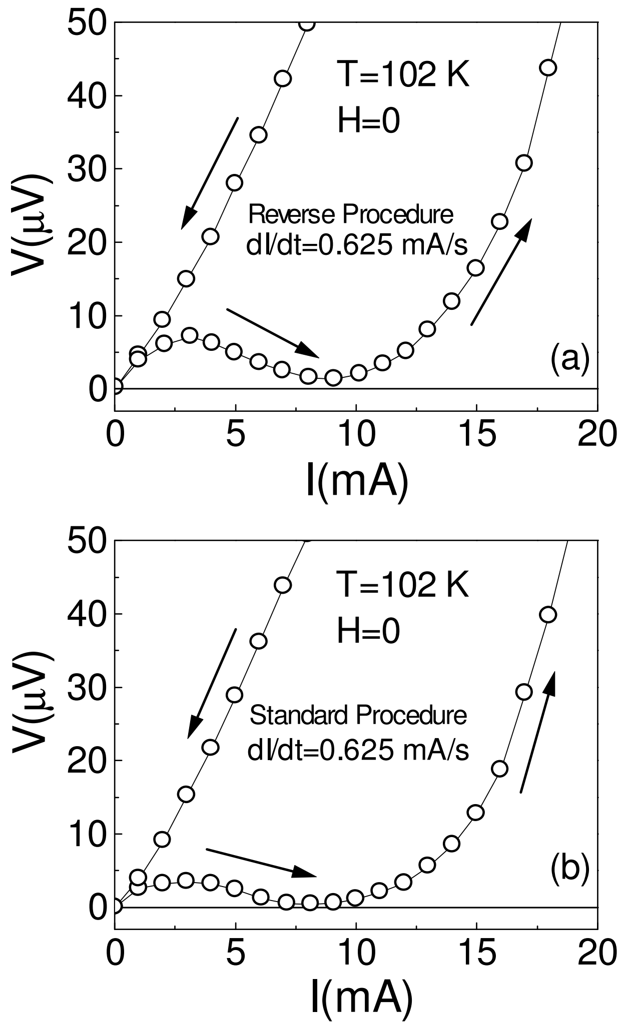

Figure 5.15 The I – V curves of sample with CH measured in **(a)** the reverse procedure and **(b)** the standard procedure. The experimental conditions are the same as in Fig. 5.14(a). Note that a downward curvature is observed on the RCI branch at low currents in both procedures in the expanded scale.

The I – V curves of the sample without CH measured in the reverse procedure are presented in Figs. 5.14(d) – 5.14(f). The hysteresis decreases with decreasing dI/dt, and the line shape of the I – V curves are not influenced much by the variation of dI/dt. Further, a voltage (~ 12 μV) which is lower than that of the sample with CH appears when I_{max} = 40 mA is applied, and this voltage becomes essentially independent of dI/dt. We also note that the measured dissipation for the RCD and RCI branches increases somewhat with decreasing dI/dt, in particular, at high currents. A comparison between the I – V curves of samples with and without CH reveals once again that the reverse procedure causes different responses.

On the other hand, the RCI branch of the I – V curve for the sample with CH measured at dI/dt = 1.25 mA/s exhibits a downward curvature below about 15 mA (see Fig. 5.14(a)). Furthermore, a trace of downward curvature in I – V curve for dI/dt = 0.625 mA/s (Fig. 5.14(b)) is also seen below about 10 mA. The I – V curves in Fig. 5.14(b) are plotted in an expanded scale (Fig. 5.15(a)) for a better demonstration of downward curvature.

When the current is increased with a rate of 0.625 mA/s, the measured voltage dissipation first increases, and, then, tends to decrease nonlinearly by taking very low values at about 8 mA. However, higher current causes again an increase in the measured dissipation and it shows a re-entrance. Fig. 5.15(b) presents the I – V curves measured under the same experimental conditions as in Fig. 5.15(a) by using the standard procedure. We observe a similar but less pronounced behavior than that in Fig. 5.15(a). We could not observe downward curvature in I – V curves of BSCCO sample without CH in the current and dI/dt ranges used as for

BSCCO sample with CH (see Fig. 5.14(e)). We suggest that the downward curvature in the $I - V$ curves at low currents may be associated from the presence of cylindrical hole.

5.6 Transport relaxation measurements

The experimental results presented in Sections 5.1 to 5.5 show that varying the value of dI/dt influences directly the $I - V$ curves, which can be attributed to the relaxation effects. Another powerful method to investigate the time effects on the evolution of sample voltage is to measure the voltage-time ($V - t$) curves [32, 84]. Two methods are used here to measure the $V - t$ curves. One is to apply a constant current, and the other is to apply a symmetric bidirectional square (BSW) wave current to the sample. After the current is applied to the sample, we start to measure the voltage developing across the sample as a function of time. Thus, it becomes possible to monitor all details of the time evolution of the sample voltage, including the transient effects. In some experiments, the dc current was interrupted or reduced to a finite value, in order to create a quenched state which is defined as an abrupt decrease in the transport current.

5.6.1 Time evolution of the sample voltage: $V - t$ curves

Such measurements involve recording the time evolution of the sample voltage at constant current and external magnetic field at temperatures below T_c. Slow and fast transport relaxation measurements of the $V - t$ curves provide a useful tool to investigate the details of the time effects in superconducting samples at temperatures just below T_c [3, 4, 28, 30, 35, 44, 84].

At slow current sweep rates, the flux lines (or the current-induced self magnetic flux lines) can find enough time to re-organize themselves. However, fast current sweep rates can be used to probe the long- or short-lived metastable states by taking directly a snapshot of the instantaneous flux line configuration before the system re-organizes itself. Therefore, such measurements are important in many transport studies and underline the importance of the time response (measurement speed) of the experimental set-up.

In this study, $V - t$ curves corresponding to the slow transport relaxation regime are obtained by applying a dc driving initial current I_1 (for a period of 60 s). The voltage developing in the direction of the transport current is measured as a function of time. During the time evolution of the sample voltage (or after the steady state is reached), the initial current I_1 is either reduced to a lower value I_2 or interrupted completely. Then, the value of I_2 is fixed in the rest of the relaxation process, i.e., up to 120 s. Thus, it becomes possible to create a quenched state. Such experiments provide a method to examine the time evolution of the quenched state and the details of current dependent re-organization of flux lines [84].

Figure 5.16 shows a set of typical $V - t$ curves for the BSCCO sample with CH measured for I_1 = 20 mA and different values of I_2 from 0 to 18 mA at T = 102 K and H = 0. The sample voltage initially increases nonlinearly and and tends to

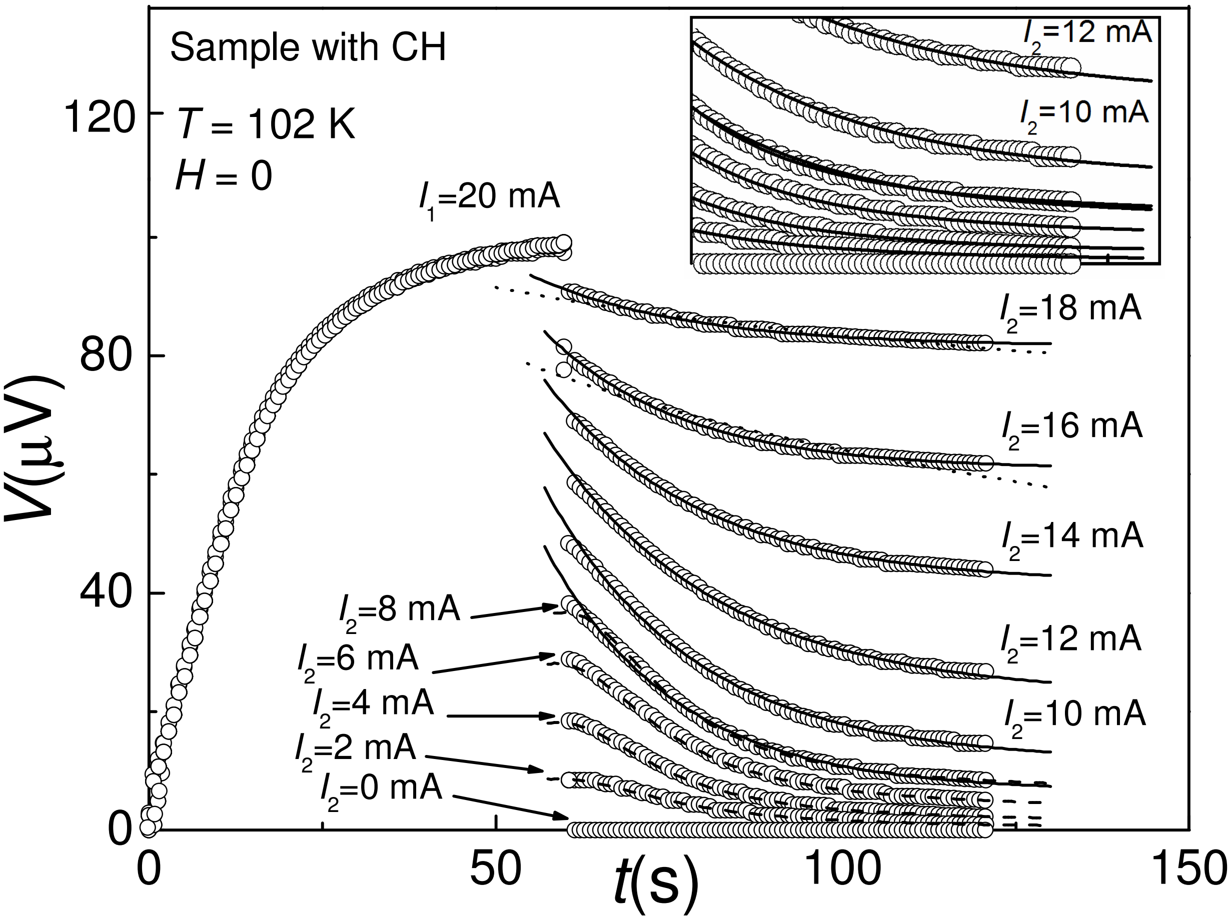

Figure 5.16 The $V - t$ curves for the BSCCO sample with CH measured at T = 102 K and H = 0 with I_1 = 20 mA and different values of I_2 as shown. The solid lines represent the calculated curves defined by Eq. (3.1). Dashed lines are calculated by using $V(t) \sim 1/1+(t/t_0)^2$ modified from Eq. (3.9), and dotted lines are described in Eq. (3.5). The inset shows the step behaviour in the sample voltage in an expanded scale.

level off as the time evolves. When I_1 = 20 mA, the sample voltage measured at t = 60 s is nearly equal to that in the $I - V$ curves for dI/dt = 0.156 mA/s (see Fig. 5.4(a)). The time evolution of sample voltage can be attributed to the reorganization of the transport current along the sample.

When the initial current I_1 is reduced abruptly to a certain value I_2, following a discontinuous sharp drop, the sample voltage associated with quenched state [103] decreases smoothly with time (Fig. 5.16). Here, it should be noted that the smooth decrease in the sample voltage evolves in the form of steps during the relaxation process (see also the inset in Fig. 5.16). The step behavior can be related to the decrease in the number of flux lines accumulated in the CH. As I_2 is decreased below about 8 mA a voltage hump appears at the beginning of the time evolution of quenched state. Note that, when $I_2 = 0$, the sample voltage drops abruptly to zero without any relaxation. This indicates that no residual voltage is left on the sample to be relaxed within the time response of the experimental set-up [103].

The $V - t$ measurements were also carried out for the BSCCO sample without CH at $T = 102$ K and $H = 0$. The aim was to compare the results with those obtained for the BSCCO sample with CH. Figure 5.17 shows a set of $V - t$ curves measured at $T = 102$ K and $H = 0$ with $I_1 = 40$ mA and $I_2 = 0$, 15, 20, 25, 30, and 35 mA. Here, the initial current I_1 is taken to be 40 mA, because the voltage dissipation measured with $I = 20$ mA is very small (around 3 μV) (see the Figure 5.8(a)). Even with $I_1 = 40$ mA, the voltage dissipation is still lower than that of the sample with CH. The sample voltage initially increases non-linearly and tends to level off at about 60 μV (Fig. 5.17). After reducing I_1 to I_2, voltage drop of sample without CH is not sharp as that of the sample with CH. Instead, it decays smoothly but faster at early times of the relaxation process.

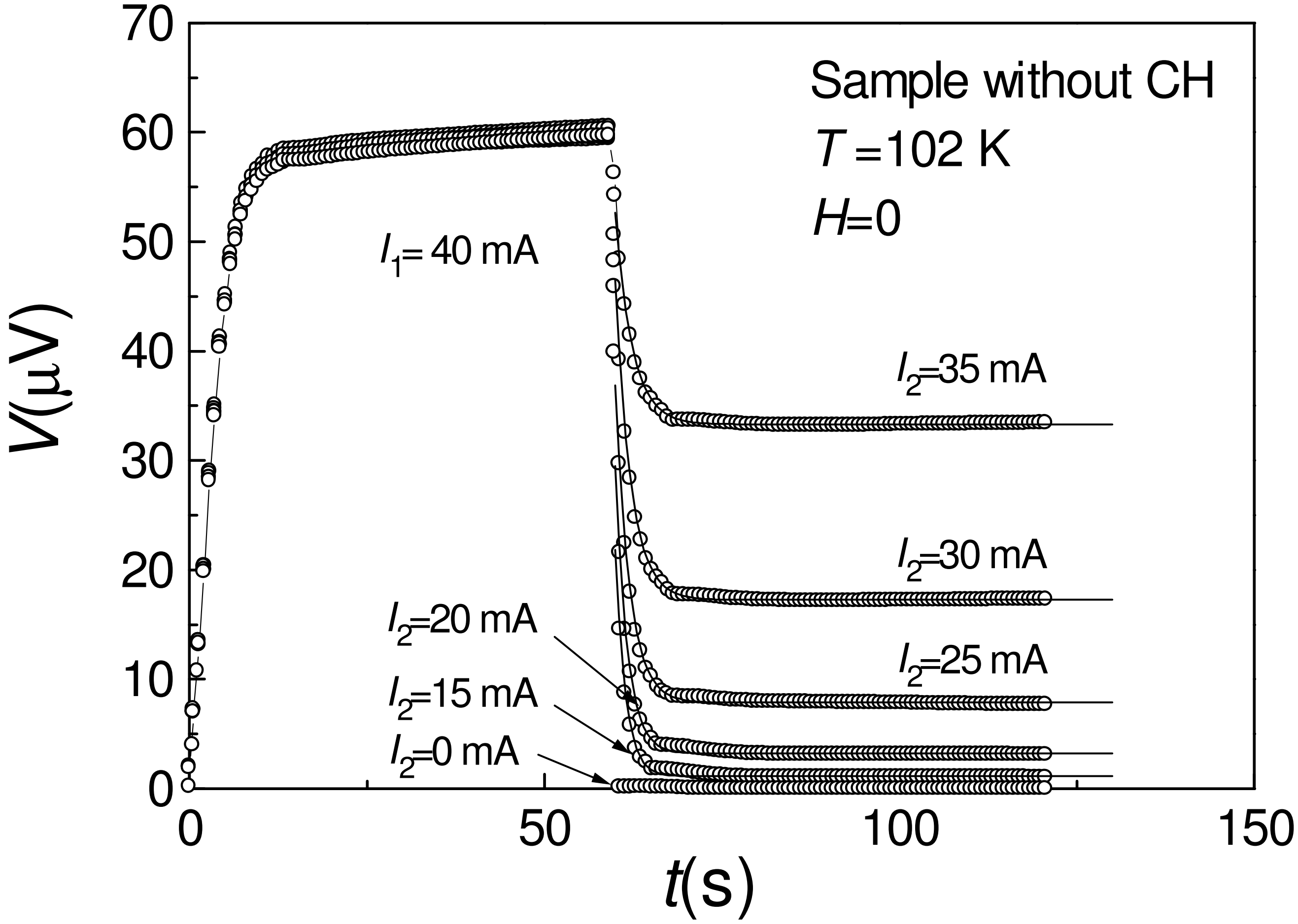

Figure 5.17 The $V-t$ curves for the BSCCO sample without CH measured at T = 102 K and H = 0 with I_1 = 40 mA and different values of I_2. The solid lines are calculated using Eq. (3.1).

To further compare the time effects on sample voltages, the $V-t$ curves of the samples with and without CH were differentiated with respect to time (Fig. 5.18). The dV/dt versus t curve for the sample without CH exhibits a narrow sharp peak at the early stage of the relaxation process and reaches higher value when compared to that of the sample with CH. This peak corresponds to the fast initial increase in sample voltage when the initial current I_1 is applied (see the inset in Fig. 5.18). Following the peak at $t \cong 2$ s the dV/dt of the sample without CH decreases rapidly to zero at $t \cong 14$ s. However, the dV/dt for the sample with CH

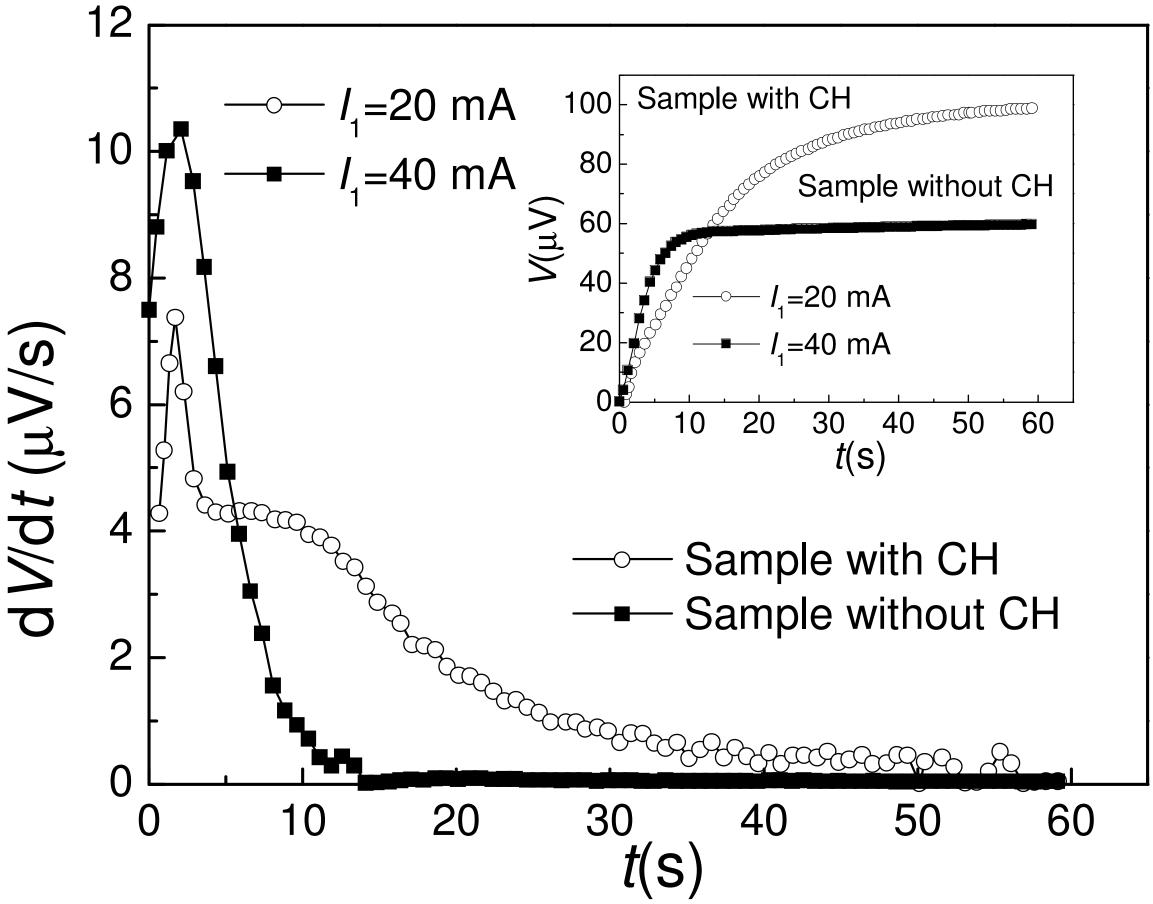

Figure 5.18 The dissipation rates (dV/dt) for the BSCCO samples with and without CH as calculated from the corresponding $V - t$ curves given in the inset.

never becomes zero in the time interval 0 – 60 s. The difference in the dV/dt – t curves of samples with and without CH can be attributed to the presence of CH in the former sample which is expected to accumulate trapped flux lines. Such a flux trapped inside the CH may result in an extra voltage dissipation during the relaxation process.

The influence of external magnetic field on the V - t curves can be seen in Figures 5.19 and 5.20 which were measured at much lower temperature, because the dissipation under magnetic field becomes very high. Fig. 5.19 shows the $V - t$

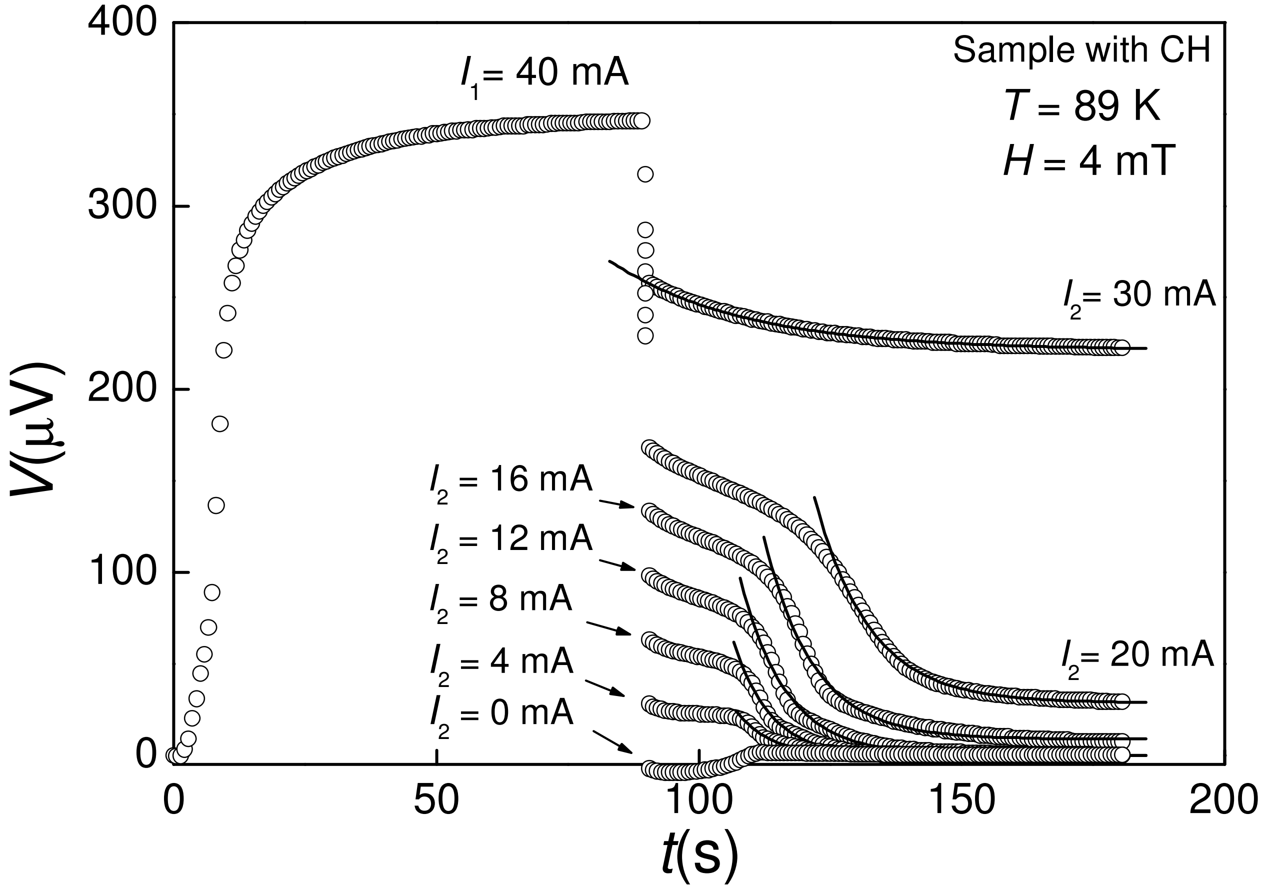

Figure 5.19 The $V - t$ curves of the BSCCO sample with CH measured at $T = 89$ K and $H = 4$ mT with $I_1 = 40$ mA for selected values of I_2. The solid lines are calculated using Eq. (3.1).

curves of the BSCCO sample with CH measured at $T = 89$ K and $H = 4$ mT with $I_1 = 40$ mA for selected values of $I_2 = 0$, 4, 8, 12, 16, 20, and 30 mA. Figure 5.20 presents the $V - t$ curves of the sample without CH measured at $T = 94$ K and $H = 4$ mT with $I_1 = 40$ mA for $I_2 = 0$, 10, 20, and 30 mA. The initial nonlinear increase in the sample voltage within first 25 s (Figs. 5.19 and 5.20) can be attributed to the suppression of superconducting order parameter with the help of the driving current. Reducing the driving current from I_1 to I_2 results in voltage decays in two stages (except for I_2 = 30mA) implying that the superconducting order parameter is suppressed much more as compared to that for the lower I_2 values (Fig. 5.19).

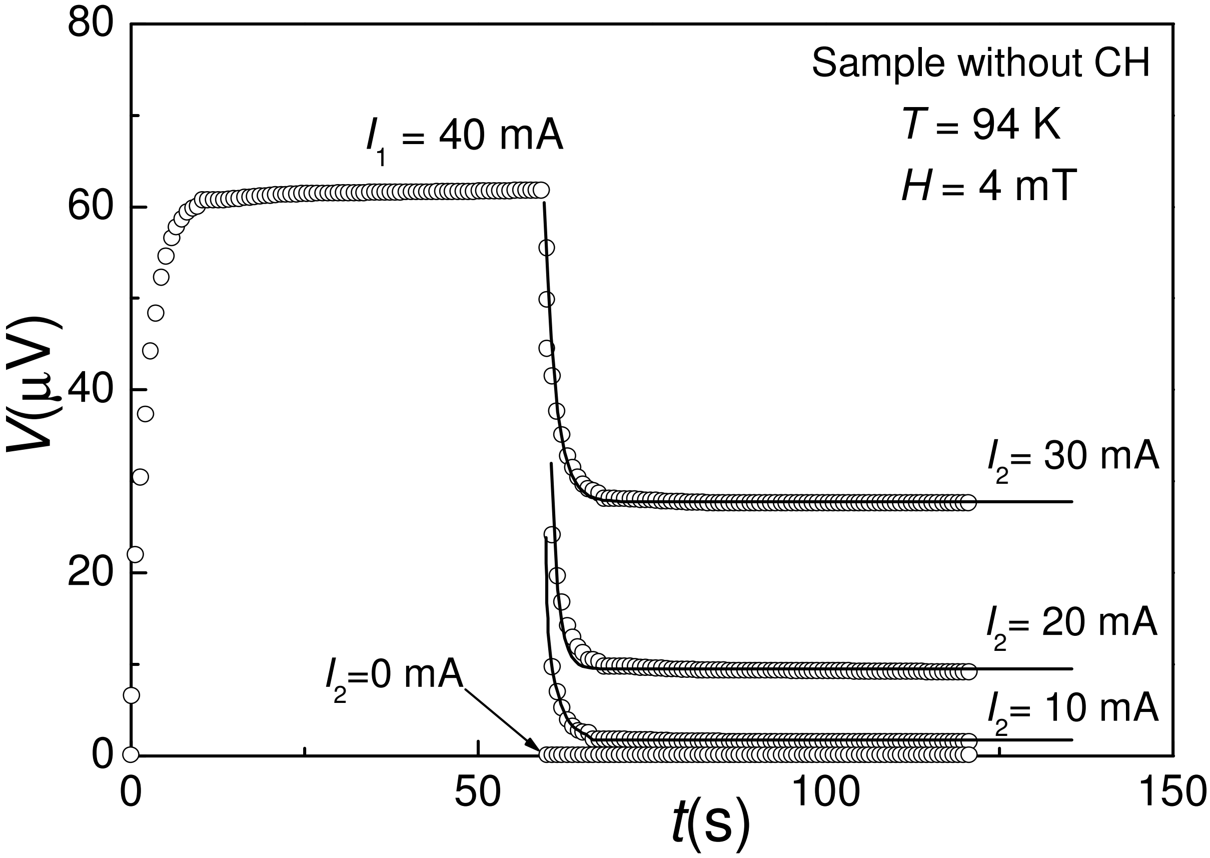

Figure 5.20 The $V - t$ curves of the BSCCO sample without CH measured at T = 94 K and H = 4 mT with I_1 = 40 mA at selected values of I_2. The solid lines are the calculated curves using Eq. (3.1).

Note that a smooth transition to a superconducting state is reached in the $V - t$ curves recorded for I_2 = 4, 8, and 12 mA; whereas, the zero resistance state is not reached for I_2 = 16 and 20 mA. The time evolution of the voltage response of the sample without CH under the magnetic field (Fig. 5.20) is similar with that given in Fig. 5.17.

5.6.2 Current and magnetic field dependent voltage oscillations

In this section, we investigated the influence of an alternating driving current on the voltage response (i.e., the flux dynamics) in the BSCCO samples with and without CH. A symmetric bidirectional square wave (BSW) current with long period (P_I) was applied to the samples. The time evolution of sample voltage was measured for BSW current with different amplitudes and periods, at different magnetic fields and temperatures.

Figures 5.21(a) – 5.21(d) show the voltage response ($V – t$ curves) of the sample with CH to a BSW current of 1 mA amplitude measured at 102 K and zero magnetic field ($H = 0$). The period of the BSW current was in the range from 10 to 30 s. The sample voltage exhibits regular oscillations as a function of time, which reflects the change in the polarity of the driving current. The voltage oscillations are approximately symmetrical with respect to the zero voltage line. The amplitude of the oscillations increases slightly with increasing the period P_I of BSW current. This finding suggests that there are some relaxation effects appearing during the oscillations and, thus, the measured dissipation increases with increasing P_I. This observation also indicates that the period of the driving current has a direct influence on the time evolution of the sample voltage for a fixed amplitude (= 1 mA) of BSW current. The distortions in the line shape of the voltage oscillations for $P_I = 20$ s and 30 s can also be taken as an evidence for the relaxation effects related to high period of the BSW current.

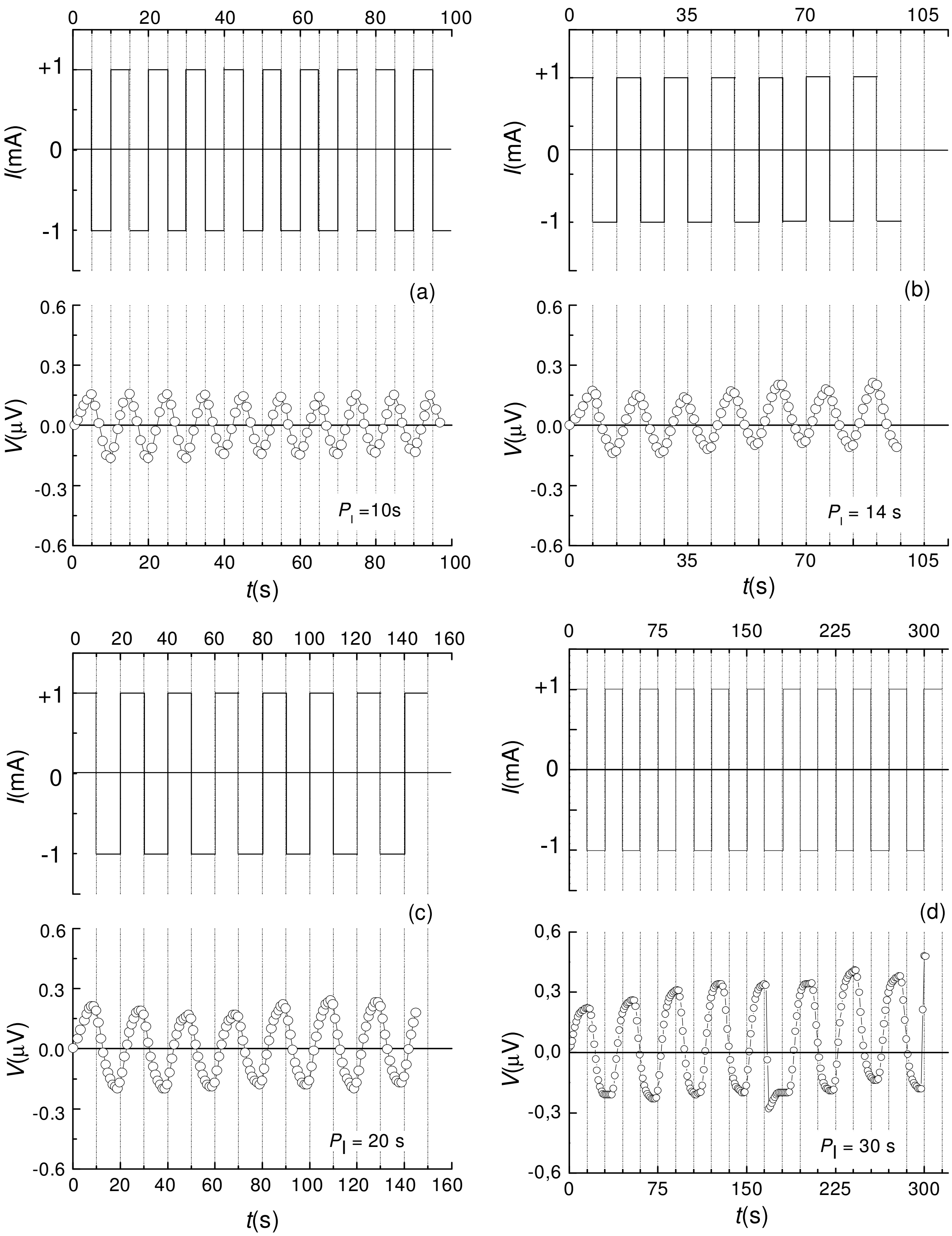

Figure 5.21 The lower panels show the voltage oscillations measured for the BSCCO sample with CH at T = 102 K and H = 0. The upper panels show the bidirectional square wave (BSW) currents with different a period P_{I} **(a)** 10 s, **(b)** 14 s, **(c)** 20 s, **(d)** 30 s. The amplitude of the BSW current was I = 1 mA.

The spectral content of the voltage oscillations were determined by using the Fast Fourier Transform (FFT) technique [44]. The FFT analysis of the $V-t$ curves in Fig. 5.21 reveals that there is a fundamental frequency accompanied by its harmonics (Fig. 5.22). The fundamental periods ($P_{\mathrm{Vosc,FFT}}$) of the voltage response oscillations obtained by FFT analysis are 12.21, 17.15, 25.77, and 38.16 s. The values of $P_{\mathrm{Vosc,FFT}}$ are comparable to the actual periods of the corresponding BSW driving currents (i.e., P_{I} = 10, 14, 20, and 30 s).

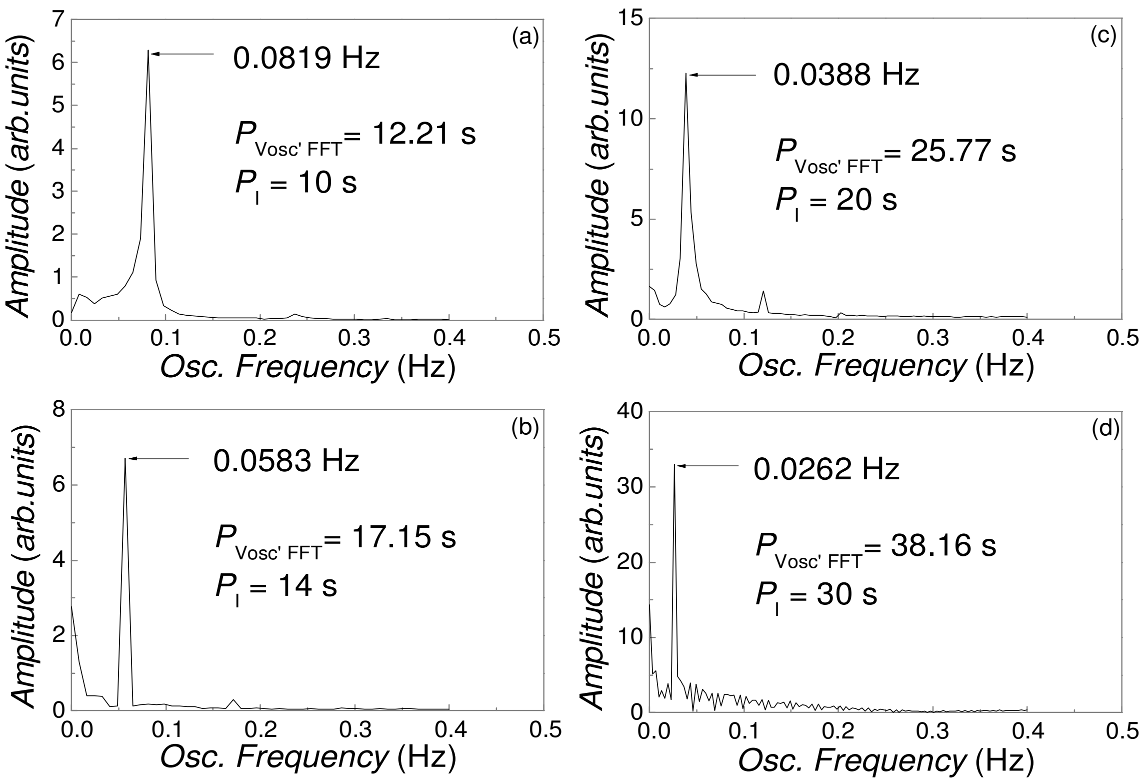

Figure 5.22 Fast Fourier Transform of the $V-t$ curves for the BSCCO sample with CH given in Fig. 5.21(a) to 5.21(d) measured at 102 K for BSW drive with amplitude 1 mA and periods P_I = 10, 14, 20, and 30 s, respectively. The fundamental periods $P_{\mathrm{Vosc,\ FFT}}$ found from FFT of the corresponding $V-t$ curves are 12.21, 17.15, 25.77, and 38.16 s respectively.

In order to determine the influence of the amplitude of BSW current on the time evolution of the sample voltage, $V-t$ measurements were made at $T = 102$ K and $H = 0$ for different amplitudes of 0.5, 1, 1.5, 2 mA of the BSW current with a fixed period $P_I = 10$ s. The $V-t$ curves obtained for the sample with CH are presented in Figures 5.23(a) – 5.23(d). Increase in the amplitude of the BSW current influences the line shape of the voltage response in two ways. The voltage

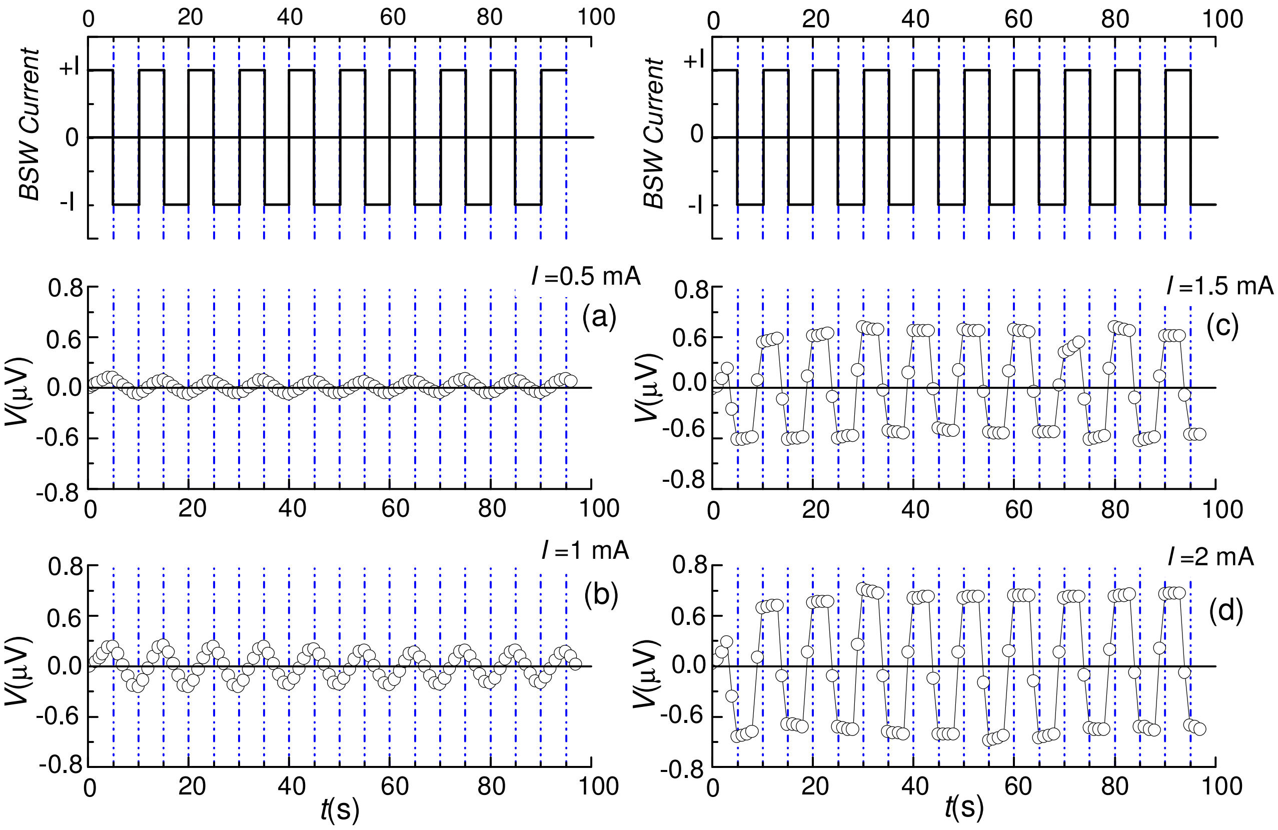

Figure 5.23 Voltage response of the BSCCO sample with CH to BSW current with a period $P_I = 10$ s and with amplitude of **(a)** 0.5 mA, **(b)** 1 mA, **(c)** 1.5 mA, and **(d)** 2 mA. The measurements were made at $T = 102$ K and $H = 0$. The panels on top of each figure show the bidirectional square wave (BSW) currents.

dissipation increases when the amplitude of the BSW current is increased. The $V-t$ curves obtained for BSW current with amplitudes 0.5 and 1 mA (Figs.

5.23(a) and 5.23(b)) exhibit sinusoidal-type voltage oscillations. However, the oscillations in $V - t$ curves evolves to a square-wave or chopped sinusoidal wave form for BSW current with amplitudes of 1.5 and 2 mA (Figures 5.23(c) and 5.23(d).

In the following we demonstrate that sinusoidal-like voltage oscillations can be observed also in the presence of an external magnetic field, provided that the temperature, the amplitude and period of the BSW current are appropriate. The temperature was reduced to 96 K and the measurements were performed at $H = 16$ mT for the fixed amplitude 1 mA but different periods ($P_I = 10$, 14, 20 and 30 s) of the BSW current. As can be seen from the $V - t$ curves of sample with CH (Figs. 5.24(a) – 5.24(d)), the voltage oscillations are of sinusoidal type and nearly symmetric with respect to zero voltage. However, the line shape of the voltage response ($V - t$ curves) changes with increasing the period of the applied BSW current. Change in the polarity of the driving current with low period results in triangular wave-like voltage oscillations (Figures. 5.24(a) and 5.24(b)). However, the peak point of the voltage oscillations becomes more round upon increasing P_I towards 30 s (Fig. 5.24(c) and 5.24(d)). This is because, the voltage response tends to level off (which can be taken as an indicator that the voltage reaches the steady state) during one half period of the applied current of amplitude 1 mA for $P_I = 20$ and 30 s. At the same time, slight increase in the measured dissipation with increasing of P_I is also observed. The results suggest that voltage oscillations appear for driving BSW currents with low period (see Figs. 5.24(a) and 5.24(b)),

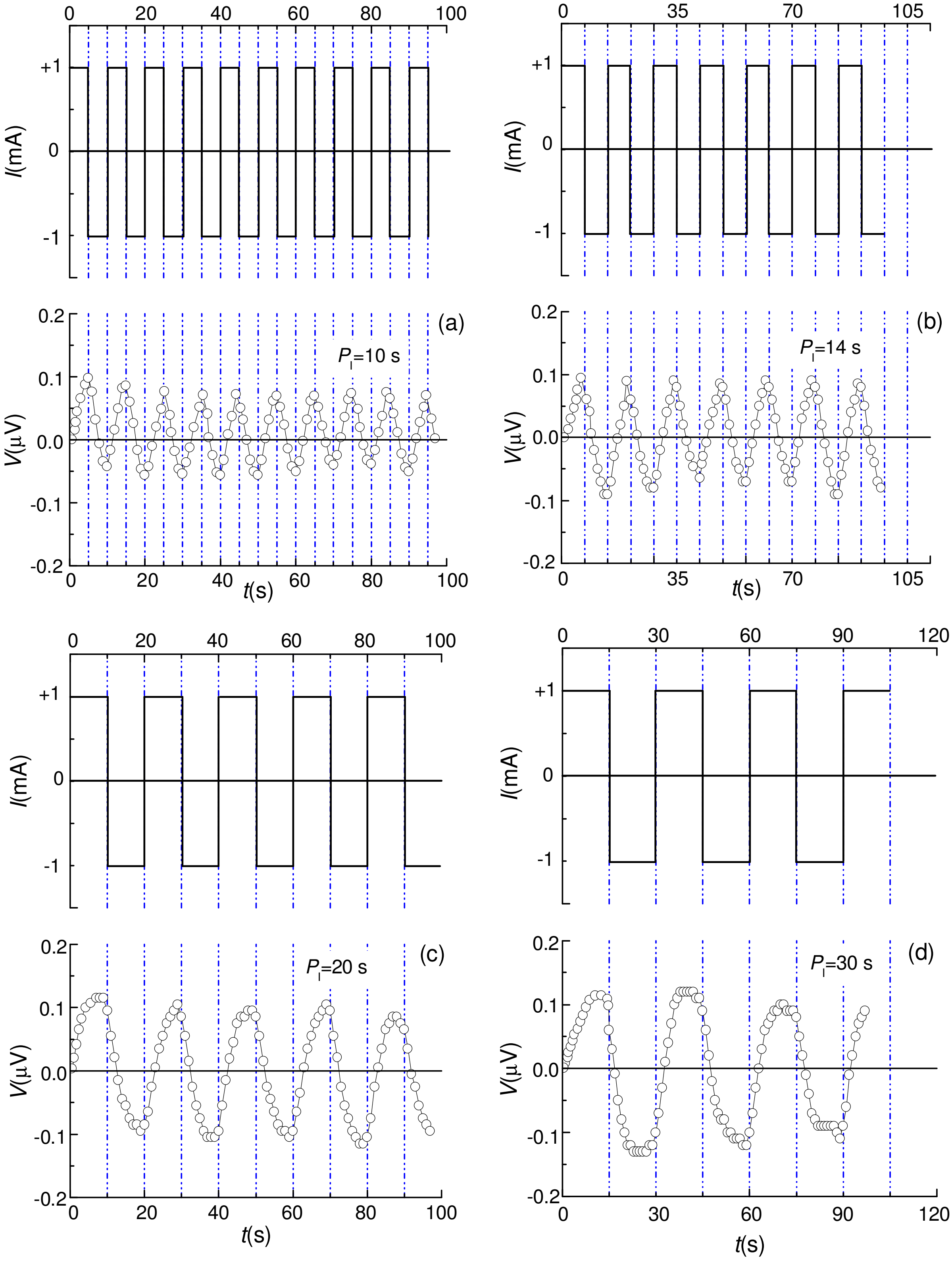

Figure 5.24 Oscillations in the $V-t$ curves for the BSCCO sample with CH measured at $T = 96$ K and $H = 16$ mT for different periods of the BSW current **(a)** $P_I = 10$ s, **(b)** 14 s, **(c)** 20 s, and **(d)** 30 s. The amplitude of BSW current was $I = 1$ mA. The upper panels show the BSW driving current.

and the voltage response should be far from the steady state. This explains why the voltage amplitude decreases with decreasing the period of driving BSW current.

As is shown in Fig. 5.23, the amplitude of the BSW current is another important parameter which affects the shape of the voltage oscillations. In order to provide further support to this suggestion, $V - t$ curves were measured at $T = 96$ K and $H = 0$ for BSW current with different amplitudes of 9.0 and 9.5 mA. The periods of BSW current values were selected as 10 s and 14 s, respectively. The $V - t$ curves of the sample with CH obtained under these experimental conditions are shown in Figure 5.25. The sample voltage initially increases smoothly with time up to ~ 10 s, then decreases with time by tending to reach the superconducting state. Further, the voltage response does not follow the changes in the polarity of the BSW current. The voltage oscillations which are not symmetrical over the whole time range considered were observed especially for $t >\sim 35$ s (see Fig. 5.25(a)). On the other hand, regular voltage oscillations appear in the $V - t$ curves presented in Figures 5.25(b) and 5.25(c) for $t > \sim 25$ s and $t > \sim 28$ s, respectively. A slight increase in the amplitude of the BSW current results in an increase in the amplitude of the voltage response, which now follows the polarity change of BSW current at longer times. Note that, for $t > 70$ s, the voltage oscillations become more symmetrical with respect to zero voltage when compared to those in Fig. 5.25(b), as the period of BSW current with 9.5 mA amplitude is increased from 10 to 14 s.

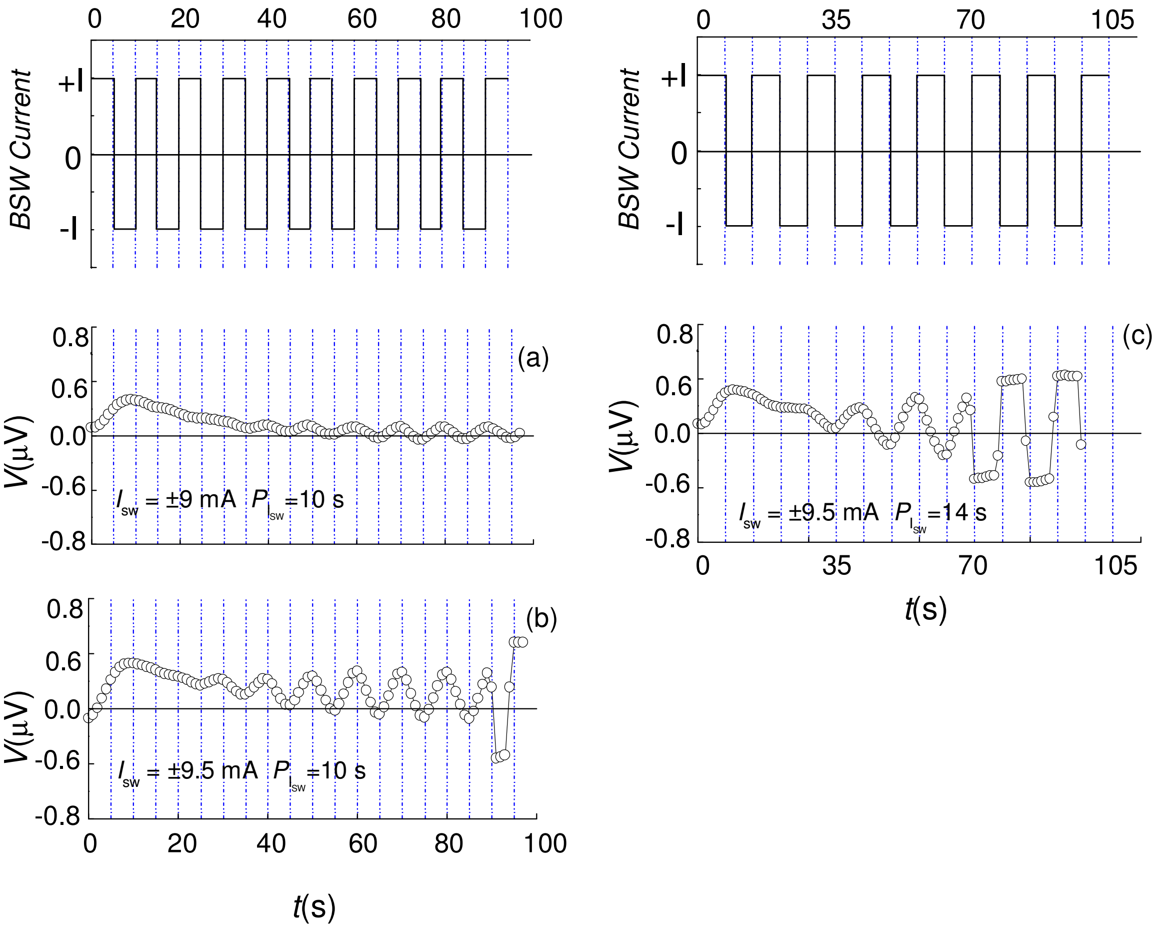

Figure 5.25 The voltage oscillations in the $V - t$ curve of the BSCCO sample with CH measured at T = 96 K and H = 0 for different amplitudes of the BSW current **(a)** I = 9 mA and **(b)** I = 9.5 mA with period P_I = 10 s. **(c)** I = 9.5 mA and P_I = 14 s. The panels on top of each figure show the BSW current.

Also, sinusoidal-like voltage oscillations in the $V - t$ curves are observed above t > ~ 28 s accompanied by a slight increase in the measured dissipation (Fig. 5.25(c)). Furthermore, the amplitude of oscillations gradually increases over time becoming approximately symmetric with respect to zero voltage line and finally, for t > ~ 70 s, its time evolution changes its character from sinusoidal to square wave oscillations. A similar change of behavior is observed for t > ~ 90 s in Fig. 5.25(b).

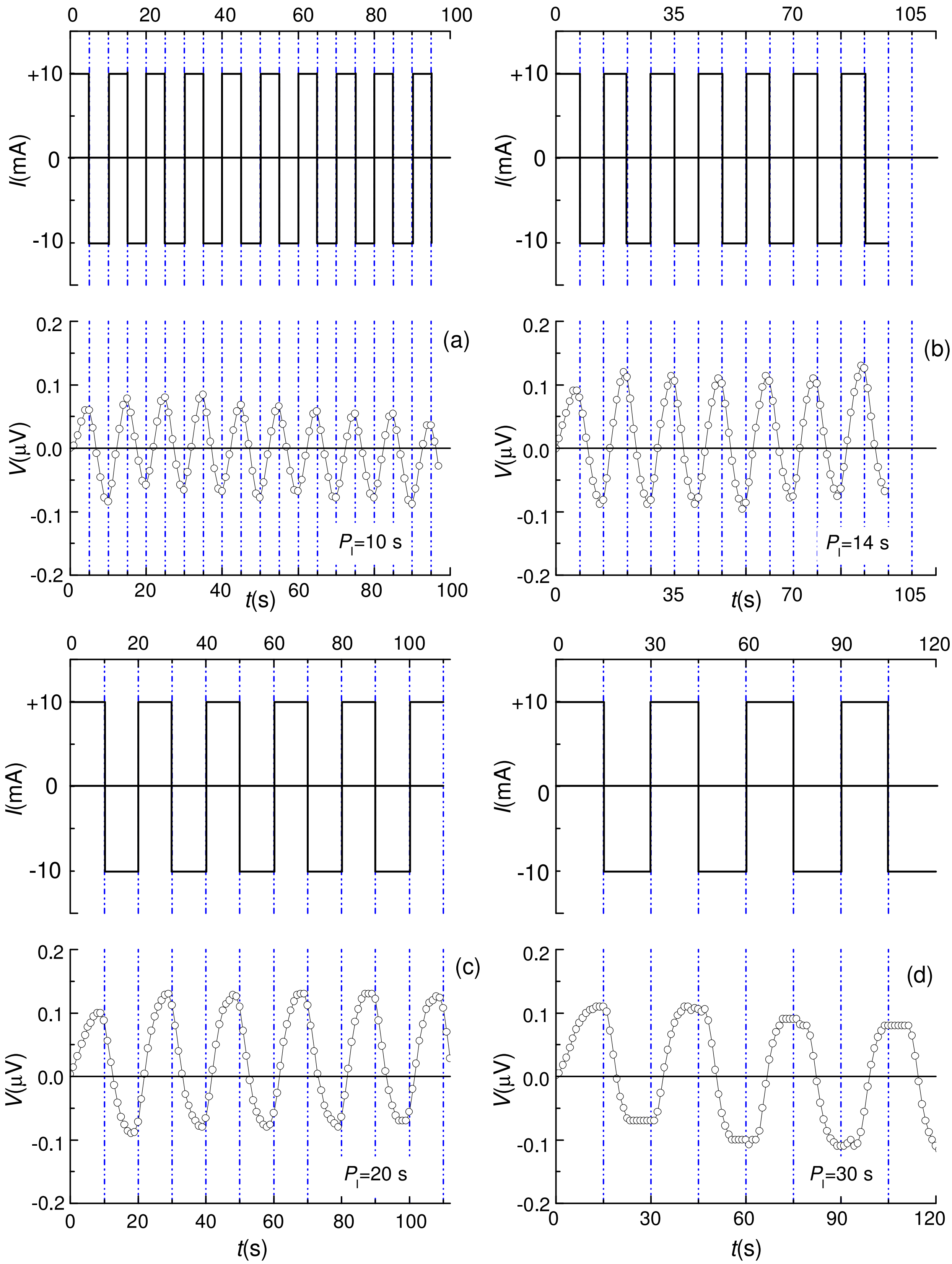

Figure 5.26 The $V-t$ curves of the BSCCO sample without CH measured at $T = 102$ K and $H = 0$ for BSW current wth period P_I **(a)** 10 s, **(b)** 14 s, **(c)** 20 s, **(d)** 30 s. The amplitude of BSW current was $I = 10$ mA. The upper panels show the BSW current.

Similar voltage oscillations were also observed in the $V-t$ curves for the sample without CH when BSW current of certain amplitude and period was applied to the sample. Figures 5.26(a) – 5.26(d) presents the $V-t$ curves of sample without CH measured at $T = 102$ K and $H = 0$. To observe regular oscillations similar to those in the sample with CH, The amplitude of BSW current was chosen as 10 mA since the voltage dissipation is very small in the sample without CH. The $V-t$ measurements were carried out for BSW current with different periods of $P_I = 10$, 14, 20 and 30 s. The $V-t$ curves exhibit sinusoidal-type oscillations approximately symmetrical with respect to zero voltage line for BSW current with $P_I = 10$, 14, and 20 s as in the case of the sample with CH. However, the $V-t$ curve obtained at $P_I = 30$ s mimics the functional behavior of BSW current after the first cycle, which could be due to the relaxation effects inside the sample. We also note that the oscillation amplitude increases slightly with increasing the period of BSW current.

5.7 Magnetovoltage measurements ($V-H$ curves) as a function of magnetic field sweep rate

The magnetovoltage ($V-H$ curves) measurements on the BSCCO samples with and without CH were carried out for a constant dc current by sweeping the external magnetic field (H) up (field increase (FI)) and down (field decrease (FD)) in a field range of 0 – 60 mT. Then, the measurements are repeated after the polarity of the magnetic field is changed (reverse magnetic field region). Finally, the magnetic field is swept up once again in the forward region. Briefly, each measurement corresponding to a given value of dH/dt is completed after the five steps. The magnetic field was oriented perpendicular to the dc driving current.

Figures 5.27(a) to 5.27(c) present the $V - H$ curves obtained at T = 94 K for certain magnetic field sweep rates dH/dt (= 1, 2, and 3 mT/s) with I = 10, 15, and 20 mA, respectively. The arrows show the direction of sweeping of the magnetic field. It is evident from Fig. 5.27 that, in the forward field region, the voltage dissipation measured in the FI branch is lower than that in the FD branch. Prominent hysteresis effects are observed in the $V - H$ curves measured for I = 10 mA at dH/dt = 3 mT/s in the forward field region. However, the area enclosed between the FI and FD branches decreases with decreasing of the magnetic field sweep rate from 3 to 1 mT/s. This hysteresis effect is diminitive in the reversed field region, so that the $V - H$ curves exhibit nearly a reversible behavior for the all field sweep rates and driving current values (Figs. 5.27(a) to 5.27(c)). It is observed that the dissipation for the forward field region increases as the field sweep rate is decreased. However, the dissipation in reverse field region becomes essentially independent of the field sweep rate. The magnetovoltage curves measured at I = 15 and 20 mA exhibit an entirely different behavior from those at I = 10 mA. For instance, the sample voltage (i.e., dissipation) is not zero at H = 0 for the FD branches in the forward field region. In the reverse field region, the voltage dissipation on the FI branch increases slightly for dH/dt = 3 mT/s, and it tends to level off on the FD branch (Fig. 5.27(b)). The voltage dissipation at H = 0 on the FD branch is higher by about 15 μV than on the FI branch.

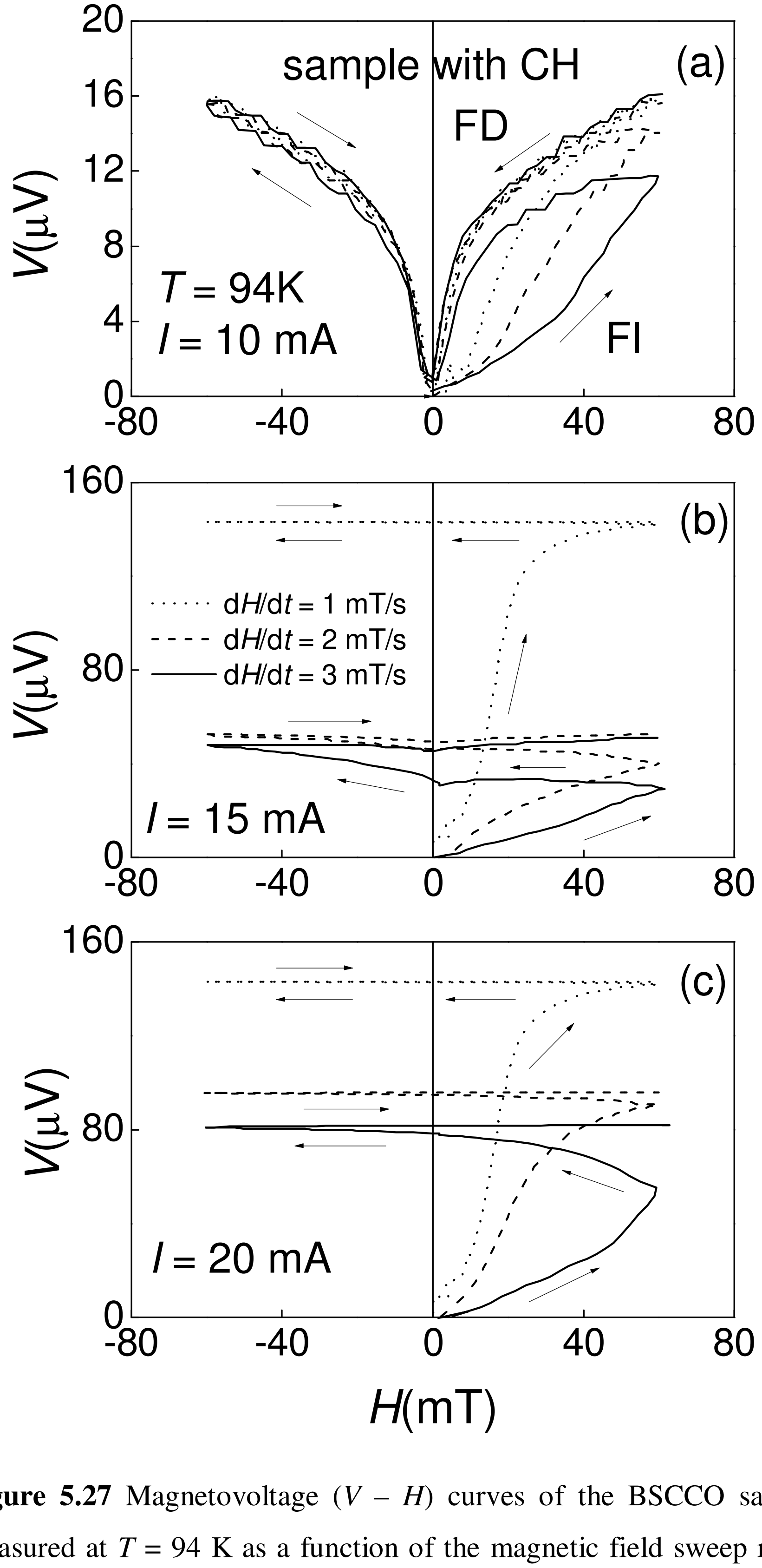

Figure 5.27 Magnetovoltage (V – H) curves of the BSCCO sample with CH measured at T = 94 K as a function of the magnetic field sweep rate (dH/dt) for different dc driving currents **(a)** I = 10, **(b)** I = 15, and **(c)** I = 20 mA. The arrows show the direction of sweeping of the external magnetic field. FI and FD refer to field increase and field decrease branches, respectively.

Finally, in the final step this voltage value remained nearly constant. The general behavior of the V - H curve obtained for dH/dt = 2 mT/s is similar to that for 3 mT/s, except that the difference between the voltage dissipations at $H = 0$, which is very small. However, he sample voltage corresponding to the V - H curve for dH/dt = 1 mT/s increases nonlinearly in the forward field region and saturates for FD branch. Furthermore, upon cycling the magnetic field in the reverse region, the voltage dissipation does not change for the FI and FD branches. This is also valid for the FI branch in the forward field region. The V - H curves measured at I = 20 mA (Fig. 5.27(c)) exhibit similar behavior with that for I = 15 mA (Fig. 5.27(b)); however, the voltage dissipation for dH/dt = 2 and 3 mT/s increases with H over the whole field range considered, while, for dH/dt = 1 mT/s, it is not changed.

In order to assess the effect of temperature (T) on the V – H curves, similar measurements were carried out at T = 89 K (Figures 5.28(a) to 5.28(c)). The V – H curves measured at 10 mA (Fig. 5.28(a)) exhibit stepwise structure and plateau on both FI and FD branches of the hysteresis loops. It can be suggested that, in the plateau regions, the effective velocity of the flux lines remains approximately constant leading to a constant flux flow rate. However, an increase in the external magnetic field favors local de-pinning of the flux lines by making the correlated flux motion unstable. In Figures 5.28(b) and 5.28(c), the steps and plateaus disappear and the V – H curves become smoother as the driving current is increased from 15 mA to 20 mA. This may be correlated with the increase in the Lorentz force due to high driving current acting on the flux lines.

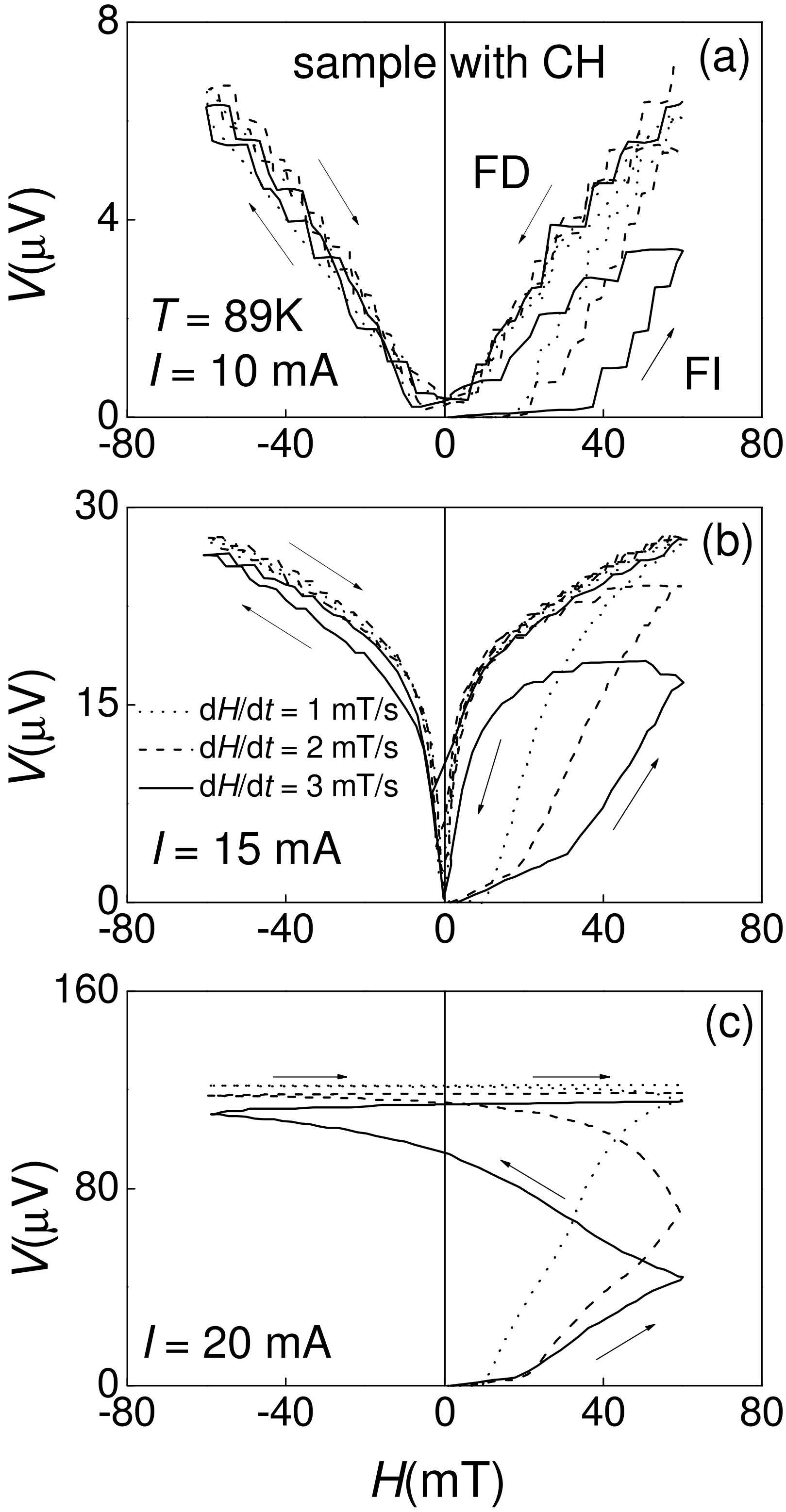

Figure 5.28 Magnetovoltage (V – H) curves of the BSCCO sample with CH for different magnetic field sweep rate (dH/dt) measured at T = 89 K with driving current **(a)** I = 10, **(b)** 15, and **(c)** 20 mA, respectively. The arrows show the direction of sweeping of the external magnetic field.

Note that the line shape of the V - H curves in Fig. 5.28(c) is similar to those in Fig. 5.27(c). Differently, the FD branches in the reversed field region and the FI branches for the fifth step in the forward region collapse nearly on the same curve.

Figure 5.29(a) presents the V - H curves corresponding to the sample without CH measured at T = 94 K and I = 50 mA for dH/dt = 1 and 3 mT/s. The V - H curves are essentially independent of the field ramping rate, so that they collapse nearly on the same curve. The $V – H$ curves of the sample without CH is obtained at T = 89 K and I = 75 mA for dH/dt =1, 2, and 3 mT/s are shown in Fig. 5.29(b). Here, the voltage dissipation on the $V – H$ curve measured for dH/dt = 3 mT/s is lower than that for dH/dt = 1 and 2 mT/s, while the $V – H$ curves for dH/dt = 1 and 2 mT/s collapse nearly on the same curve. This finding suggests that, at the given temperature and driving current, the magnetic field ramping rate is faster than the time needed for the motion of flux lines in the medium. In addition, the $V – H$ curves in Figs. 5.29(a) and 5.29(b) revealed clockwise hysteresis effect typical for HTSC ceramics in the forward field region. However, the V - H curves of the sample with CH (Figs. 5.27 and 5.28) exhibit a counterclockwise behavior, which is unusual. The reason of this counterclockwise behavior of $V – H$ curves in the BSCCO sample with CH can be attributed to the contribution of the flux trapped in CH to the measured dissipation, as the magnetic field is decreased (on the FD branches) in both the forward and reverse field regions.

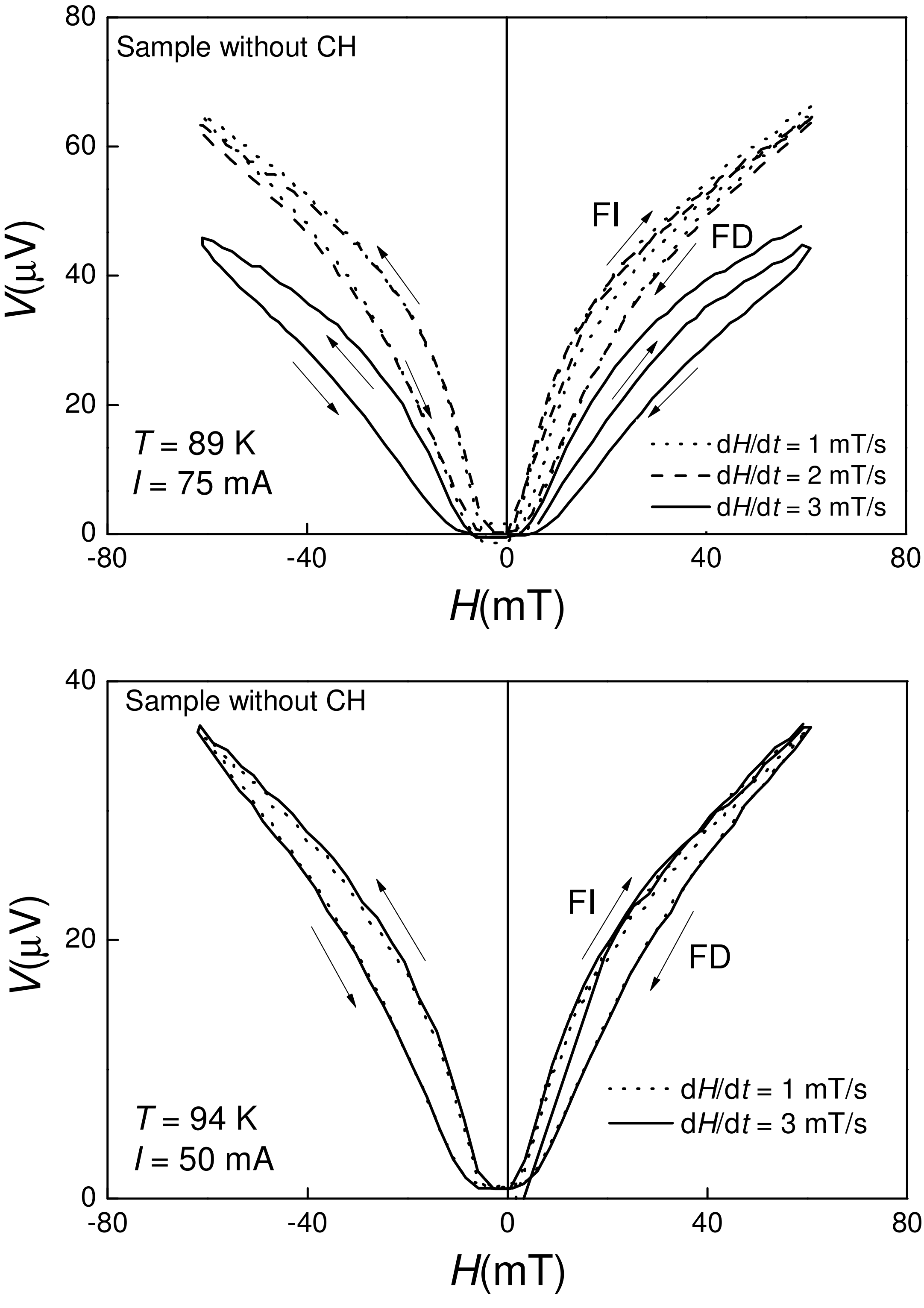

Figure 5.29 The $V - H$ curves of the BSCCO sample without CH measured at T = 94 K and I = 50 mA **(a)** for dH/dt = 1 mT/s and 3 mT/s, **(b)** for dH/dt = 1 mT/s, 2 mT/s, and 3 mT/s at T = 89 K and I = 75 mA. The arrows show the direction of sweeping of the external magnetic field.

CHAPTER 6

DISCUSSION

The experimental results, in particular, the non-linearity, hysteresis effects and downward curvature in the I - V curves, and the time effects will be discussed within the granular structure composing the polycrystalline BSCCO sample. Before discussing the experimental results, a brief introduction concerning the flux dynamics in a granular structure having a macroscopic cylindrical hole (CH) is presented. It is well known that bulk, polycrystalline high-T_c superconductors (HTSCs) show a typical weak-link behavior which can be easily destroyed by applying small magnetic field [63, 67, 95, 104–107]. A weak-link structure is assumed to behave like a type-II superconductor with its own penetration depth, first (H_{c1}^{W}) and second (H_{c2}^{W}) critical fields, and edge (surface-like) screening current flowing along the edge of the Josephson junction between grains [32, 35, 63, 67, 108]. The junction parameters can be obtained from low-field magnetization measurements (M – H). In a granular structure, it is extremely difficult to realize ideal and reversible junctions, which are not consistent with the results of low-field magnetization measurements showing hysteresis effects. By definition, the critical current (I_c) is dominated by the hysteresis phenomena, while the junction network is highly ramified and recovers the whole sample [63]. Therefore, in the interpretation of both the transport and low-field magnetization data, it is assumed that the Josephson junction barriers are very large and inhomogeneous with vortex trapping regions. This kind of junction is closer to the real situation in HTSC polycrystalline samples [32, 35, 63, 95, 106, 108].

In real experimental conditions, the sample surfaces are imperfect and possess various kinds of defects with different spatial dimensions. Surface imperfections are not equivalent physically and not equally efficient in perturbing the flux penetration within the sample. Some surface imperfections can be considered as "surface weak-links" which give rise to magnetic hysteresis at very low fields, and the local field seen by a weak-link can be considerably increased by the demagnetizing fields [63, 95]. Thus, the combination of surface weak-links and local demagnetizing fields could cause several effects in both transport and $M-H$ measurements, i.e., hysteresis effects and also losses. The flux lines do not enter the sample uniformly by overcoming the surface barriers from outer surface of the sample towards its interior, but follow different stages starting from the weakest paths of the weak-link network and ending in individual and highly superconducting grains [63, 95].

The physical description of the flux dynamics related to the sample with a macroscopic cylindrical hole (CH) would be different from that of the one without hole. When a magnetic field (or driving current) is applied to the superconducting sample, at the beginning, the macroscopic shielding currents at the surface of the sample and also around the periphery of the hole can appear within a distance comparable to the effective penetration depth λ to counterbalance the applied field- or current- induced flux lines accumulated at the surface of the sample [56, 109]. In the presence of an external magnetic field, these surface currents which circulate in opposite directions produce no magnetic flux inside the sample and inside the CH, and will not allow the flux lines to enter into the sample and also the CH. However, increasing the external magnetic field (or the driving current) can lead to penetration of the flux lines into the sample and CH [57–60, 110].

After the flux lines are penetrated from outer surface of the sample, they will move from the sample edges towards the interior of the sample along the weak pinning centers (easy motion channels) and will reach the CH. However, the flux lines may be forced to avoid the CH with the aid of the induced circulating currents and meander around it until the first flux line penetrates the CH. At this point, we note that the flux dynamics is somewhat different in the presence of only the self-field of transport current. In this case, the current-induced flux lines developing in the opposite direction and the ones coming from the opposite side of sample will annihilate each other and this can prevent further penetration of flux lines into the CH. However, due to the inhomogeneous distribution of the pinning centers inside sample, it is possible that the flux lines coming from one side of the sample can suppress the ones coming from the opposite side. Thus, the first flux line can penetrate into the CH in a complicated way at zero magnetic field.

In the presence of an external magnetic field, when another flux line enters in the CH, the two flux lines tend to stay as far apart as they can, but not to locate near the surface of the hole due to presence of the flux lines remaining outside the hole [56, 109]. The increase in the number of the flux lines in the CH will increase the interaction energy between the flux lines outside and the ones inside the CH but will also favor their repelling [56, 109]. It should be noted that the radius r of the macroscopic CH plays an important role: since r (= 0.25 mm) is much greater than the coherence length (ξ), it can be expected that its filling capacity will be quite high as compared to a microhole where $r \sim \xi$ [61, 109]. This can give an advantage to the condensation of the self-energy of flux lines. In this description, due to the competition between the attractive and repulsive interactions between the CH and the flux lines and also depending on which interaction dominates, the flux lines will be either trapped or de-trapped by CH. Another important parameter which has to be considered in the transport measurements is the sweep rates of the driving current and external magnetic field, dI/dt and dH/dt, respectively. It is natural to expect that large circulating currents can be developed at high values of dI/dt and dH/dt [61]. In particular, such a case becomes more significant in the reverse procedure used in measuring the $I - V$ curves.

6.1 Hysteresis effects in the $I - V$ curves obtained in the standard procedure

Hysteresis effects in the $I - V$ curves have been reported by many authors for both high-T_c [35, 37, 111–116] and low-T_c superconductors [38, 41, 117–119] upon sweeping the driving current up and down. Fendrich *et al.* [114] observed hysteresis effects in the $I - V$ curves of single-crystal samples of $Y_1Ba_2Cu_3O_{7-\delta}$ (YBCO) at high magnetic fields, which were interpreted as relaxation-pinning effect. The authors [114] pointed out that the observed sharp hysteresis effects depend on how the flux line lattice was formed. Sas *et al.* [116] reported history-dependent irreversibility in the $I - V$ curves of a single-crystal sample of $Bi_2Sr_2CaCu_2O_8$ (Bi-2212 phase). Xiao *et al.* [42] observed strong hysteresis effects in the $I - V$ curves of single-crystal sample of 2*H*-$NbSe_2$, which become more significant at large current ramping rates. Realistic computer simulations confirmed the presence of such hysteresis effects in the $I - V$ curves under suitable conditions [23, 120]. For instance, Reichardt *et al.* [23] found pronounced hysteresis effects in the $I - V$ curves of Type-II superconductors by using detailed molecular dynamic simulations, which depend on different dynamical vortex phases with different flow patterns. One of the possible mechanisms for hysteresis effects appearing in the $I - V$ curves of HTSCs can be the Joule heating at the current contacts. It can be suggested that the power dissipated at the current contacts can be high enough to cause such hysteresis effects in the $I - V$ curves. In our study, the measured contact resistance (see Section 4.1) is rather low. Therefore, the power dissipated at the current contacts in our samples would be about $4x10^{-6}$ W for $I_{max} = 20$ mA, and, of course, this would have no effects on the $I - V$ curves and could not be a source of the hysteresis effects observed in the $I - V$ curve of the BSCCO samples with and without CH (see Figures 5.4 to 5.9). In addition, the $I - V$ curves presented in our study do not show any marked voltage jumps and instabilities. This observation implies that the hysteresis effects in the $I - V$ curves of the samples with and without CH do not originate from hot–spot effect [121] and local heating effects evolving inside the sample. We note that the current carrying normal regions can appear due to the Joule heating and these localized regions are assumed as hot-spots.

Let us consider the $I - V$ curves measured at $H = 0$ and $H \neq 0$ for the BSCCO sample with CH (Figs. 5.4, 5.6, and 5.7), and the sample without CH (Figs. 5.8 and 5.9) and focus on the hysteresis effects. In order to describe the hysteresis effects better, the current increasing (CI) and current decreasing (CD) branches of the $I - V$ curves will be discussed separately.

6.1.1 The current - increase (CI) branch

The driving current is increased from 0 to I_{max} with a given sweep rate (dI/dt). In the CI branch, the transport current tends to distribute itself and to enter into a more ordered stable state within a dynamic re-organization. During this process, the transport current plays two different roles: one is to lower the pinning barriers by creating nucleation centers for vortices, and the other is its dynamic annealing effect on the flux line configuration [7, 32, 122]. If the current sweep rate is sufficiently high, in some regions of the sample, the increase in current can be faster than the time needed for the vortices to move, and, thus, the flux line lattice can not find enough time for re-ordering by staying in a more disordered state causing relatively low dissipation (see Figs. 5.4(a) and 5.6). At low sweep rates, it can be expected that the transport current causes an increase in the number of the nucleation centers for vortices and the vortices find enough time to re-arrange themselves into a more ordered state. Such a case can result in an enhancement in the measured dissipation.

A similar case, but less marked, is observed in the $I - V$ curves of the BSCCO sample without CH (Figs. 5.8(a) – 5.8(f)) so that the measured dissipation for this sample becomes approximately independent of dI/dt, in particular, in the I – V curves taken in the presence of external magnetic field (see Figs. 5.8(d) – 5.8(f)). It seems that the average speed of the flux lines in the BSCCO sample without CH meets the current–increase rate within the time response of the experimental set–up. In addition, in both BSCCO samples with and without CH, the critical current is not affected much by the variation of the sweeping rate of driving current in the presence of magnetic field (see Figs. 5.4(b), 5.8(d) to 5.8(f)). This case can be correlated with the weak pinning properties of polycrystalline BSCCO samples [63, 116]. On the other hand, we observe in some I – V curves (Figs. 5.4(b) and 5.7) that there are regions which exhibit changes in slope of the CI branches. These regions become more pronounced at low values of dI/dt, which can be interpreted as successive opening of new, individual easy motion channels for flux lines together with the increase in size of existing channels. It can be concluded that the current sweep rate controls the degree of current-induced organization in the sample.

6.1.2 The current - decrease (CD) branch

The I – V curves measured for the BSCCO samples with and without CH show that the measured dissipation in the CD branches is always greater than that of CI branch, which leads to hysteresis in the I – V curves (Figs. 5.4 – 5.9). The hysteresis appearing in I – V curves can be assumed as a kind of superheated state of coherent motion of flux lines which try to keep their integrity by resisting against reducing the driving current [123]. Furthermore, the superheated state associated with the CD branch represents a non-equilibrium dynamical effect since it depends clearly on dI/dt (see Fig. 5.4a). At low current sweep rates and at low currents, the measured dissipation in the CD branch of $I - V$ curves takes lower values as compared to higher current sweep rates. In this case, it can be suggested that a smooth order-to-disorder transition takes place by a gradual cooling of the superheated state, which causes to increase the bulk pinning. Finally, it can be concluded that the strong hysteresis effects in the $I - V$ curves of the BSCCO samples with and without CH arise from the different degrees of the inhomogeneous flux motion during the sweeping of the driving current up and down, respectively [17, 41, 119]. However, it is important to realize that the physical mechanisms of the hysteresis exhibited by the $I - V$ curves is different from that responsible of the hysteresis in the $M - H$ curves [35, 63]. The transport measurements are obtained by a resistivity technique, whereas, $M - H$ measurements are related to an inductive technique. The resistivity technique does not represent the bulk or intragrain critical current, but $M - H$ measurements reflect both inter and intra-grain critical currents [35, 63].

A comparison between the $I - V$ curves of the BSCCO sample with CH in Figs. 5.4(a) and 5.4(b) (also between those in Figs. 5.6 and 5.7), where the maximum current is increased from 20 to 30 mA reveals that the presence of external magnetic fields of magnitudes $H = 4$ and 8 mT causes a decrease in the hysteresis effects with respect to that of zero magnetic field. This is evident in Fig. 5.5(a), which presents the relative variation of the area of hysteresis loops as a function of dI/dt. At high magnetic fields (i.e., $H \cong 10$ mT) comparable to the characteristic magnetic fields of weak-link structure, the flux lines in the intergranular region where the weak pinning regime exists can redistribute spatially themselves within a very short time leading to a correlated flux motion under the action of the Lorentz force [35, 63, 95]. Then, the flux lines begin gradually to penetrate into the grains from their weakest points and move along easy motion channels subjecting to a dynamic competition between the pinning and depinning. As more flux lines penetrate the structure, the number of the mobile vortices inside the sample can increase and the change in vortex density can force to liberate the flux lines out of pinning centers with the help of the transport current. Thus, the measured dissipation can increase considerably leading to a correlated motion of the flux lines and hysteresis effects can decrease.

As can be seen from Figs. 5.8(d) to 5.8(f), the $I - V$ curves of the BSCCO sample without CH measured at H = 8 mT exhibit almost no hysteresis effects for all sweep rates which indicates a stable ordered state upon cycling the driving current in up and down. However, interpretation of the experimental results of the BSCCO sample with CH requires more attention, because, in addition to the flux dynamics described above, the presence of a CH directly influences the measured dissipation, hysteresis effects and line shape of the $I - V$ curves. This can be seen easily from the comparison of the $I - V$ curves measured at T = 102 K and H = 8 mT for the sample with CH (see Fig. 5.4(b)) with those for the sample without CH (see Figs. 5.8(d) – 5.8(f)). The $I - V$ curves of sample without CH are almost linear over the whole current range, which can be attributed to a typical behavior of flux flow, whereas, the ones belonging to the sample with CH continue to demonstrate a non-linear behavior over the whole current range. It can be suggested that the non-linearity in the $I - V$ curves of the latter sample originates from the presence of CH that acts as a strong (macroscopic) pinning center, which is supported by the results of several observations on the thin films or bulk samples with microholes created in microscopic level [56, 57–60, 62, 109, 110]. Indeed, the previous experimental studies related to Bitter decoration and scanning electron microscopy confirm the presence of flux trapping evolving in microholes with comparable sizes to the coherence length ξ [56, 124], and, further, the increase of microhole radius results in an enhancement of trapping of more vortices than that expected [56]. Such a case can even lead to the formation of single vortices with the vorticity more than one at the middle of hole, i.e., giant vortices [57, 110, 125]. We note that our study differs from those given mentioned since the CH considered has a diameter of 0.5 mm which is much greater the coherence length ξ.

During the measurements of the $I - V$ curves, the BSCCO sample with CH resists against increasing or reducing the driving current with the help of local circulating shielding currents in the sample volume and also the ones around the CH. As the measured dissipation suggests, it seems that the de-pinning wins mostly the competition evolving inside the CH (see Figs. 5.4(b) and 5.7). On the other hand, despite the large dissipation measured in the $I - V$ curves given in Figs. 5.4(b) and 5.7, the non-linearity in $I - V$ curves measured under magnetic field suggests that the presence of CH acts a pinning center. In addition, low current sweep rates used in the $I - V$ measurements of the sample with CH generally enhances the current-driven organization of the flux configuration leading to the enhancement in both the hysteresis effect and measured dissipation (see for instance Fig. 5.4). The $I - V$ curves of the sample without CH measured under magnetic field (Figs.

5.8(d) – 5.8(f)) suggest that as the driving current is increased, the competition between pinning and de-pinning results in favor of de-pinning due to high Lorentz force acting on flux lines, which leads to high vortex mobility, i.e., flux flow effect. The influence of CH can be seen from the comparison of the $I - V$ curves at zero magnetic field presented in Figs. 5.9(a) – 5.9(c) with those in Fig. 5.6. The presence of CH in the BSCCO sample reinforces the hyseresis effects appearing in $I - V$ curves and enhances the measured dissipation in both the CD and CI branches.

6.2 $I - V$ curves obtained in the reverse procedure

The $I - V$ curves of the BSCCO sample with CH obtained by the reverse procedure depend on dI/dt and also on the external magnetic field (Figs. 5.10, 5.13(a), and 5.13(b)]. When I_{max} = 20 mA (or 30 mA) is applied to the sample, the measured dissipation in the $I - V$ curves measured at H = 0 establish that the driving current flows mainly along the edges of the sample so that the current-induced flux lines are completely expelled from the sample. We suggest that this physical case arises mainly from the surface barriers which inhibit the entry of current-induced flux lines into the sample, i.e., the Bean-Livingston surface barriers rather than geometrical ones [126–128]. Here, there is a competition between the attraction of the flux lines to its image and the repulsion of the flux lines by the induced circulating currents along the sample [126]. However, the induced circulating currents having relatively low values evolve around the CH but in reverse direction to the one appearing in the outer surface of the sample so that the flux in the CH becomes effectively zero. Thus, in one hand, the reverse procedure considered here allows to study the surface effects on evolution of $I - V$ curves, on the other hand, it provides a way to assess how the driving current (or associated vortices) penetrates into the sample at $H = 0$.

An interesting observation in the reverse procedure is the marked difference in the line shape of RCD and RCI branches of the $I - V$ curves (see Fig. 5.10 and Figs. 5.13(a) – 5.13(b)). Here, it is important to understand the behavior of the RCD branch, because the RCI branch evolves similar to the CI branches mentioned in the previous section.

In the reverse procedure, a comparison between the zero magnetic field $I - V$ curves (Figs. 5.10, 5.13, and 5.14(a) – 5.14(c)), which were measured for the same value of dI/dt reveal that their evolution depends on both dI/dt, and the magnitude of (I_{max}) of the current applied to the sample. For I_{max} = 20 and 30 mA, the measured dissipation at $H = 0$ (Figs. 5.10 and 5.13) starts from zero voltage; whereas, in Figs. 5.14(a) – 5.14(c), it appears at a value of about 200 μV. This finding suggests that, at high values of I_{max}, the driving current penetrates into the sample immediately, and redistribute itself very rapidly along the sample as compared to that of lower I_{max} values. The redistribution process in the RCD branch includes (i) the reorganization of the driving current along the sample starting from the outer surface and (ii) the simultaneous increase in the measured dissipation. Since in the reverse procedure the driving current is reduced with a given sweep rate from a maximum current value at the beginning of the procedure, this process leads to the appearance of a response which results in a maximum voltage (V_{max}) in the RCD branch of $I - V$ curves depending clearly on dI/dt. Therefore, we suggest that the pronounced voltage difference between the RCD and RCI branches can originate mainly from the penetration of the driving current from the surface to the interior of the sample, while current sweep rate determines the number of the mobile vortices along sample [126–128].

It can be suggested that, if the current sweep rate is greater than the redistribution rate of the transport current, the measured dissipation for the RCD branch becomes negligible at $H = 0$ as demonstrated in Fig. 5.10(a). By contrast, when dI/dt is reduced, the driving current can find enough time to penetrate into the sample and also to redistribute within the sample. This could be one reason of why V_{max} values increases as shown in Fig. 5.11(a) and why V_{max} values shift to larger current values (Fig. 5.10). The I_{c1} values corresponding to the RCD branch shifted to low currents as dI/dt is increased (except the one for dI/dt = 1.25 mA/s) (see Fig. 5.11(b)), and, for the RCI branches of the $I - V$ curves in Fig. 5.10, the I_{c2} values which tend to increase with increasing dI/dt reveal that, in the fast measurements, the measurement time becomes relatively shorter than the reordering time [6], and, thus, the flux lines do not find enough time for a correlated motion. This intepretation also explains the relatively large value I_{c1} on the RCD branch obtained at dI/dt = 1.25 mA/s.

In the reverse procedure, at the beginning of measurement, I_{max} is first applied to sample and then decreased from this value with a certain sweep rate. Thus, large circulating shielding currents in the outer surface of the sample and also around CH develop depending on the magnitude of dI/dt. After the penetration of the transport current, the local circulating shielding currents developing in the volume of the sample in different sizes can produce an extra flux associated with inductivity of an induced current loop by leading to further contribution to the measured dissipation [96, 129]. However, as the process continues, in the lower current range, the local shielding currents can find sufficient time to relax and to lose its dynamic effect by causing relatively low dissipation. On the other hand, in Figs. 5.14(a) to 5.14(c) where $I_{\max} = 40$ mA, the RCD branch of the $I - V$ curve of the sample with CH remains in a more resistive state as compared to that observed in RCD branch in Fig. 5.10. We also note that, although the same current range and sweep rates were used in the measurements, there was a remarkable difference in the shape of the evolution of $I - V$ curves for the sample with CH and that of the BSCCO sample without CH at $H = 0$ (see Figs. 5.13 and 5.14). This difference can be attributed to the presence of CH. However, the $I - V$ curves of the sample without CH measured with the standard procedure under the same experimental conditions (see Figs. 5.8(a) – 5.8(c)) and in the reverse procedure do not exhibit any marked change, except the behavior of the RCD branch at the beginning of the reverse procedure. The measured dissipations of the sample without CH for $I_{\max} = 30$ and 40 mA are about 4 μV and 10 μV, respectively, whereas the voltage dissipation of the sample with CH for the same $I_{\max}$ values increases from zero to 200 μV (Figs. 5.13 and 5.14). We suggest that this difference originates from the decrease in the amount of the BSCCO material by drilling of a CH through the sample.

6.3 Downward curvature of the $I - V$ curves

The $I - V$ curves measured for the sample with CH exhibit a downward curvature at low currents. Such a behavior was observed in the $I - V$ curves of sample with CH measured in the reverse procedure at $I_{\max} = 40$ mA and $H = 0$ with current sweep rates dI/dt = 1.25 and 0.625 mA/s (Figures 5.14(a) and 5.14(b)). Fig. 5.15(a) shows the $I - V$ curve in Fig. 5.14(b) replotted in an expanded scale for a better demonstration of the downward curvature. Fig. 5.15(b) shows the $I - V$ curve measured under the same experimental conditions as in Fig. 5.15(a) by using the standard procedure. We could not observe downward curvature in the $I - V$ curves of the sample without CH in the same experimental conditions used as for the sample with CH. Therefore, we suggest that the downward curvature in the $I - V$ curves at low applied current is originated from the presence of CH drilled through the sample, which can behave as an attractive or repulsive macroscopic pinning center depending on both dI/dt and the magnitude of the Lorentz force acting on flux lines.

We suggest that, at low applied currents, the CH acts initially as a repulsive macroscopic pinning center. As described above, the shielding currents circulating around the CH prevent the flux variation inside the CH and try to keep a flux free region by enhancing the superconducting order parameter around it. However, as the driving current is increased, some flux lines enter into the CH via the weakest points. The flux lines can be trapped in there and, as a consequence, the CH acts as an attractive macroscopic pinning center for flux lines leading to a decrease in the measured dissipation. Thus, a downward curvature would appear in the $I - V$

curves although the applied current is increased. However, for low values of dI/dt, the flux lines find enough time to reorganize themselves and the downward curvature in the $I - V$ curves disappears (see for instance Fig. 5.14(c)).

6.4 The time evolution of the sample voltage: $V - t$ curves

The non-linear growth in $V - t$ curves represented in Figures 5.16, 5.17, 5.19, and 5.20 can be attributed to the reorganization of the driving current with complex flow patterns in the volume of the sample as the time progress [103]. In this process, the transport current penetrates into the sample from the edges and creates many channels consisting of normal (resistive) regions by suppressing locally the superconducting order parameter in the regions where the superconductivity is weak. After this step, the transport current moves from the sample edges towards the interior of the sample along weak pinning centers (i.e., easy motion channels). As the time progresses, the measured dissipation enhances for all $V - t$ curves, which can be considered as a measure of the enhancement in the resistive flow channels depending on the structural disorder of the sample. However, for the sample with CH, the current dependent reorganization is expected to be different due to the presence of CH. At early times of the relaxation process, the driving current will try to avoid the CH by flowing around it due to the macroscopic shielding circulating current around the periphery of the CH within a distance comparable to the effective penetration depth [130]. Note that the measured dissipation for the $V - t$ curves of the sample with CH tends to increase slightly with time before the initial current (I_1) is interrupted or reduced to a finite value (I_2), as compared to that of the sample without CH. This implies that the dynamic process concerning the reorganization of the driving current is still active, so that, in one hand, the flux lines (or current-induced flux lines) penetrate and nucleate within the CH, on the other hand, some of them leave the CH and contribute to the measured dissipation.

When $I_2 = 0$, the sample voltage becomes zero, such that no trace of relaxation effects is observed (see Figures 5.16, 5.19, and 5.20). However, it is important to discuss the physical meaning of the V - t curves observed for $I_2 \neq 0$. When I_1 is suddenly reduced to I_2, first, an abrupt drop in the voltage of the sample with CH is observed, and, then, the quenched state which appears due to the sudden decrease in the driving current decays over time. The abrupt drop in the sample voltage results in a state of quenched disorder created by I_2 and can be correlated with supercooling. Here, it is assumed that the driving current plays the role of temperature, as in the usual sense in statistical mechanics [7, 32]. Note that the relaxation of the quenched state evolves in the form of steps which continue for some time (see Fig. 5.16). However, in the $V - t$ curves of the sample without CH (see Fig. 5.17), the time evolution of the quenched state shows a quite smooth decrease up to a critical time t_c, (Fig. 6.1), which depends on the magnitude of I_2. t_c is defined as the time passed until the voltage response levels off, after I_1 is reduced to I_2. For $t > t_c$, the voltage response levels off at long times of the relaxation process and a step-wise behavior is not observed. The increase of t_c with I_2 means that the reorganization of the driving current along the whole sample takes long times. The step-wise behavior observed in $V - t$ curves of the sample with CH (see the inset of Fig. 5.16) can be related to the leaving of current-induced magnetic flux lines through the area of the CH and to the superconducting surface effects near the CH edge.

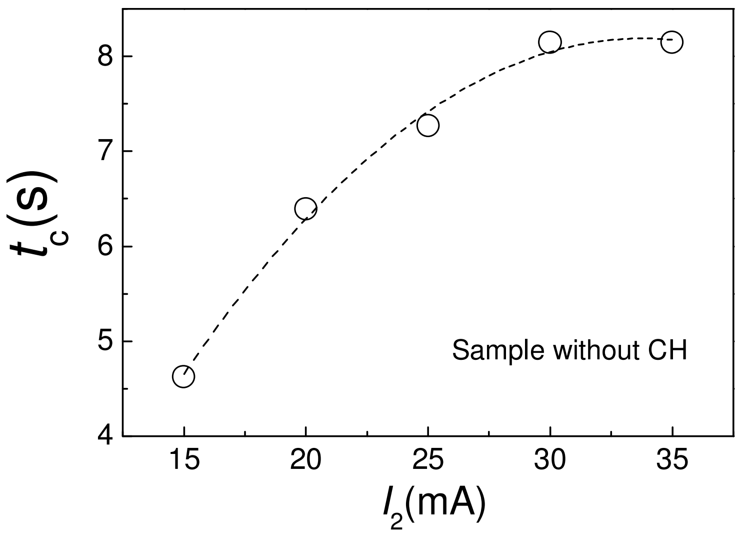

Figure 6.1 The variation of the critical time t_c as a function of I_2. The data were extracted from the $V - t$ curves for the sample without CH given in Fig. 5.17.

The nature of voltage decays in the $V - t$ curves of the samples with and without CH can be described by some current models [85, 94, 99, 103]. According to the modified flux flow and the resistive weak-link models [85, 94], in transport relaxation measurements, the decrease of the sample voltage follows a logarithmic time dependence given in Equation (3.5). On the other hand, some experimental observations provide some evidence that the glassy state relaxation fits a stretched exponential time dependence of the form ~ exp $(-t/t_0)^{\alpha}$ at long times. Here, both the characteristic time t_0 and the exponent α depend on the driving current and temperature [85, 103]. We now show that the decrease in voltage at the currents of $I_2 > 8$ mA in Fig. 5.16 and the voltage decays in Figs. 5.17, 5.19, and 5.20 can be described by the empirical relation in Equation (3.1) which is analogous to the glassy state relaxation [103]. The solid lines in these figures which are calculated by using Equation (3.1) show reasonable agreements with the experimental data. The t_0 values found from the fitting procedure is plotted as a function of I_2 in Fig. 6.2.

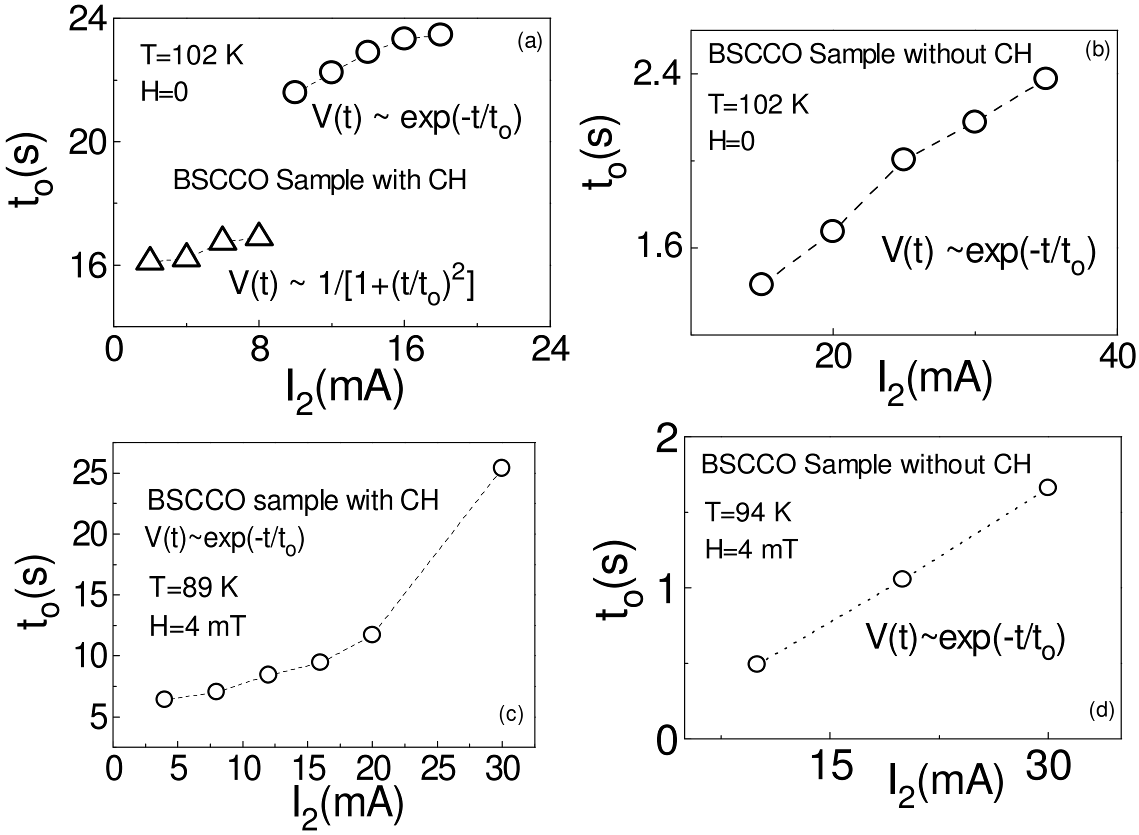

Figure 6.2 The variation of the characteristic time t_0 with the current I_2. The data were extracted from the fitting procedure to data points given in **(a)** Fig. 5.16, **(b)** Fig. 5.17, **(c)** Fig. 5.19, and **(d)** Fig. 5.20.

It is seen that t_0 increases with I_2. This could be expected because the transitions to the low dissipation (superconducting) state at low driving currents are much faster than those at higher currents. In fact, a quenched disorder can be created by interrupting abruptly the driving current or reducing it to a finite value. The voltage decays in time, whichever they fit (either Equations (3.1) or (3.5)), should include structural disorder due to the frustrated superconducting domains coupled by weak links and quenched disorder created in the flux lines. However, below 10 mA, the $V - t$ curves in Fig. 5.16 give more reasonable agreement with the emprical relation $V(t) \sim 1/[1+(t/t_0)^2]$ ([108]) rather than Equation (3.1) (see the dashed lines in Fig. 5.16). This expression describes well the small voltage hump at the onset of the relaxation process just after the initial current I_1 is reduced abruptly to I_2. We suggest that the voltage hump observed at the currents below 8 mA could be due to the current-induced flux trapped inside CH.

6.5 The coherent voltage oscillations

The flux dynamics in type-II superconductors depends also on the type of the driving current modulations such as square wave, symmetrical and asymmetrical square waves [3, 4] and sinusoidal forms [28]. It has been observed that the vortex mobility in single crystalline samples of 2*H*-$NbSe_2$ increases as the square wave currents applied to the sample [3, 4, 34]. This implies that the motion of vortices becomes more ordered along the sample for a driving current of square wave form. Another interesting study [3, 4] demonstrated that the response of the twinned single crystalline samples of $Y_1Ba_2Cu_3O_{7-\delta}$ to an asymmetrical square wave current is in the form of slow voltage oscillations. Similar voltage oscillations have been observed for symmetrical bi-directional square wave (BSW) currents in polycrystalline samples of $Y_1Ba_2Cu_3O_{7-\delta}$ on long time scales.

In this study, regular *sinusoidal-like* voltage oscillations are observed at certain temperatures and magnetic fields as functions of both the amplitude and period of the symmetric BSW current (see Figs. 5.21 and 5.23 to 5.26). The amplitude of the response is of the same order (i.e., in the range from 10^{-7} to 10^{-6} V) as found in the studies by Gordeev *et al*. [3, 4] and Kwok *et al.* [28].

In the present work, we observed, for the first time, long period oscillations in the response to a BSW driving current in polycrystalline BSCCO samples with and without CH. In our measurements, the period of the response oscillations compares well with the period of BSW drive (see Fig. 5.22), in contrary to the study by Goordev *et al.* [3]. We suggest that these current-induced voltage oscillations is similar to the phenomena observed in the dynamics of sliding charge-density waves (CDWs), and represents fundamentally a new kind of vortex dynamics. In the study by Goordev *et al.* [3, 4], the regular voltage oscillations were described as the transit of periodic vortex density fluctuations and it was shown that the motion of vortices in the weak-bulk-pinning regime resembles the sliding CDWs [131–139]. In our present work, we suggest that coherent density fluctuations of flux lines along the sample can develop depending on the amplitude and period of driving BSW current and can lead to a similar effect as in the case of the CDWs. The flux lines can drift back and forth transversely and can remain in an oscillating mode by causing regular voltage oscillations. Here, the oscillating mode can be correlated to the defective flow of flux lines (or current-induced self-magnetic flux (SMF) lines) in a multiply connected network. In addition, the symmetry seen in voltage oscillations suggests that there can be an elastic coupling between the flux lines and pinning centers.

The effects of the period and amplitude of driving BSW current can be seen in the $V - t$ curves presented in Figs. 5.21 and 5.23 – 5.26. At a given temperature and external magnetic field, when the period or amplitude of the applied drive is increased, the coherent voltage oscillations begin to turn into a square wave type response at longer times (see for instance Fig. 5.23 and Fig. 5.26). We suggest that the competition between pinning and depinning plays a central role in the evolution of distorted voltage oscillations. In this physical description, the type of the pinning centers and the pinning strength determine the flow pattern of flux lines evolving inside the sample. Thus, at long periods and large amplitudes of the BSW current, pronounced relaxation effects can occur due to this competition, so that the flux lines (or current induced SMF lines) can find new accessible states in a multiply connected weak-link structure of intergranular regions while they try to go to a new equilibrium state in time during the positive or negative parts of the driving current. This can be taken as one of the main reasons why regularities or distortions appear in the evolution of some of the $V - t$ curves (see, Figs. 5.21 and 5.23 – 5.26). All these observations indicate that there is always a threshold value of the period (or magnitude) of the driving current, which determines whether the regular sinusoidal-like oscillations occur or not in the given temperature and magnetic field regions.

The amplitude of BSW drive applied to the sample with CH was 1 mA (see Fig. 5.21); whereas, that for the sample without CH was 10 mA (Fig. 5.26). The amplitudes of BSW drive applied to the samples with and without CH must be different to be able to observe the regular oscillations, because some amount of the superconducting material is removed from the sample by drilling a CH. The local circulating shielding currents within the sample and also around CH evolving against the drive cause an increase in the voltage dissipation. Therefore, it is possible to observe the voltage oscillations in the sample with CH even at low current values. However, high driving current values are needed for the sample without CH in order to observe the regular oscillations similar to the ones for the sample with CH. At the early stage of the dynamic process, CH can behave as a macroscopic pinning center for flux lines and can capture them. As the driving current alternates periodically, some of the flux lines can leave the CH due to the repulsive interactions between the flux lines inside the volume of the CH by joining the vortex motion inside the sample. That is, the CH contributes positively to the measured dissipation during all dynamic processes. Therefore, in the vicinity of critical temperature region (i.e., $T < T_c$), sinusoidal-like oscillations in the sample voltage could undergo deformation even at small amplitude and sufficiently long period of the BSW current (see Fig. 5.23).

Another interesting feature of the $V - t$ curves for the sample with CH is that the voltage oscillations remain positive over some time interval, despite the fact that the driving current is bidirectional (Fig. 5.25). When the polarity of the driving current changes, the direction of the current-induced flux lines is expected to change accordingly, in addition, the sample voltage developing in the direction of the current would also follow the polarity change of the driving current. We suggest that the pinning and relaxation effects dominate effectively the flux motion at $T = 96$ K and they do not permit the spatial reorganization of the flux lines. Thus, the measured dissipation can not return back to zero or find enough time to achieve a negative value. However, as the time evolves, the alternating driving current leads to an increase in the measured voltage by facilitating the formation and growth of easy-motion flow channels for flux lines. Thus, the motion of flux lines becomes more ordered along such easy-motion channels which evolve gradually. The symmetry seen in the voltage responses obtained for the sample with CH suggests that the ordered motion of flux lines leave the sample and follows the same flow channels.

Finally, when the period and magnitude of the BSW drive are sufficiently large, the drive and voltage response follow each other at the temperatures just below T_c. In this case, no phase difference between the drive and response evolves due to the relaxation effects. In addition, the measured magnitude of the voltage response suggests that the flux dynamics develops in the intergranular region where the local superconducting order parameter is strongly suppressed. According to the experimental results presented in Figs. 5.21 and 5.23– 5.26, voltage distortion in the samples with and without CH is observed at the dissipation levels above about 0.4 μV. A similar case was observed in polycrystalline YBCO by Kiliç *et al.* [44]. The authors showed that, when the dissipation reaches or exceeds 1 μV, the regular voltage oscillations evolve in the form of bi-directional square wave by reflecting the polarity change of drive. It is well known that 1 μV is commonly accepted as a criterion in critical current measurements. Therefore, 1 μV can be taken as a reference voltage value for the destruction of the weak-link structure in polycrystalline YBCO sample. We suggest that, for polycrystalline BSCCO samples with and without CH used in the present study, this value should be less than 1 μV and could be about 0.4 μV. Thus, for practical applications such as magnet designs, this lower voltage value where the distortions are observed can be considered as a new voltage criterion (instead of 1 μV) in determining of the critical current of BSCCO.

6. 6 Magnetovoltage measurements as a function of magnetic field sweep rate

It is well-known that strong irreversibility effects appear both in magnetization and magnetovoltage measurements on high-T_c superconductors at low, moderate and high magnetic fields [61, 63, 71]. The hysteresis effects in magnetovoltage measurements ($V - H$ curves) of HTSCs evolve generally in the clockwise direction as the external field is swept up and down in the forward region. The irreversibility effects observed in the $V - H$ curves of HTSCs are attributed mainly to the flux trapping developed in both intergranular and intragranular regions of the material [71, 140].

Several models have been proposed to explain the hysteresis effects observed in the $V - H$ curves of superconductors. One of them is the two-level critical state model proposed by Ji *et al.* [69]. In this model, the macroscopic and local magnetic fields are calculated for ordered and disordered polycrystalline superconducting samples by assuming that the flux dynamics is maintained by the percolative paths through the grains. Beloborodov *et al.* [141] proposed a model which is in reasonable agreement with the experimental results concerning the negative magnetoresistance observed in a granular superconducting Al sample

[142]. Palau *et al.* [143] showed that the irreversibility effects arise from the magnetic flux trapped in the grains returning through the grain boundaries (i.e., return flux), i.e., from grains into the grain boundaries. Recently, Garcia-Fornaris *et al.* [140] reported that the magnetoresistance of polycrystalline HTSCs can be reproduced in the framework of intragranular flux trapping model. In this model, which is based on previous studies by Chen and Qian [144] and Qian *et al.* [145], it is assumed that the superconductor is composed of series and parallel connected arrays of Josephson junctions and the effective magnetic field along intergranular region arises from the magnetic field trapped inside the grains.

The $V - H$ curves measured for the BSCCO sample without CH exhibit typical clockwise hysteresis curves in the forward field region (Figs. 5.29(a) and 5.29(b)), as found previously for polycrystalline HTSCs [71]. We suggest that this type of hysteresis effects in the $V - H$ curves are mainly related to the return flux going through the grain boundaries and generated by the field trapped in the grains [71, 144]. This can explain the usual clockwise hysteresis effects in Figs. 5.29(a) and 5.29(b). However, the $V - H$ curves measured for the BSCCO sample with CH exhibit an unusual counter-clockwise behavior in the forward field region (Figs. 5.27 and 5.28). We suggest that this behavior originates from the contribution of the flux trapped in CH to the measured dissipation as the magnetic field is decreased. When the magnetic field is decreased, due to the field gradient evolving in within the sample, the flux trapped inside CH can penetrate into the sample so that CH behaves as a flux reservoir. This would enhance the measured dissipation developing in the direction of driving current and lead to the saturation of the sample voltage at high magnetic fields by enhancing the reversibility in $V-H$ curves of the sample with CH (Figs. 5.27(b) - 5.27(c) and 5.28(c)). Thus, the mobile flux lines reach an equilibrium state (i.e., correlated flux motion). We also note that cycling the external magnetic field in the forward and reverse directions with different sweep rates results in an increase in the number of the flux lines participating the flux motion both inside the CH and remaining part of sample, which results in a pronounced asymmetry observed in $V-H$ curves in Figs. 5.27(b) - 5.27(c) and 5.28(c).

It is evident from the $V-H$ curves of the samples with and without CH (see Figs. 5.27 to 5.29) that the non–linearity, which is a measure of the voltage dissipation rate correlated with dV/dH, depends on the temperature, magnitude of the transport current and magnetic field sweep rate dH/dt. Both the line shape of $V-H$ curves and the measured dissipation strongly depend on dH/dt. This implies that variation of dH/dt serves to control the number of flux lines inside the sample and also inside CH, so that the variation of dH/dt leads to a large difference between the measured dissipations corresponding to the dH/dt values of 1 mT/s and 3 mT/s, respectively. It can be suggested that, at low sweep rates, the flux lines find enough time to penetrate into the sample, and, thus, the increase in the number of flux lines participating the flux motion causes an enhancement in the measured voltage dissipation. Cycling the magnetic field brings strong reversible behavior, as observed in the $V-H$ curves, depending on the magnitudes of magnetic field and driving current (Figs. 5.27(b) and 5.27(c)). In addition, the dependence of sample voltage on dH/dt shows that the number of the flux lines inside the CH and that within the sample is not equal to each other for every $V-H$ curve.

However, the $V-H$ curves obtained for the sample without CH (Figs. 5.29(a) and 5.29(b), except the one obtained for dH/dt = 3 mT/s) are practically independent of the value of dH/dt. We suggest that the flux lines find enough time to move in the sample at the low values of the magnetic field rate and the $V-H$ curves collapse nearly on the same curve due to the weak pinning properties of BSCCO [61, 63], i.e., the hysteresis disappears. Here, we note that the maximum number of the flux lines (n_v) inside the CH can be controlled by the variation of dH/dt. Thus, it appears that the dependences of the $V-H$ and $I-V$ curves on the sweep rates dH/dt and dI/dt, respectively, provide useful tools to assess whether a CH can behave as a macroscopic pinning center or not.

Finally, we show that the CH drilled through the BSCCO sample can trap the magnetic flux lines. A normal region in the form of a cylinder (metallic or insulating) or a cylindrical hole attracts the flux lines because a flux line tries to save core energy when it is located at a defect, provided that the radius (r) of the defect is greater than the effective coherence length (ξ) [15, 56–62, 109, 110, 125, 146, 147]. Mkrtchyan and Shmidt [146] showed that the maximum number of flux lines, n_v, which can be trapped inside the columnar defect (i.e., an empty cylindrical cavity), is proportional to ~ $r/2\xi(T)$. In our case, the radius of the CH drilled in BSCCO sample is r = 0.25 mm, hence, $r >> \xi$. Thus, the CH should set an attractive potential energy to incoming flux lines, and, hence, should trap a large number of flux lines as compared to that of a microhole. Substituting the reasonable values of r = 0.25 mm, $\xi \sim 1$ nm [63] for BSCCO, we find that $n_v \sim 10^5$. On the other hand, the magnetic flux Φ through the cross section area of the CH can be found from the expressions $\Phi = H_s A_{CH} = n_c \Phi_o$. Here, H_s is the external magnetic field at which the $V - H$ curves saturate, A_{CH} is the cross sectional area of the CH, n_c is the number of the flux lines in the sample and Φ_o is the flux quantum. Using $H_s \sim 60$ mT (see Fig. 5.27(c), the $V - H$ curve taken for $I = 20$ mA) and $\Phi_o \sim 2\text{x}10^{-15}$ Tm^2 [73], we find that $n_c \sim 10^6$, so that $n_c > n_v$. This rough estimation shows that the CH has a higher filling capacity than the one predicted in Ref. [146], where a CH with $r << \lambda$ was considered. This difference may be related to the formation of multiple-quanta vortices inside CH [56, 57, 59, 146]. Buzdin [57] showed analytically that the multiple-quanta vortices on columnar defects become energetically favorable provided that $r^3 < \xi(T)\lambda(T)^2$. For a macroscopic CH, as in our case, however, it is clear that the latter condition is not satisfied and it seems that the finding of $n_c > n_v$ does not originate from the presence of multiple-quanta vortices inside the CH. Thus, during the cycling of the external magnetic field, one can rule out the formation of multiple-quanta vortices and their breaking up single-quantum vortex, and also their contribution to the measured dissipation. We suggest that the finding $n_c > n_v$ can originate from the substantial attractive potential energy of the macroscopic CH and high degree compressibility of flux lines due to their large elastic modulus C_{11} [10] as compared to a microscopic columnar defect (i.e., microscopic hole). In the presence of a CH, the energy of the Abrikosov vortex per unit length can be written [80] as

$$E_v = \left[\frac{\Phi_0}{4\pi\lambda}\right]^2 \ln(\frac{\lambda}{r}), \qquad (6.1)$$

where Φ_0 is the flux quantum and λ is the penetration depth. Since $r >> \xi$ and $E_V < 0$, the CH exerts an attractive potential to the flux lines and this allows the vortices to penetrate inside the CH at a magnetic field which is smaller than the bulk lower critical field of BSCCO (i.e., $H_{c1} \approx 20$ G and $H_{c2} \approx 5$ T at 102 K (see for instance Ref. [63]).

CHAPTER 7

CONCLUSIONS

In this study, the flux dynamics in polycrystalline $Bi_{1.7}Pb_{0.3}Sr_2Ca_2Cu_3O_x$ (BSCCO) sample with a macroscopic cylindrical hole (CH) drilled through it was investigated by means of the transport and magnetovoltage measurements at the temperatures just below T_c. The results were compared with similar measurements performed on the original BSCCO sample before drilling the CH.

This comprehensive experimental study includes measurements of current-voltage ($I - V$) curves for different current sweep rates (dI/dt) of the transport current, transport relaxation ($V - t$) curves at zero magnetic field ($H = 0$) and also in the presence of an external magnetic field H, slow voltage oscillations, and magnetovoltage ($V - H$) curves as a function of the magnetic field sweep rate dH/dt. We found that the distribution of the transport current and the current-induced reorganization of the magnetic flux lines within the sample with CH take relatively long times leading to a strong dependence of $I - V$ curves on dI/dt. We observed that hysteresis effects evolve upon cycling of the transport current up (the current-increase (CI) branch) and down (the current-decrease (CD) branch) direction, which tend to increase as dI/dt decreases, contrary to the case observed in the sample without CH. Observation of high dissipation in the CD branch (especially at high transport currents) was interpreted as a kind of superheated state. Further, in the presence of an external magnetic field, the hysteresis effects in the $I - V$ curves of the sample without CH almost disappear pointing to flux flow effects. However, for the same magnetic field, temperature, maximum current (I_{max}) and current sweep rates, the non-linearity in the $I - V$ curves of the sample with CH is still observed with enhanced dissipation. The $I - V$ curves of the sample with CH obtained in the reverse procedure revealed several interesting features. One of them is the pronounced difference between the RCI and RCD branches of the $I - V$ curves, which reflects itself as a remarkable voltage maximum on the RCD branch. The reverse procedure enables us to study how the driving current (or magnetic flux lines) penetrates into the sample from its outer surface (i.e., the surface effects). A downward curvature is observed in the low current region and at high values of dI/dt. Interpretation of the experimental results established that, under certain conditions, the CH acts as a macroscopic pinning center. It is also established that the current sweep rate dI/dt controls the degree of current-induced organization of the magnetic flux lines in the sample.

It was shown that the relaxation of the magnetic flux trapped inside the sample with CH can be monitored, via slow transport relaxation measurements ($V - t$ curves), by creating a quenched state which occurs as a result of a sudden decrease of the transport current from I_1 to I_2. We observed that the time evolution of quenched state of the sample with CH develops in steps, which is correlated with leaving of magnetic flux from inside the CH and with surface effects. The voltage decays at high values of I_2 are generally consistent with an exponential relationship, which is analogous to that of the glassy state relaxation. In the $V - t$ curves of the sample without CH, the time evolution of quenched state is quite smooth and the sample voltage levels off after a certain critical time value (t_c), which depends on the value of I_2. It was found that the voltage decays observed in the sample without CH also show reasonable agreements with an exponential relationship associated with glassy state relaxation. At long times of the relaxation process, the non-zero voltage dissipation rate ($\mathrm{d}V/\mathrm{d}t$) observed in $V-t$ curves the sample with CH implies that the steady state is not reached yet and the dynamic process concerning the penetration of the driving current into the sample is still active.

The time evolution of the sample voltage ($V-t$ curves) at low dissipation levels was investigated by applying bidirectional square wave (BSW) current of long period to the BSCCO samples with and without CH. The measurements were carried out as functions of temperature, amplitude and period of the BSW drive, at $H = 0$ and $H \neq 0$, for both short and intermediate time scales. We observed that, for both samples, regular sinusoidal type oscillations evolve in certain ranges of the amplitude and period of the BSW drive, external magnetic field, and temperature. The sinusoidal and non-sinusoidal oscillations on the $V-t$ curves were discussed in terms of the dynamic competition between pinning and depinning, and the possible relaxation effects. The defective flow of magnetic flux lines (or current-induced self magnetic flux (SMF) lines) in a multiply connected network and the elastic coupling among flux lines and pinning centers can cause such regular oscillations of the sample voltage as a function of time.

The magnetovoltage measurements ($V-H$ curves) showed that the measured dissipation depends strongly on $\mathrm{d}H/\mathrm{d}t$ for the sample with CH; whereas, the $V-H$

curves for the sample without CH are essentially independent of dH/dt. We observed counter-clockwise hysteresis effects in the $V - H$ curves of sample with CH, upon cycling the external magnetic field. These hysteresis effects were considered as an evidence of flux trapping in the CH. Further, as the external magnetic field is decreased, the trapped flux inside the CH can cause a repulsive interaction with the flux lines present in the bulk of the sample, and, thus the CH tries to prevent the flux trapping by enhancing the measured dissipation. The CH drilled through the BSCCO sample behaves as a flux reservoir by increasing the number of the flux lines joining the flux motion inside the sample. In addition, the magnetic field sweep rate dependence of the sample voltage shows that the numbers of the flux lines inside the sample and in the CH are not equal to each other, and this results in counter-clockwise hysteresis effects in the $V - H$ curves measured for the sample with CH.

Finally, we note that drilling a macroscopic CH through the BSCCO sample can provide a useful tool in designing SQUIDs. In these devices, a few strategically introduced holes can trap the vortices and reduce the noise by increasing their performance. Therefore, some of the experimental methods used in this study introduce new techniques to investigate such superconducting samples designed for practical applications. As a future work, systematic molecular dynamic simulations will be performed in a two-dimensional superconducting sample consisting of periodic pinning arrays with a radius comparable to the coherence length and penetration depth. In the numerical simulations, the overdamped equation of motion of a vortex will be solved for a pinning force derived from the interaction potential energy by Nordborg and Vinokur [109]. The results will be compared to the experimental data presented in this thesis and also to Bitter decoration experiments [56, 124].

REFERENCES

[1] S. Bhattacharya, M. J. Higgins, *Dynamics of a Disordered Flux Line Lattice*, Phys. Rev. Lett. **70**, 2617 (1993).

[2] S. Bhattacharya, M. J. Higgins, *Peak Effect and Anomalous Flow Behavior of a Flux-Line Lattice*, Phys. Rev. B **49**, 10005 (1995).

[3] S. N. Gordeev, P. A. J. de Groot, M. Oussena, A. V. Volkozup, S. Pinfold, R. Langan, R. Gagnon, L. Taillefer, *Current-Induced Organization of Vortex Motion in Type-II Superconductors*, Nature **385**, 324 (1997).

[4] S. N. Gordeev, P. A. J. de Groot, M. Oussena, R. M. Langan, A. P. Rassau, R. Gagnon, L. Taillefer, *Organisation of Vortex Motion in Detwinned* $YBa_2Cu_3O_{7-\delta}$ *Single Crystals*, Physica C **282**, 2033 (1997).

[5] M. C. Hellerqvist, A. Kapitulnik, *Current-Induced Ordering of Vortices in Two-Dimensional Amorphous* $Mo_{77}Ge_{23}$ *Films as a Function of Film Thickness and Magnetic Field*, Phys. Rev. B **56**, 5521 (1997).

[6] Z. L. Xiao, E. Y. Andrei, M. J. Higgins, *Flow Induced Organization and Memory of a Vortex Lattice*, Phys. Rev. Lett. **83**, 1664 (1999).

[7] Y. Paltiel, E. Zeldov, Y. N. Myasoedov, H. Shtrikman, S. Bhattacharya, M. J. Higgins, Z. L. Xiao, P. L. Gammel, D. J. Bishop, *Dynamic Instabilities and Memory Effects in Vortex Matter*, Nature **403**, 398 (2000).

[8] Z. L. Xiao, E. Y. Andrei, P. Shuk, M. Greenbatt, *Depinning of a Metastable Disordered Vortex Lattice*, Phys. Rev. Lett. **86**, 2431 (2001).

[9] G. Blatter, M. V. Feigel'man, V. B. Geshkenbein, A. I. Larkin, V. M. Vinokur, *Vortices in High-Temperature Superconductors*, Rev. Mod. Phys. B **66**, 1125 (1994).

[10] E. H. Brandt, *The Flux-Line Lattice in Superconductors*, Rep. Prog. Phys. **58**, 1465 (1995).

[11] A. C. Shi, A. J. Berlinsky, *Pinning and I – V Characteristics of a Two-Dimensional Defective Flux-Line Lattice*, Phys. Rev. Lett. **67**, 1926 (1991).

[12] A. E. Koshelev, V. M. Vinokur, *Dynamic Melting of the Vortex Lattice*, Phys. Rev. Lett. **73**, 3580 (1994).

[13] A. Richardson, O. Pla, F. Nori, *Confirmation of the Modified Bean Model from Simulations of Superconducting Vortices*, Phys. Rev. Lett. **72**, 1268 (1994).

[14] C. Reichhardt, C. J. Olson, J. Groth, S. B. Field, F. Nori, *Microscopic Derivation of Magnetic-Flux-Density Profiles, Magnetization Hysteresis Loops, and Critical Currents in Strongly Pinned Superconductors*, Phys. Rev. B **52**, 10441 (1995).

[15] C. Reichhardt, C. J. Olson, J. Groth, S. B. Field, F. Nori, *Vortex plastic flow, local flux density, magnetization hysteresis loops, and critical current, deep in the Bose-glass and Mott-insulator regimes*, Phys. Rev. B **53**, R8898 (1996).

[16] C. Reichhardt, C. J. Olson, J. Groth, S. B. Field, F. Nori, *Spatiotemporal Dynamics and Plastic Flow of Vortices in Superconductors with Periodic Arrays of Pinning Sites*, Phys. Rev. B **54**, 16108 (1996).

[17] C. Reichhardt, C. J. Olson, J. Groth, S. B. Field, F. Nori, *Erratum: Spatiotemporal Dynamics and Plastic Flow of Vortices in Superconductors with Periodic Arrays of Pinning Sites*, Phys. Rev. B **56**, 14196 (1997).

[18] C. J. Olson, C. Reichhardt, J. Groth, S. B. Field, F. Nori, *Plastic Flow, Voltage Noise and Vortex Avalanches in Superconductors*, Physica C **290**, 89 (1997).

[19] C. J. Olson, C. Reichhardt, F. Nori, *Superconducting Vortex Avalanches, Voltage Bursts, and Vortex Plastic Flow: Effect of the Microscopic Pinning Landscape on the Macroscopic Properties*, Phys. Rev. B **56**, 6175 (1997).

[20] C. Reichhardt, C. J. Olson, F. Nori, *Dynamic Phases of Vortices in Superconductors with Periodic Pinning*, Phys. Rev. Lett. **78**, 2648 (1997).

[21] C. Reichhardt, C. J. Olson, F. Nori, *Commensurate and Incommensurate Vortex States in Superconductors with Periodic Pinning Arrays*, Phys. Rev. B **57**, 7937 (1998).

[22] C. J. Olson, C. Reichhardt, F. Nori, *Nonequilibrium Dynamic Phase Diagram for Vortex Lattices*, Phys. Rev. Lett. **81**, 3757 (1998).

[23] C. Reichhardt, C. J. Olson, F. Nori, *Nonequilibrium Dynamic Phases and Plastic Flow of Driven Vortex Lattices in Superconductors with Periodic Arrays of Pinning Sites*, Phys. Rev. B **58**, 6534 (1998).

[24] C. Reichhardt, C. J. Olson, F. Nori, *Fractal Networks, Braiding Channels, and Voltage Noise in Intermittenly Flowing Rivers of Quantized Magnetic Flux*, Phys. Rev. Lett. **80**, 2197 (1998).

[25] C. Reichhardt, F. Nori, *Phase Locking, Devil's Staircases, Farey Trees, and Arnold Tongues in Driven Vortex Lattices with Periodic Pinning*, Phys. Rev. Lett. **82**, 414 (1999).

[26] A. P. Mehta, C. J. Olson, C. Reichhardt, F. Nori, *Topological Invariants in Microscopic Transport on Rough Landscapes: Morphology, Hierarchical Structure, and Horton Analysis of Riverlike Networks of Vortices*, Phys. Rev. Lett. **82**, 3641 (1999).

[27] Y. Cao, Z. Jiao, H. Ying, *Numerical Study on the Dynamics of a Driven Disordered Vortex Lattice*, Phys. Rev. B **62**, 4163 (2000).

[28] W. K. Kwok, G. W. Craptree, J. A. Fendrich, L. M. Paulius, *Dynamic Instabilities in the Vortex Lattice of $YBa_2Cu_3O_{7-\delta}$*, Physica C **293**, 111 (1997).

[29] W. Henderson, E. Y. Andrei, M. J. Higgins, S. Bhattacharya, *Metastability and Glassy Behavior of a Driven Flux-Line Lattice*, Phys. Rev. Lett. **77**, 2077 (1996).

[30] W. Henderson, E. Y. Andrei, M. J. Higgins, *Plastic Motion of a Vortex Lattice Driven by Alternating Current*, Phys. Rev. Lett. **81**, 2352 (1998).

[31] C. J. Olson, C. Reichhardt, R. T. Scaletter, G. T. Zimányi, Niels Gronbech-Jensen, *Metastability and Transient Effects in Vortex Matter Near a Decoupling Transition*, Phys. Rev. B **67**, 184523 (2003).

[32] A. Kiliç, K. Kiliç, O. Çetin, *Vortex Instability and Time Effects in I–V Curves of Superconducting $Y_1Ba_2Cu_3O_{7-\delta}$*, J. Appl. Phys. **93**, 448 (2003); Virtual J. Appl. Supercon. Vol **4**, issue 1 (2003).

[33] A. C. Marley, M. J. Higgins, S. Bhattacharya, *Flux Flow Noise and Dynamical Transitions in a Flux Line Lattice*, Phys. Rev. Lett. **74**, 3029 (1995).

[34] G. D'Anna, P. L. Gammel, H. Safar, G. B. Alers, D. J. Bishop, *Vortex-Motion-Induced Voltage Noise in $YBa_2Cu_3O_{7-\delta}$ Single Crystals*, Phys. Rev. Lett. **75**, 3521 (1995).

[35] A. Kilic, K. Kilic, O. Cetin, *Vortex Instability and Hysteresis Effects in I–V Curves of Superconducting $Y_1Ba_2Cu_3O_{7-\delta}$*, Physica C **384**, 321 (2003); H. Yetiş, A. Kiliç, K. Kiliç, A. Altinkok, and M. Olutaş, *Observation of Unusual Irreversible/Reversible Effects in a Macroscopic Cylindrical Hole Drilled in Superconducting Bi–Sr–Ca–Cu–O*, Physica C **468**, 1435 (2008).

[36] P. Chowdhury, S. K. Gupta, C. L. Prajapat, G. Yashwant, M. R. Singh, G. Ravikumar, J. V. Yakhmi, V. C. Sahni, *Dynamics of Transition from Metastable Disordered State to Ordered State of Vortex Structure in 2H-$NbSe_2$ Single Crystals*, Physica C **436**, 1 (2006).

[37] D. Goldschmidt, *Critical Currents and Current-Voltage Characteristics in Superconducting Ceramic* $YBa_2Cu_3O_{7-\delta}$, Phys. Rev. B **39**, 9139 (1989).

[38] A. V. Samoilov, M. Konczykowski, C. N. Yeh, S. Berry, C. C. Tauei, *Electric-Field-Induced Electronic Instability in Amorphous* Mo_3Si *Superconducting Films*, Phys. Rev. Lett. **75**, 4118 (1995).

[39] B. A. Glowacki, H. Noji, A. Oota, *The Effect of the Time Dependent Angular Distribution of the Intergrain Magnetic Field on the Transport Critical Current in* $Ag\text{-}(Bi,Pb)_2Sr_2Ca_2Cu_3O_x$ *Tapes*, J. Appl. Phys. **80**, 2311 (1996).

[40] Y. Liu, H. Luo, X. Leng, Z. H. Wang, L. Qui, S. Y. Ding, *History Effect in Inhomogeneous Superconductors*, Phys. Rev. B **66**, 144510 (2002).

[41] S. Bhattacharya, M. J. Higgins, *Flux-Flow Fingerprint of Disorder: Melting versus Tearing of a Flux-Line Lattice*, Phys. Rev. B. **52**, 64 (1995).

[42] Z. L. Xiao, E. Y. Andrei, P. Shuk, M. Greenblatt, *Equilibration and Dynamic Phase Transitions of a Driven Vortex Lattice*, Phys. Rev. Lett. **85**, 3265 (2000).

[43] Z. L. Xiao, O. Dogru, E. Y. Andrei, P. Shuk, M. Greenblatt, *Observation of the Vortex Lattice Spinodal in* $NbSe_2$, Phys. Rev. Lett. **92**, 227004 (2004).

[44] K. Kilic, A. Kilic, A. Altinkok, H. Yetis, O. Cetin, *Current-Induced Voltage Oscillations in Superconducting* $Y_1Ba_2Cu_3O_{7-\delta}$, Eur. Phys. J. B **48**, 189 (2005).

[45] C. Reichhardt, G. T. Zimányi, *Melting of Moving Vortex Lattices in Systems with Periodic Pinning*, Phys. Rev. B **61**, 14354 (2000).

[46] M. Benkraouda, I. M. Obaidat, U. Al Khajawa, *Temperature and Pinning Strength Dependence of the Critical Current of a Superconductor with a Square Periodic Array of Pinning Sites*, Physica C **433**, 205 (2006).

[47] A. C. Shi, A. John Berlinsky, *Pinning and I – V Characteristics of a Two-Dimensional Defective Flux-Line Lattice*, Phys. Rev. Lett. **67**, 1926 (1991).

[48] Y. Cao, Z. Jiao, *Pinning and Thermal Fluctuation Effects on the Two-Dimensional Vortex Lattice: A Numerical Study*, Physica C **321**, 177 (1999).

[49] C. J. Olson and C. Reichhardt, *Transverse Depinning in Strongly Driven Vortex Lattices with Disorder*, Phys. Rev. B **61**, R3811 (2000).

[50] C. J. Olson, C. Reichhardt, B. Jank, F. Nori, *Collective Interaction-Driven Ratchet for Transporting Flux Quanta*, Phys. Rev. Lett. **87**, 177002 (2001).

[51] K. Moon, R. T. Scalettar, G. T. Zimányi, *Dynamical Phases of Driven Vortex Systems*, Phys. Rev. Lett. **77**, 2778 (1996).

[52] H. Fangohr, Simon J. Cox, Peter A. J. De Groot, *Vortex Dynamics in Two-Dimensional Systems at High Driving Forces*, Phys. Rev. B **64**, 064505 (2001).

[53] T. Matsuda, K. Harada, H. Kasai, O. Kamimura, A. Tonomura, *Observation of Dynamic Interaction of Vortices with Pinning Centers by Lorentz Microscopy*, Science **271**, 393 (1996).

[54] K. Harada, O. Kamimura, H. Kasai, T. Matsuda, A. Tonomura, *Direct Observation of Vortex Dynamics in Superconducting Films with Regular Arrays of Defects*, Science **274**, 1167 (1996).

[55] V. Metlushko, U. Welp, G. W. Crabtree, R. Osgood, S. D. Bader, L. E. DeLong, Zhao Zhang, S. R. J. Brueck, B. Ilic, K. Chung, P. J.Hesketh, *Interstitial Flux Phases in a Superconducting Niobium Film with a Square Lattice of Artificial Pinning Centers*, Phys. Rev B **60**, R12585 (1999).

[56] A. Bezryadin, Yu. N. Ovchinnikov, B. Pannetier, *Nucleation of Vortices Inside Open and Blind Microholes*, Phys. Rev. B **53**, 8553 (1996).

[57] A. I. Buzdin, *Multiple-Quanta Vortices at Columnar Defects*, Phys. Rev. B **47**, 11416 (1993).

[58] G. M. Braverman, S. A. Gresedeskul, Y. Avishai, *Multiquantum Vortices in Conventional Superconductors with Columnar Defects Near the Upper Critical Field*, Phys. Rev. B **57**, 13899 (1998).

[59] M. M. Doria, G. F. Zebende, *Multiple Trapping of Vortex Lines by a Regular Array of Pinning Centers*, Phys. Rev B **66**, 064519 (2002).

[60] A. Tonomura et al., *Lorentz Microscopy Observation of Vortices Inside Bi-2212 Thin Films with Columnar Defects*, Physica C **369**, 68 (2002).

[61] A. Kilic, K. Kilic, H. Yetis, M. Olutas, A. Altinkok, H. Sozeri, O. Cetin, *Flux Trapping in a Macroscopic Cylinderical Hole Drilled in Bi-Sr-Ca-Cu-O*, Eur. Phys. J. B **50**, 565 (2006); H. Yetiş, A. Altinkok, M. Olutaş, A. Kiliç, and K. Kiliç, *Flux Dynamics and Magnetovoltage Measurements in a Macroscopic Cylindrical Hole Drilled in BSCCO*, Physica C **463**, 445 (2007).

[62] A. V. Silhanek, S. Raedts, M. J. Van Bael, and V. V. Moshchalkov, *Experimental Determination of the Number of Flux Lines Trapped by Microholes in Superconducting Samples*, Phys. Rev. B **70**, 054515 (2004).

[63] S. Senoussi, *Review of the Critical Current Densities and Magnetic Irreversibilities in High T_c Superconductors*, J. Phys. (Paris) III, **2**, 1041 (1992).

[64] S. Senoussi, A. Kilic, P. Manuel, R. Gagnon, L. Taillefer, and H. Traxler, *Anomalous Flux Pinning and Flux Creep Near the Critical State*, Physica C **264**, 172 (1996).

[65] R. Prozorov, A. Poddar, E. Sheriff, A. Shaulov, and Y. Yeshurun, *Irreversible Magnetization in Thin YBCO Films Rotated in External Magnetic Field*, Phsyica C **264**, 27 (1996).

[66] E. Sheriff, R. Prozorov, Y. Yeshurun, A. Shaulov, G. Koren, and C. Chabaud-Villard, *Magnetization and Flux Creep in Thin $YBa_2Cu_3O_{7-\delta}$ Films of Various Thickness*, J. Appl. Phys. **82**, 4417 (1997).

[67] A. Kiliç, K. Kiliç, S. Senoussi, *Grain Size Dependence of the Current–Voltage Characteristics and Critical Current Density in the Self-Field Approximation*, J. Appl. Phys. **84**, 3254 (1998).

[68] X. Y. Cai, A. Gurevich, I-Fei Tsu, D. L. Kaiser, S. E. Babcock, and D. C. Larbalastier, *Large Enhancement of Critical-Current Density due to Vortex Matching at the Periodic Facet Structure in $YBa_2Cu_3O_{7-\delta}$ Bicrystals*, Phys. Rev. B **57**, 10951 (1998).

[69] L. Ji, M. S. Rzchowski, N. Anand, and M. Tinkham, *Magnetic-Field-Dependent Surface Resistance and Two-Level Critical-State Model for Granular Superconductors*, Phys. Rev. B. **47**, 470 (1993).

[70] P. Mune, F. C. Foncesa, R. Muccillo, and R. F. Jardim, *Magnetic Hysteresis of the Magnetoresistance and the Critical Current Density in Polycrystalline $YBa_2Cu_3O_{7-\delta}$–Ag Superconductors*, Physica C **390**, 363 (2003).

[71] A. Kiliç, K. Kiliç, H. Yetiş and O. Çetin, *Low-Field Magnetovoltage Measurements in Superconducting $Y_1Ba_2Cu_3O_{7-\delta}$*, New J. Phys. **7**, 212 (2005).

[72] B. A. Albiss, *Thick Films of Superconducting YBCO as Magnetic Sensors*, Supercond. Sci. Technol. **18**, 1222 (2005).

[73] C. Kittel, *Introduction to Solid State Physics*, John Wiley and Sons, 7th Edition, (1996).

[74] J. Bardeen, L.N. Cooper and J.R. Schrieffer, *Theory of Superconductivity*, Phys. Rev. **108**, 1175 (1957).

[75] J. D. Jackson, *Classical Electrodynamics*, New York, Wiley, (1962).

[76] V. L. Ginzburg and L. D. Landau, *On the Theory of Superconductviy*, Zh. Eksperim. Teor. Fiz. **20**, 1064 (1950).

[77] L. D. Landau, E. M. Lifshitz: *Statistical Physics*, 3rd edn, part 1 (Nauka, Moskow 1976).

[78] V. V. Schmidt, *Physics of Superconductors, Introduction to Fundamentals and Applications*, Springer-Verlag Berlin, (1997).

[79] A. A. Abrikosov, *On the Magnetic Properties of Superconductors of the Second Group*, Sov. Phys. JETP, **5**, 1174 (1957).

[80] A. A. Abrikosov, *Fundamentals of the Theory of Metals* (North-Holland, Amsterdam, 1988).

[81] M. Thinkham, *Introduction to Superconductivity*, 2nd Edition, Mc Graw-Hill Inc, P. 319 (1996).

[82] A. Kilic, *Analysis of the Current-Voltage Characteristics and Transport Critical Current Density of Superconducting $YBa_2Cu_3O_{7-\delta}$ in the Self-Field Approximation*, Supercond. Sci. Technol. **8**, 497 (1995).

[83] P. W. Anderson, *Theory of Flux Creep in Hard Superconductors*, Phys. Rev. Lett **9**, 309 (1962); P.W. Anderson and Y.B. Kim, *Hard Superconductivity: Theory of the Motion of Abrikosov Flux Lines*, Rev. Mod. Phys. **36**, 39 (1964).

[84] Yu. S. Karimov, A. D. Kikin, *New Relaxation Phenomena in High-T_c Ceramic Superconductors*, Physica C **169**, 50 (1990).

[85] K. A. Müller, M. Takashiga, J. G. Bednorz, *Flux Trapping and Superconductive Glass State in La_2CuO_{4-y}:Ba*, Phys. Rev. Lett. **58**, 1143 (1987).

[86] I. Morgernstern, K. A. Müller, J. G. Bednorz, *Numerical Simulations of a High-T_c-Superconductive Glass Model*, Z. Phys. B **69**, 33 (1987).

[87] C. Rossel, Y. Maeno, I. Morgenstern, *Memory Effects in a Superconducting Y-Ba-Cu-O Single Crystal: A Similarity to Spin-Glasses*, Phys. Rev. Lett. **62**, 681 (1989).

[88] A. P. Malozemoff, L. Krusin-Elbaum, D. C. Cronomeyer, Y. Yeshurun, F. Holtzberg, *Intensities of Zero-Phonon $T_v(0)$ and $V_v(0)$ Single Transitions and $S_v(0)+R_{v'}(0)$ and $S_v(0)+T_{v'}(0)$ Double Transitions in Solid HD*, Phys. Rev. B **38**, 6440 (1988).

[89] R. V. Chamberlin, M. Hardiman, L. A. Turkevich, R. Orbach, *H-T Phase Diagram for Spin-Glasses: An Experimental Study of Ag:Mn*, Phys. Rev. B **25**, 6720 (1982).

[90] G. Deutscher, K. A. Müller, *Origin of Superconductive Glassy State and Extrinsic Critical Currents in High-T_c Oxides*, Phys. Rev. Lett. **59**, 1745 (1987).

[91] G. Deutscher, *Superconducting Glass and Related Properties*, Physica C **153 - 155**, 15 (1988).

[92] J. R. Clem, *Granular and Superconducting-Glass Properties of the High-Temperature Superconductors*, Physica C **153 - 155**, 50 (1988).

[93] I. Morgenstern, K. A. Müller, J. G. Bednorz, *Glass Behavior of High-T_c Superconductors*, Physica C **153 - 155**, 59 (1988).

[94] J. Wang, K. N. R Taylor, D. N. Matthews, H. K. Liu, G. J. Russel, S. X. Dou, *Magnetoresistance Relaxation and Flux Creep in High-T_c Superconductors*, Physica C **180**, 307 (1991).

[95] M. Tinkhams and C. J. Lobb, *Physical Properties of the New Superconductors*, Solid State Phys. **42**, 91 (1989).

[96] A. Kiliç, K. Kiliç, S. Senoussi and K. Demir, *Influence of an External Magnetic Field on the Current–Voltage Characteristics and Transport Critical Current Density*, Physica C **294**, 203 (1998).

[97] A. M. Campbell, J. Evetts, *Flux Vortices and Transport Currents in Type II Superconductors*, Adv. Phys. **21**, 199 (1972).

[98] D. Dew-Hughes, *Model for Flux Creep in High T_c Superconductors*, Cryogenics **28**, 674 (1988).

[99] L. P. Ma, H. C. Li, R. L. Wang, L. Li, *The Nature of the Relaxation of Resistivity in High-T_c Superconductors,* Physica C **279**, 79 (1997).

[100] E. Zeldov, N. M. Amer, G. Koren, A. Gupta, M. W. WcEIfresh, R. J. Gambino, *Flux Creep Characteristics in High-Temperature Superconductors*, Appl. Phys. Lett. **56**, 680 (1990).

[101] I. Hamadneh, A. Agil, A. K. Yahya, S. A. Halim, *Superconducting Properties of Bulk $Bi_{1.6}Pb_{0.4}Sr_2Ca_{2-x}Cd_xCu_3O_{10}$ System Prepared via Conventional Solid State and Coprecipitation Methods*, Physica C **463**, 207 (2007).

[102] Donglu Shi, H. E. Kourous, Ming Xu, and D. H. Kim, *Thermally Activated Dissipation in a Long-Term-Annealed Single Crystal of $Bi_2Sr_2CaCu_2O_x$*, Phys. Rev. B **43**, 514 (1991).

[103] K. Kiliç, A. Kiliç, A. Altinkok, H. Yetiş, O. Çetin, and Y. Dürüst, *Time Evolution of Quenched State and Correlation to Glassy Effects*, Physica C **420,** 1 (2005).

[104] H. Dersch and G. Blatter, *New Critical-State Model for Critical Currents in Ceramic High-T_c Superconductors*, Phys. Rev. B **38**, 11391 (1988).

[105] D. Dimos, P. Chaudhari and J. Mannhart, *Superconducting Transport Properties of Grain Boundaries in $YBa_2Cu_3O_7$ Bicrystals*, Phys. Rev. B. **41**, 4038 (1990).

[106] T. R. Askew, R. B. Flippen, K. J. Leary, and M. N. Kunchur, *Local Magnetic Field Distribution in Polycrystalline $YBa_2Cu_3O_7$ and Its Influence on Bulk Critical Currents*, J. Mater. Res. **6**, 1135 (1991).

[107] H. Hilgenkamp and J. Mannhart, *Grain Boundaries in High-T_c Superconductors*, Rev. Mod. Phys. **74**, 485 (2002).

[108] K. Kiliç, A. Kiliç, H. Yetiş and O. Çetin, *Transport Relaxation Phenomena in Superconducting $Y_1Ba_2Cu_3O_{7-\delta}$*, J. Appl. Phys. **95**, 1924 (2004).

[109] H. Nordborg, V. M. Vinokur, *Interaction between a Vortex and a Columnar Defect in the London Approximation*, Phys. Rev. B **62**, 12408 (2000).

[110] M. M. Doria, S. C. B. de Andrade, E. Sardella, *Maximum Number of Flux Lines Inside Columnar Defects*, Physica C **341**, 1199 (2000).

[111] J. E. Evetts and B. A. Glowacki, *Relation of Critical Current Irreversibility to Trapped Flux and Microstructure in Polycrystalline $YBa_2Cu_3O_7$*, Cryogenics **28**, 641 (1988).

[112] K. Kwasnitza and Ch Widmer, *Hysteretic Effects in the Flux-Flow State of Granular High-T_c Superconductors*, Physica C **171**, 211 (1990).

[113] T. S. Orlova, A. N. Kudymov, B. I. Smirnov, D.J. Miller, M. T. Lanagan, and K. C. Goretta, *Hysteretic Effects in the Flux-Flow State of Granular High-T_c Superconductors*, Physica C **235**, 194 (1995).

[114] J. A. Fendrich, U. Welp, W. K. Kwok, A. E. Koshelev, G. W. Craptree, and B. W. Veal, *Static and Dynamic Vortex Phases in $YBa_2Cu_3O_{7-\delta}$*, Phys. Rev. Lett. **77**, 2073 (1996).

[115] B. I. Smirnov, T. S. Orlova, A. N. Kudymov, M. T. Lanagan, M. P. Chudzik, N. Chen and K. C. Goretta, *Electric Field Effect in $(BiPb)_2Sr_2Ca_2Cu_3O_x$ Superconductor Bars*, Physica C **273**, 255 (1997).

[116] B. Sas, F. Portier, K. Vad, B. Keszei, L. F. Kiss, N. Hegman, I. Puha, S. Meszaros, and F. I. B. Williams, *Metastability Line in the Phase Diagram of Vortices in $Bi_2Sr_2CaCu_2O_8$*, Phys. Rev. B **61**, 9118 (2000).

[117] R. Wördenweber, P. H. Kes, and C. C. Tsuei, *Peak and History Effects in Two-Dimensional Collective Flux Pinning*, Phys. Rev. B **33**, 3172 (1985).

[118] P. F. Herrmann, L. Schellenberg, J. Zuccone, B. Seeber, O. Fischer, R. Grill, and J. A. A. J. Perenboom, *Investigation of Voltage Steps of U(I) Curves in $PbMo_6S_8$ Wires*, Physica C **202**, 61 (1992).

[119] M. C. Hellerqvist, D. Ephron, W. R. White, M. R. Beasley and A. Kapitulnik, *Vortex Dynamics in Two-Dimensional Amorphous $Mo_{77}Ge_{23}$ Films*, Phys. Rev. Lett. **76**, 4022 (1996).

[120] R. Exartiera and L. F. Cugliandolo, *Slow Relaxations and History Dependence of the Transport Properties of Layered Superconductors*, Phys. Rev. B **66**, 012517 (2002).

[121] A. V. Gurevich, R. G. Mints, *Self-Heating in Normal Metals and Superconductors*, Rev. Mod. Phys. **59**, 941 (1987).

[122] M. Marchevsky, M. J. Higgins and S. Bhattacharya, *Driven Dynamics of the Vortex-Phase Mixture near the Peak Effect: The "Vortex Capacitor"*, Phys. Rev. Lett. **88**, 087002 (2002).

[123] N. R. Dilley, J. Hermann, S. H. Han, and M. B. Maple, *Dynamic Transition Near the Peak Effect in $CeRu_2$*, Phys. Rev. B **56**, 2379 (1997).

[124] K. Runge and B. Pannetier, *First Decoration of Superconducting Networks*, Europhys. Lett. **24**, 737 (1993).

[125] J. Van de Vondel, C. C. de Souza Silva, B. Y. Zhu, M. Morelle, and V. V. Moshchalkov, *Vortex-Rectification Effects in Films with Periodic Asymmetric Pinning*, Phys. Rev. Lett. **94**, 057003 (2005).

[126] Y. Paltiel, D. T. Fuchs, E. Zeldov, Y. N. Myasoedov, H. Shtrikman, M. L. Rapparort, E. Y. Andrei, *Surface Barrier Dominated Transport in $NbSe_2$*, Phys. Rev. B **58**, R14763 (1998).

[127] Z. L. Xiao, E. Y. Andrei, Y. Paltiel, E. Zeldov, P. Shuk, and M. Greenblatt, *Edge and Bulk Transport in the Mixed State of a Type-II Superconductor*, Phys. Rev. B **65**, 094511 (2002).

[128] X. Leng, S. Y. Ding, Y. Liu, Z. H. Wang, H. K. Liu, and S. X. Dou, *Dip Effect in AC Susceptibility due to Surface Barrier with Flux Creep*, Phys. Rev. B **68**, 214511 (2003).

[129] D. Lopez, R. Decca and F. De la Cruz, *Topological Pinning and Flux Flow in Ceramic Superconductors*, Solid State Commun. **79**, 959 (1991).

[130] R. Wördenweber, P. Dymashevski, V. R. Misko, *Guidance of Vortices and the Vortex Ratchet Effect in High-T_c Superconducting Thin Films Obtained by Arrangement of Antidots*, Phys. Rev. B **69**, 184504 (2004).

[131] J. Dumas, C. Schlenker, J. Markus, and R. Buder, *Nonlinear Conductivity and Noise in the Quasi One-Dimensional Blue Bronze $K_{0.30}MoO_3$*, Phys. Rev. Lett. **50**, 757 (1983).

[132] R. P. Hall and A. Zettl, *Role of Current Oscillations in AC-DC Interference Effects in $NbSe_3$*, Phys. Rev. B **30**, 2279 (1984).

[133] H. F. Hundley and A. Zettl, *Shapiro-Step Spectrum and Phase-Velocity Coherence in $NbSe_3$ in a Uniform Temperature Gradient*, Phys. Rev. B **33**, 2883 (1986).

[134] R. M. Fleming and L. F. Schneemeyer, *Observation of a Pulse-Duration Memory Effect in $K_{0.30}MoO_3$*, Phys. Rev. B **33**, 2930 (1986).

[135] S. N. Coppersmith and P. B. Littlewood, *Pulse-Duration Memory Effect and Deformable Charge-Density Waves*, Phys. Rev. B **36**, 311 (1987).

[136] S. N. Coppersmith, *Phase Slips and the Instability of the Fukuyama-Lee-Rice Model of Charge-Density Waves*, Phys. Rev. Lett. **65**, 1044 (1990).

[137] S. N. Coppersmith and A. J. Millis, *Diverging Strains in the Phase-Deformation Model of Sliding Charge-Density Waves*, Phys. Rev. B **44**, 7799 (1991).

[138] K. L. Ringland, A. C. Finnefrock, Y. Li, J. D. Brock, S. G. Lemay, and R. E. Thorne, *Scaling in Charge-Density-Wave Relaxation: Time-Resolved X-Ray Scattering Measurements*, Phys. Rev. Lett. **82**, 1923 (1999).

[139] M. Karttunen, M. Haataja, K. R. Elder, and M. Grant, *Defects, Order, and Hysteresis in Driven Charge-Density Waves*, Phys. Rev. Lett **83**, 3518 (1999).

[140] I. Garcia-Fornaris, E. Govea-Alcaide, P. Mune, and R. F. Jardim, *Magnetoresistance, Transport Noise and Granular Structure in Polycrystalline Superconductors*, Phys. Stat. Sol. (a) **204**, 805 (2007).

[141] I. S. Beloborodov, K. B. Efetov, and A. I. Larkin, *Magnetoresistance of Granular Superconducting Metals in a Strong Magnetic Field*, Phys. Rev. B **61**, 9145 (2000).

[142] A. Gerber, A. Milner, G. Deustscher, M. Karpovsky, and A. Gladkikh, *Insulator-Superconductor Transition in 3D Granular Al-Ge Films*, Phys. Rev. Lett. **78**, 4277 (1997).

[143] A. Palau, T. Puig, X. Obradors, E. Pardo, C. Navau, A. Sanchez, A. Usoskin, H. C. Freyhardt, L. Fernandez, B. Holzapfel, and R. Feenstra, *Simultaneous Inductive Determination of Grain and Intergrain Critical Current Densities of $YBa_2Cu_3O_{7-x}$ Coated Conductors*, Appl. Phys. Lett. **84**, 230 (2004).

[144] K. Y. Chen and Y. J. Qian, *Critical Current and Magnetoresistance Hysteresis in Polycrystalline* $YBa_2Cu_3O_{7-x}$, Physica C **159**, 131 (1989).

[145] Y. J. Qian, Z. M. Zhang, K. Y. Chen, B. Zhou, J. W. Qui, B. C. Miao, and Y. M. Cai, *Transport Hysteresis of the Oxide Superconductor* $Y_1Ba_2Cu_3O_{7-x}$ *in Applied Fields*, Phys. Rev. B **39**, 4701 (1989).

[146] G. S. Mkrtchyan, V. V. Shmidt, *Interaction Between a Cavity and a Vortex in a Superconductor of the Second Kind*, Sov. Phys. JETP **34**, 195 (1972).

[147] A. V. Silhanek, S. Raedts, M. Lange, V. V. Moshchalkov, *Field-Dependent Vortex Pinning Strength in a Periodic Array of Antidots*, Phys. Rev. B **67**, 064502 (2003).

CURRICULUM VITAE

Hakan Yetiş

Address:

Abant İzzet Baysal University
Department of Physics,
Gölköy - Bolu, Turkey
Phone: +90 374 2541000
Fax: + 90 374 2534642
Email: yetis_h@ibu.edu.tr

Personal Details:

Gender: Male
Date of birth: 21nd of October, 1978
Place of birth: İstanbul, Turkey

Education:

1996-2001 Undergraduate Studies in Physics at the Abant İzzet Baysal University

2001-2003 MSc in Physics at the Abant İzzet Baysal University
Thesis: Transport and relaxation measurements in ceramic superconductor $Y_1Ba_2Cu_3O_{7-x}$.

2003-2009 PhD in Physics at the Abant İzzet Baysal University
Thesis: Irreversible transport phenomena in $Bi_{1.7}Pb_{0.3}Sr_2Ca_2Cu_3O_x$ superconductors.

Specialization: Superconductivity

Publications:

1. K. Kiliç, A. Kiliç, H. Yetiş, and O. Çetin "Low field transport relaxation measurements in superconducting $Y_1Ba_2Cu_3O_{7-\delta}$" Phys. Rev. B 68, 144513 (2003).

2. K. Kiliç, A. Kiliç, H. Yetiş, and O. Çetin, “Transport relaxation phenomena in superconducting $Y_1Ba_2Cu_3O_{7-\delta}$” J. Appl. Phys. 95, 1924 (2004).

3. K. Kiliç, A. Kiliç, A. Altinkok, H. Yetiş, O. Çetin, and Y. Durust “Time evolution of quenched state and correlations to glass effects” Physica C 420, 1 (2005).

4. K. Kiliç, A. Kiliç, A. Altinkok, H. Yetiş, and O. Çetin “Current-induced voltage oscillations in superconducting $Y_1Ba_2Cu_3O_{7-\delta}$” Eur. Phys. J. B 48, 189 (2005).

5. A. Kiliç, K. Kiliç, H. Yetiş, and O. Çetin "Low-field magnetovoltage measurements in superconducting $Y_1Ba_2Cu_3O_{7-d}$" New Journal of Physics 7, 212 (2005).

6. A. Kiliç, K. Kiliç, H. Yetiş, and O. Çetin "Current dependent reorganization in superconducting $Y_1Ba_2Cu_3O_{7-d}$ " Eur. Phys. J. B 46, 177 (2005).

7. A. Kiliç, K. Kiliç, H. Yetiş, M. Olutaş, A. Altinkok, H. Sözeri, and O. Çetin “Flux trapping in a macroscopic cylinderical hole drilled in Bi-Sr-Ca-Cu-O ” Eur. Phys. J. B 50, 565 (2006).

8. A. Altinkok, H. Yetiş, M. Olutaş, K. Kiliç, A. Kiliç, and O. Çetin "Coherent voltage oscillations in superconducting polycrystalline $Y_1Ba_2Cu_3O_{7-\delta}$" Journal of Phys. Conf. Ser. 43, 698 (2006).

9. M. Olutaş, H. Yetiş, A. Altinkok, H. Sözeri, K. Kiliç, A. Kiliç, and O. Çetin "Flux dynamics and time effects in a carved out superconducting polycrystalline Bi-Sr-Ca-Cu-O Sample" Journal of Phys. Conf. Ser. 43 631 (2006) .

10. H. Yetiş, A. Altinkok, M. Olutaş, K. Kiliç, A. Kiliç, and O. Çetin "Magnetovoltage measurements and field sweep rate dependence in superconducting polycrystalline YBCO" Journal of Phys. Conf. Ser. 43, 635 (2006) .

11. A. Altinkok, H. Yetiş, M. Olutaş, K. Kiliç, A. Kiliç “Time effects and glassy state behaviour in superconducting $YBa_2Cu_3O_{7-x}$“ Physica C 463, 371-373 (2007).

12. H. Yetiş, A. Altinkok, M. Olutaş, K. Kiliç, A. Kiliç “Flux dynamics and magnetovoltage measurements in a macroscopic cylindrical hole drilled in BSCCO” Physica C 463, 445-448 (2007).

13. A. Altinkok, H. Yetiş, K. Kiliç, A. Kiliç, M. Olutaş “ Slow voltage oscillations in Ag-doped superconducting YBCO” Physica C 468, 1419-1423 (2008).

14. H. Yetiş, A. Kiliç, K. Kiliç, A. Altinkok, M. Olutaş " Observation of unusual irreversible/reversible effects in a macroscopic cylindrical hole drilled in superconducting Bi–Sr–Ca–Cu–O" Physica C 468, 1435-1438 (2008).

15. M. Olutaş, H. Yetiş, A. Altinkok, A. Kiliç, K. Kiliç " Transport relaxation measurements and glassy state effects in superconducting MgB_2" Physica C 468, 1447-1450 (2008).

Presentations :

1. "Current-Induced Time Effects and Direct Observation of the Glassy State Relaxation in Superconducting $YBa_2Cu_3O_{7-x}$" European Conference on Applied Superconductivity (EUCAS' 03), Naples- Italy (2003).

2. "Dynamic Effects and Transport Relaxation Measurements in Superconducting $YBa_2Cu_3O_{7-x}$" European Conference on Applied Superconductivity (EUCAS' 03), Naples-Italy (2003).

3. "Quasi-Peak Effect Behavior and Direct Observation of the Transition from Josephson to Abrikosov Vortices" European Conference on Applied Superconductivity (EUCAS' 03), Naples-Italy (2003).

4. "$YBa_2Cu_3O_{7-x}$ Seramik Süperiletkeninde Zamana Bağlı Etkiler ve Taşıma Durulma Ölçümleri" Turkish Physical Society 22nd Meeting, Bodrum-Turkey (2004).

5. "YBCO Seramik Süperiletkeninde Camsı Durum Akı Dinamiği" Turkish Physical Society 22nd Meeting, Bodrum-Turkey (2004).

6. "Organization of Flux Lines and Transport Relaxation Measurements in Polycrystalline Superconducting $YBa_2Cu_3O_{7-d}$", İTÜ, 12th Statistical Physics Days, İstanbul-Turkey (2005).

7. "Magnetovoltage Measurements and Field Sweep Rate Dependence in Superconducting Polycrystalline YBCO" European Conference on Applied Superconductivity (EUCAS' 05), Vienna-Austria (2005).

8. "Coherent Voltage Oscillations in Superconducting Polycrystalline YBCO" European Conference on Applied Superconductivity (EUCAS' 05), Vienna-Austria (2005).

9. "Flux Dynamics and Time Effects In a Carved Out Superconducting Polycrystalline Bi-Sr-Ca-Cu-O Sample" European Conference on Applied Superconductivity (EUCAS' 05), Vienna-Austria (2005).

10. “Flux Dynamics and Magnetovoltage Measurements in Macroscopic Cylinderical Hole Drilled in BSCCO” 19th International Symposium on Superconductivity (ISS 2006) , Nagoya-Japan (2006).

11. "Time Effects and Glassy State Behaviour in Superconducting $YBa_2Cu_3O_{7-x}$" 19th International Symposium on Superconductivity (ISS 2006), Nagoya-Japan (2006).

12. “Slow Voltage Oscillations in Ag-Doped Superconducting Y-Ba-Cu-O” 20th International Symposium on Superconductivity (ISS 2007), Tsukuba-Japan (2007).

13. “Observation of Unusual Irreversible/Reversible Effects in a Macroscopic Cylinderical Hole Drilled in Superconducting Bi-Sr-Ca-Cu-O” 20th International Symposium on Superconductivity (ISS 2007), Tsukuba/Japan (2007).

14. “Transport Relaxation Measurements and Glassy State Effects in Superconducting MgB_2” 20th International Symposium on Superconductivity (ISS 2007), Tsukuba-Japan (2007).

15. “Slow Voltage Oscillations in Ag-doped Superconducting YBCO” Applied Superconductivity Conference (ASC08), Chicago-USA (2008).

16. “Observation of Unusual Irreversible/Reversible Effects in a Macroscopic Cylindrical Hole Drilled in Superconducting Bi–Sr–Ca–Cu–O” Applied Superconductivity Conference (ASC08), Chicago-USA (2008).

17. “Transport Relaxation Measurements and Glassy State Effects in Superconducting MgB_2” Applied Superconductivity Conference (ASC08), Chicago-USA (2008).

Projects:

1. $Y_1Ba_2Cu_3O_{7-x}$ Süperiletkeninde Orta ve Düşük Harcanımlı Vorteks Dinamiği, Tübitak, Grant No: TBAG-2037 (Researcher).

2. MgB_2 Süperiletkenin Elektriksel Özellikleri ve Yüksek Alan Akı Dinamiği, DPT, Grant No: 2004K120200 (Researcher).

3. Seramik Süperiletkenlerde Camsı Durum Akı Dinamiğinin İncelenmesi, AIBU Research Fund, Grant No: 2004.03.02.200 (Researcher).

Working Experience:

2001-2009 Working in Abant İzzet Baysal University, Physics Department as a research assistant.